January 2016

ALTERNATIVE ARCHITECTURE FOR SOLUTION PROCESSED THIN FILM SOLAR MATERIALS

Robert William Boyne
Purdue University

Graduate School Form
30 Updated 12/26/2015

PURDUE UNIVERSITY
GRADUATE SCHOOL
Thesis/Dissertation Acceptance

This is to certify that the thesis/dissertation prepared

By ROBERT WILLIAM BOYNE

Entitled

ALTERNATIVE ARCHITECTURE FOR SOLUTION PROCESSED THIN FILM SOLAR MATERIALS

For the degree of Master of Science in Chemical Engineering

Is approved by the final examining committee:

Rakesh Agrawal
Chair

Rajamani Gounder

Hilkka I Kenttamaa

Bryan W. Boudouris

To the best of my knowledge and as understood by the student in the Thesis/Dissertation Agreement, Publication Delay, and Certification Disclaimer (Graduate School Form 32), this thesis/dissertation adheres to the provisions of Purdue University's "Policy of Integrity in Research" and the use of copyright material.

Approved by Major Professor(s): Rakesh Agrawal

Approved by: John A. Morgan 7/27/2016

Head of the Departmental Graduate Program Date

ALTERNATIVE ARCHITECTURE FOR SOLUTION PROCESSED THIN FILM SOLAR MATERIALS

A Thesis

Submitted to the Faculty

of

Purdue University

by

Robert W. Boyne

In Partial Fulfillment of the

Requirements for the Degree

of

Master of Science in Chemical Engineering

August 2016

Purdue University

West Lafayette, Indiana

For my parents, Art and Christi Boyne, who always encouraged me, and to my grandfather, Robert Dayle Harris, whose dream was for all his grandchildren to get a good education.

ACKNOWLEDGEMENTS

I would like to acknowledge the collaboration of all of my lab-mates who have helped me both through training, suggestions and assistance with various measurements. I would particularly like to thank Dr. Caleb Miskin, Xianyi Hu and Scott McClary who provided SEM and EDX measurements for this thesis.

I would like to acknowledge my advisor, Prof. Rakesh Agrawal for his mentoring as a researcher and consultations on the work contained in this thesis.

I would also like to acknowledge our collaborators, at Purdue, particularly Prof. Hilkka Kentämaa, Priya Murria and Laurance Cain for their work in mass spectrometry examining amine thiol solutions, and Prof. Bryan Bourdouris for the use of UV-Vis spectroscopy, at NREL in Golden, Colorado, Maikel van Hest and Ethan Palay for collaboration and training in the fabrication of TiO_2 films, and Prof. Yanfa Yan at the University of Toledo for preparing perovskite cells to test our TiO_2 structures.

Finally, I would like to acknowledge the funding from the Department of Naval Research through the NEPTUNE project for the amine-thiol work, and graduate funding from the US D.O.E. through Graduate Assistance in Areas of National Need (GAANN) and the Solar Economy Integrative Graduate Education and Research Training (SEIGERT) program.

With thanks and appreciation, Robert W. Boyne.

TABLE OF CONTENTS

Page

LIST OF TABLES

LIST OF FIGURES

Figure Page

Figure Page

Figure Page

Figure Page

Figure Page

Figure Page

Figure Page

Figure Page

LIST OF ABBREVIATIONS

Ag: Silver

Ag_2S: Silver Sulfide

Ag_2Se: Siver Selenide

Au: Gold

AZO: Aluminum Zinc Oxide

BA: Butylamine

Cd: Cadmium

CdS: Cadmium Sulfide

$CdSO_4$: Cadmium Sulfate

CdTe: Cadmium Telluride

CIGS: Copper Indium Gallium Selenide

CIS: Copper Indium Diselenide

Cu: Copper

Cu_2S: Copper (I) Sulfide

Cu_2Se: Copper (I) Sulfide

Cu_3PS_4: Copper Tetrathiophosphate

$CuAcAc_2$: Copper (II) Acetylacetonate

CuCl: Copper (I) Chloride

$CuCl_2$: Copper (II) Chloride

CZTS: Copper Zinc Tin Selenide

CZTSSe: Copper Zinc Tin Sulfoselenide

DMSO: Dimethylsulfoxide

DSC: Dye-Sensitized Solar Cell

EDA: Ethylenediamine

EDT: Ethanedithiol

EQE: External Quantum Efficiency

FF: Fill Factor

FTO: Fluorine-Doped Tin Oxide Coated Glass

Ga: Gallium

$GaAcAc_3$: Gallium (III) Acetylacetonate

GeI_4: Germanium (IV) Iodide

GIXRD: Grazing Incident X-Ray Diffraction

HA: Hexylamine

In: Indium

In_2Se_3: Indium Selenide

$InAcAc_3$: Indium (III) Acetylacetonate

$InCl_3$: Indium (III) Acetylacetonate

InP: Indium Phosphide

IPA: Isopropanol

ITO: Tin-Doped Indium Oxide

IV: Current-Voltage

J_{SC}: Short Circuit Current Density

J-V: Current Density-Voltage

k: Boltzmann Constant

MgZnO: Magnesium Zinc Oxide

Mo: Molybdenum

NH_4OH: Ammonium Hydroxide

OLA: Oleylamine

OPV: Organic Photovoltaic

PT: Propanethiol

PTFE: Poly(Tetrfluoroethylene)

pXRD: Powder X-Ray Diffraction

S: Sulfur

Se: Selenium

Si: Silicon

Sn: Tin

$SnCl_2$: Tin (II) Chloride

SnO: Tin (II) Oxide

SnS: Tin(II) Sulfide

SnSe: Tin (II) Selenide

Spiro-OMeTAD: (2,2′,7,7′-tetrakis-(N,N-di-p-methoxyphenylamine)-9,9′-spirobifluorene)

T: Temperature

Te: Tellurium

TEA: Titanium Diethoxide bis(Acetylacetonate)

TFS-Li: Bis(Trifluoromethyl)Sulfonimide Lithium Salt]

Ti: Titanium

TIA: Titanium Diisopropoxide bis(Acetylacetonate)

$TiCl_4$: Titanium Tetrachloride

TiO_2: Titanium Dioxide

V_{OC}: Open Circuit Voltage

XPS: X-Ray Photoemission Spectroscopy

XRD: X-Ray Diffraction

Zn: Zinc

$ZnAcAc_2$: Zinc Acetylacetonate

$ZnCl_2$: Zinc Chloride

ZnO: Zinc Oxide

ZnS(O,OH): Zinc Hydroxysulfide

ABSTRACT

Boyne, Robert W. M.S., Purdue University, August 2016. Alternative Architecture for Solution Processed Thin Film Solar Materials. Major Professor: Rakesh Agrawal.

A variety of competing semiconductor materials are used to create p-n solar cells. Currently silicon solar cells dominate more than 90% of the solar market. The major competitors to silicon solar cells are inorganic thin-film solar cells, mainly cadmium telluride and copper indium gallium sulfide. These materials evolved from initial devices based off of cadmium sulfide. All of the non-silicon commercial cells still use cadmium sulfide in their production, which is of concern due to the toxicity of cadmium and limits their application, especially in Europe due to the E.U. Restriction of Hazardous Substances directive. If these devices are to remain market competitive, increased cost efficiency and the removal of cadmium are necessary.

First, the cadmium sulfide layers were optimized for nanoparticle CZTS devices, and an in situ measurement apparatus was developed to monitor the deposition thickness during processing. While photons absorbed into cadmium sulfide show low quantum efficiencies, increasing the thickness of the cadmium sulfide buffer layer from 50 to 70nm increased the open circuit voltage and reduced shunting, with only negligible loss in current density, yielding more efficient devices. This agrees with work done on

vacuum-based copper indium gallium cells in literature. Thinner films require a partial-electrolyte treatment to achieve comparable efficiencies.

Both mesoporous titanium dioxide films were developed as a potential alternative for CdS buffer layers. These layers are comparable to those used in perovskite and dye-sensitized solar cells. Titanium dioxide is a cadmium-free low toxicity alternative to cadmium sulfide as a n-type layer for photovoltaic devices. It has a different conduction band energy, making it a potential candidate for a variety of novel semiconductor materials that may not align with cadmium sulfide. Further, it is resistant to annealing in a selenium atmosphere, allowing solar absorbers to be deposited and annealed in an inverted structure, which, with a proper transparent conductor could create bifacial solar cells. CIGS and CIS devices were prepared on the mesoporous and planar structures, but showed short circuit currents limited to 120$\mu A/cm^2$. The major limitation of these devices is the poor metallurgical contact between the titanium dioxide and the absorber crystals.

Finally, a dissolution mechanism is proposed for the unique action of amine-thiol solvent mixtures. These solvents can be used to create semiconductor films from a variety of metal, chalcogenide and salt precursors. The mechanism relies on the Bronsted acid-base behavior of thiols and amines and the strong complexing potential of thiolates with soft metal ions such as copper, zinc and silver. Evidence suggests that the species in solution consist mainly of metal thiolates and alkylammonium salts. Understanding this mechanism may allow for better control of amine-thiol molecular precursor routes to device fabrication.

CHAPTER 1. INTRODUCTION

1.1 Introduction to Solar Cells

Since the initial discovery of the photovoltaic effect by Edmund Becquerel in 1839[1] and the subsequent development of platinum-selenium Schottky barrier solar cells by William Adams and Richard Day,[2] a wide variety of materials and architectures have been developed to effectively transform electromagnetic radiation into electricity. Silicon proved to be the first practical solar cell for energy production, as shown by Chapin, Fuller and Pearson who developed the first p-n solar cell with an efficiency of about 6% in 1954.[3] Since then, a wide variety of materials have been utilized to collect solar energy with varying effectiveness. Figure **1.1** illustrates the progress in many of the most prominent of these technologies.

All p-n solar cells rely on similar physics to operate. Semiconductors have electronic bands that are completely full at 0K, separated by a small gap by of a few electron volts from another band.[4] The full band is the valence band, where the next unfilled band is known as the conduction band. In a full band there are no available electronic states for electronics to move to and become conductive. At ambient temperatures on earth, a very small proportion of those electrons are at an excited energy according to the Fermi-Dirac distribution. Those electrons can move, and other electrons can move into the open energy levels, or holes, they leave behind. This causes the

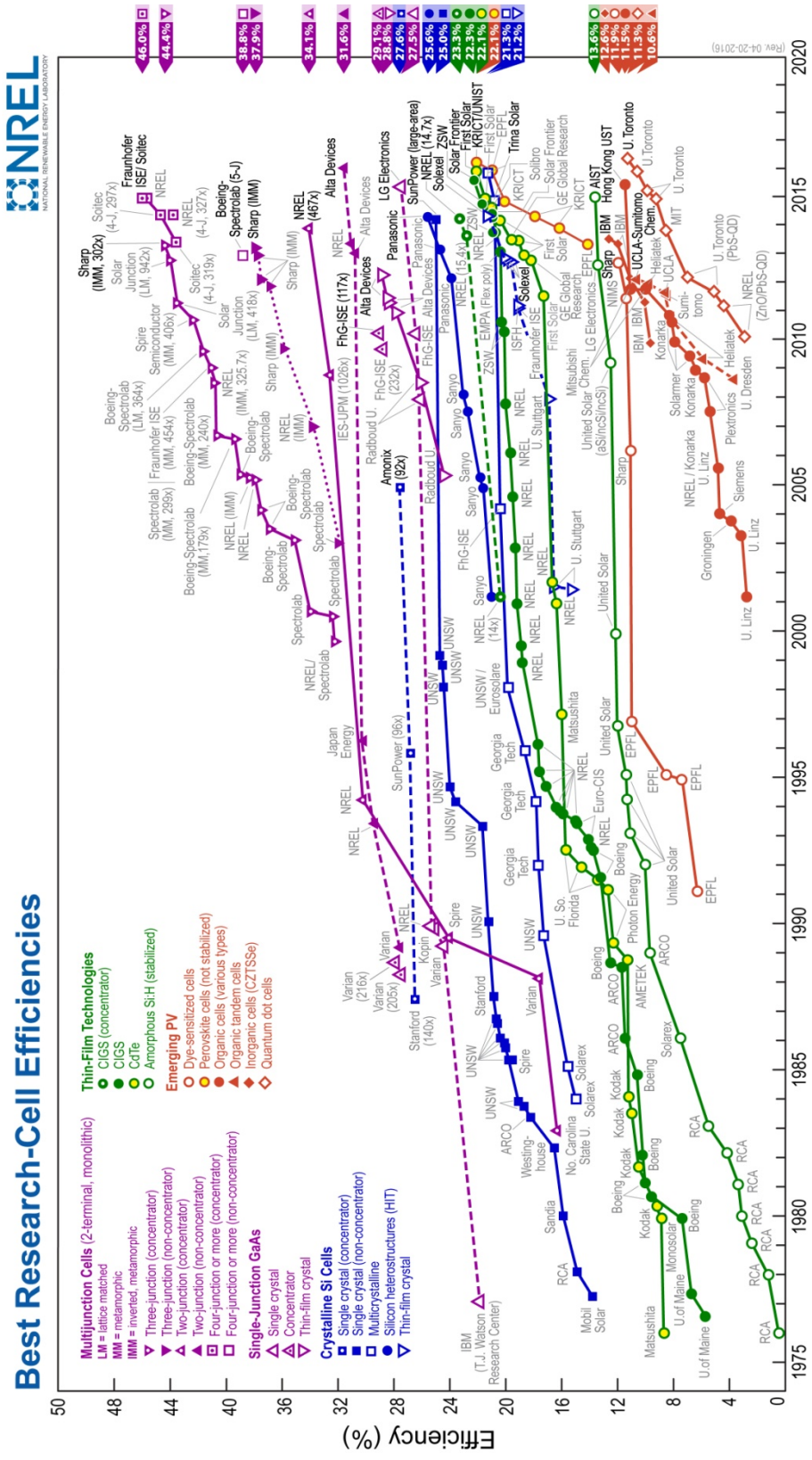

Figure 1.1: Best Solar Cell Efficiencies at Research Scale. This plot is courtesy of the National Renewable Energy Laboratory, Golden, CO.

material to have higher conductivity at higher temperatures, as opposed to metals whose conductivities decrease with higher temperature.[4] Trace impurities, known as dopants, or defects in the material create localized electronic defect states which can become more easily ionized depending on their location between bands. If they more easily accept, or trap, excited electrons, they leave an excess of holes, creating a p-type material. Instead, defects that more easily ionize to create excited electrons create an excess of electrons in the material, resulting in n-type conductivity. N and p-type conductivity refer to the charge of the majority charger carrier as shown by the sign of the Hall coefficient. These defect states shift the Fermi energy of the electrons in the material. Pure, defect-free materials have a Fermi energy close to the middle of the band structure and equal numbers of electrons and holes, and these materials are referred to as intrinsic. Figure 1.2 shows a simplified diagram of these band structures.

A diode is formed when a p-type and n-type semiconductor are brought into contact one with another. The excited electrons in the n-type material diffuse into the nearby electron deficient region of the p-type material according to Fick's law, leaving positively charged nuclei behind, and a negative charge in the p-type region creating an electric field, called a space-charge region. The current from the electric field quickly counteracts the diffusion flux and equilibrium is reached. When light excites an electron in this region, the electric field separates the electron and the hole from each other, creating a photocurrent, as shown in Figure 1.3 A wide variety of solar cells can be made by alternating the impurity doping levels within a material, the morphology of the material or by using different materials for either or both the n-type and p-type region.

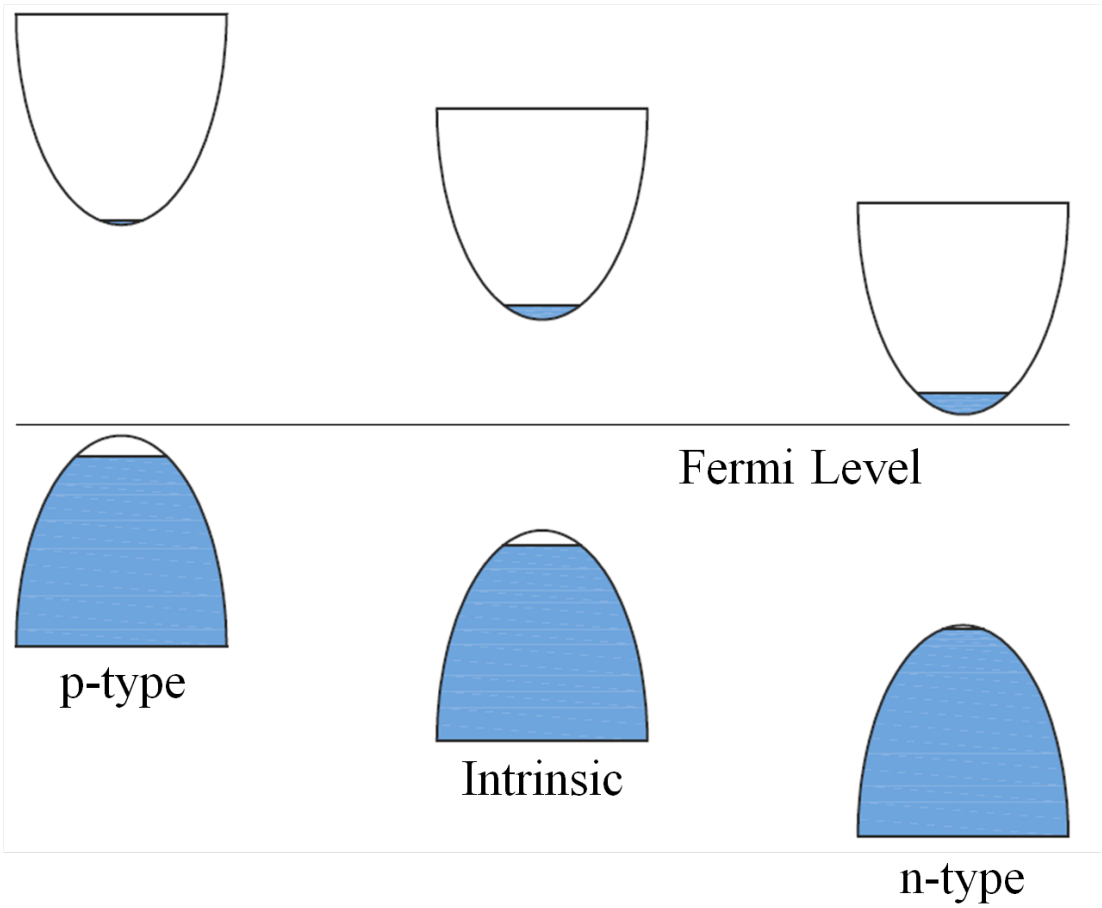

Figure 1.2: Simplified band structure of p-type, intrinsic and n-type semiconductors. Occupied electronic states are shown in blue, while unnocupied states are shown in white.

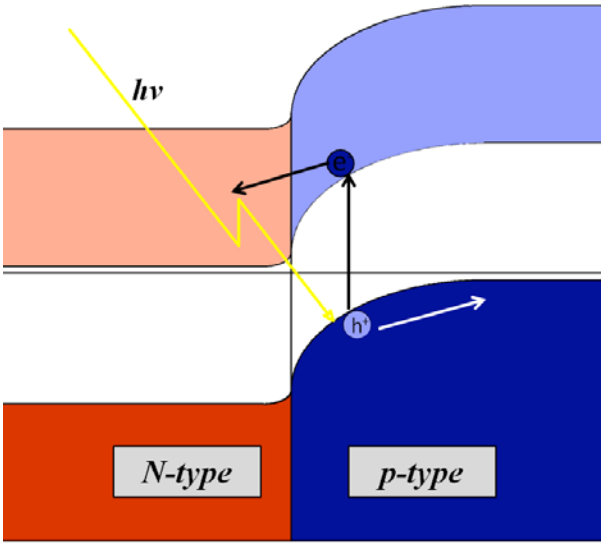

Figure 1.3: Diagram of a p-n solar cell.

The terrestrial photovoltaics market can be divided into three major divisions: polycrystalline silicon (poly Si), which held 55% of market share in 2013, single crystal silicon, (36% of market share) and thin film solar (the remaining 9%) as cadmium telluride (CdTe), copper indium gallium selenide (CIGSe) and amorphous silicon (a:Si).[5] Each technology has its advantages and disadvantages. Silicon solar cells tend to be more efficient overall, but thin films have shorter energy payback times and investments.[5] Also, silicon is the second most abundant element in Earth's crust after oxygen, while both CdTe and CIGSe require rare elements, especially indium and tellurium.[6] The use of these rare elements poses a problem for scaling up these technologies to terawatt scale.

Various alternative materials and methodologies have been and continue to be researched as alternatives to these materials, including copper zinc tin sulfoselenide (CZTSSe), ammonium lead halide perovskite, dye sensitized solar cells (DSC's), organic photovoltaics (OPV) and quantum dot solar cells.

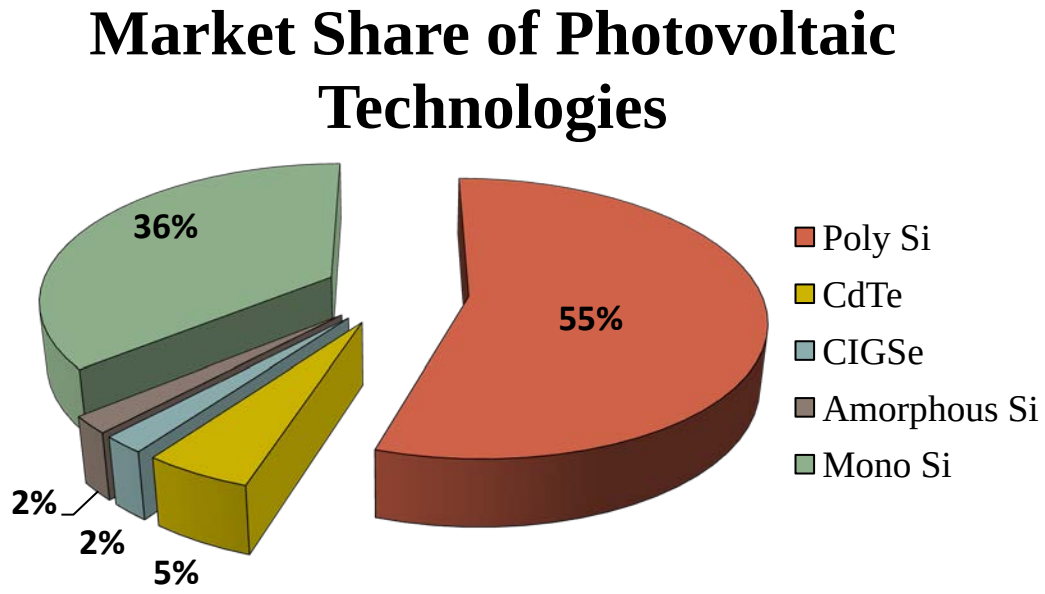

Figure 1.4: Market Share of Commercial Photovoltaic Technologies.[5]

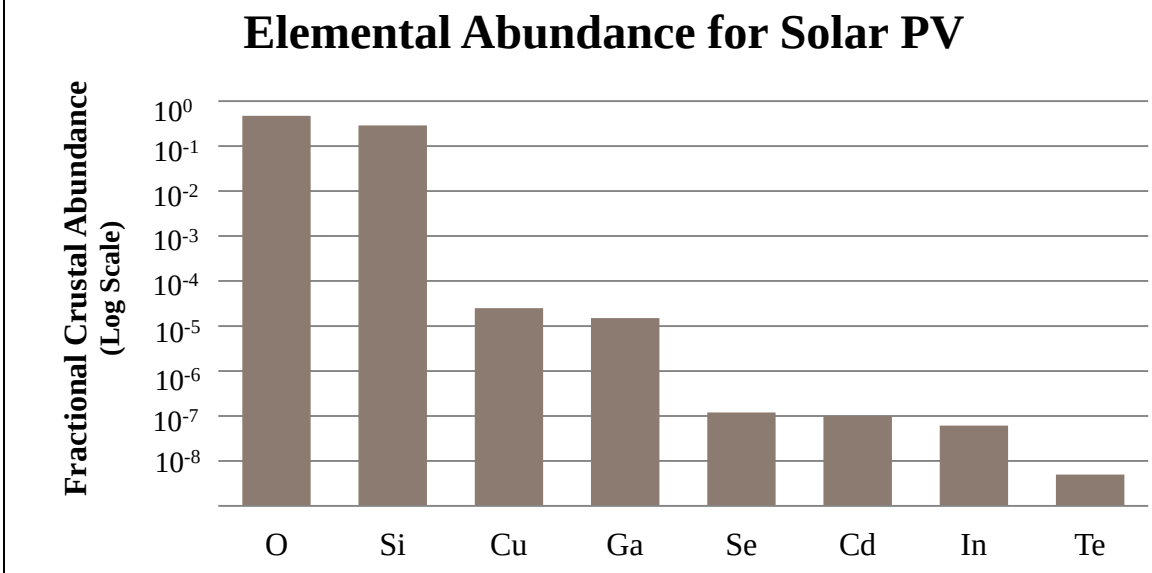

Figure 1.5: Abundance of major constitutive elements for various solar technologies in Earth's Crust.[6]

1.2 Thin Film Solar Cells

In 1954, alongside the advent of the first modern silicon-based solar cells, an n-type semiconductor, cadmium sulfide (CdS), was observed to have a photovoltaic effect by Reynolds et al.[7] Two years later, a 1% efficient cadmium sulfide cell was developed.[8,9] Shortly thereafter, it was recognized that a copper contact and/or a thin resulting layer of copper sulfide was necessary to achieve effective performance of these CdS solar cells.[10,11] Various methodologies were used to create these CdS layers, including sintering of CdS powder,[12] spray coating,[13] evaporation[14] and chemical bath deposition.[15,16] Related compounds, including cadmium selenide (CdSe) and cadmium telluride (CdTe) were also shown to have photoconductive and photovoltaic properties by Richard Bube.[17] Cadmium sulfide was then combined with CdTe[18] and other p-type materials, such as copper indium selenide[19] (CIS) and indium phosphide[20] (InP) to provide the basis for most inorganic thin film solar cells. Most modern inorganic thin-film solar cells are based off of this CdS technology. As stated before, this leaves many issues with the toxicity of cadmium, which has resulted in legal conflicts and bans on cadmium containing technologies, particularly within the EU.[21]

Researchers continue to look for alternatives to replace the rare and toxic materials found within various thin film solar cells. One of the more well studied alternative p-type absorbers is kesterite copper zinc tin sulfoselenide (CZTSSe)[22] which has been developed and now holds a record 12.6% efficiency.[23] By comparison, copper indium gallium selenide (CIGS) has a record efficiency of 22.3%[24] while CdTe holds a record efficiency of 22.1%.[25] More recent alternatives rely on replacing some of the elements commonly found in CIGS and CZTS with alternative metal cations, particularly

those that tend to monovalent oxidation states, or that have significantly different ionic radii to reduce the defects caused by intermixing of cations.[26] Examples based on CZTS include replacing the tin in with germanium[27] or indium,[28] replacing the zinc with barium,[29] or replacing the copper with silver.[30] Silver can also be used to substitute for copper in CIGS based systems,[31] and some work has been done in replacing the indium-gallium CIGS alloy with a copper indium-aluminum selenide.[32] All of these crystal structures are variations on the diamond-like zincblende structure, and theoretical work has been done to suggest other possible alternative materials within this structure group.[33] Other systems of interest with a similar structure are the Cu_3-V-VI_4 group of semiconductors such as copper tetrathiophosphate (Cu_3PS_4),[34] as well as analogues with sulfur replaced by other chalcogens, Se and Te,[35] or phosphorous replaced with other pnictides, As[36] or Sb.[37] The chalcopyrite structure of CIGS and the kesterite and stannite structures of CZTS are shown in Figure 1.6.

Alternative buffer layers for CdS have also been researched. Zinc oxysulfide

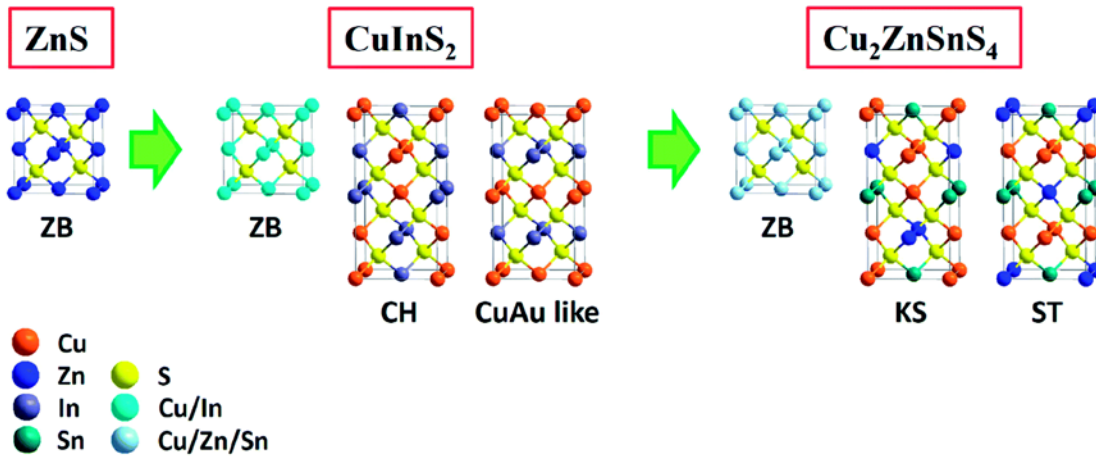

Figure 1.6: The substitution of elements in the cubic zincblende (ZB) structure to form the tetrahedral chalcopyrite (CH), kesterite (KS) and stannite (ST) crystal structures. *From: Chang, J. and E. Waclawik*[110] *Published by The Royal Society of Chemistry.*

(ZnS(O,OH)) is one prominent alternative, but has had challenges with defects and control of the O:S ratio essential to performance.[38] CIGS devices utilizing ZnS(O,OH) have achieved a maximum of 18.5% efficiency in a lab setting.[39] Other alternative buffer layers include magnesium zinc oxide (MgZnO) and indium sulfide (In_2Se_3).[40] A more recent alternative has been the deposition of a thin layer of titanium dioxide (TiO_2) on CIS, which has show efficiencies up to 9.9%.[41] These alternative buffer layers have the advantage of having a larger bandgap, which means the buffer layer absorbs less light, allowing more light to be absorbed in the p-type absorber, potentially increasing the short circuit current of the devices. The low lifetime of holes in cadmium sulfide results in poor collection of carriers absorbed in this buffer layer which is clearly visible in external quantum efficiency data of light above the band gap of CdS as shown in Figure 1.7 by the sharp decrease in collection for wavelengths below 500nm.

Integration of these novel materials into a useful photovoltaic cell requires the appropriate pairing of the electronic structure of the p-type and n-type material. When

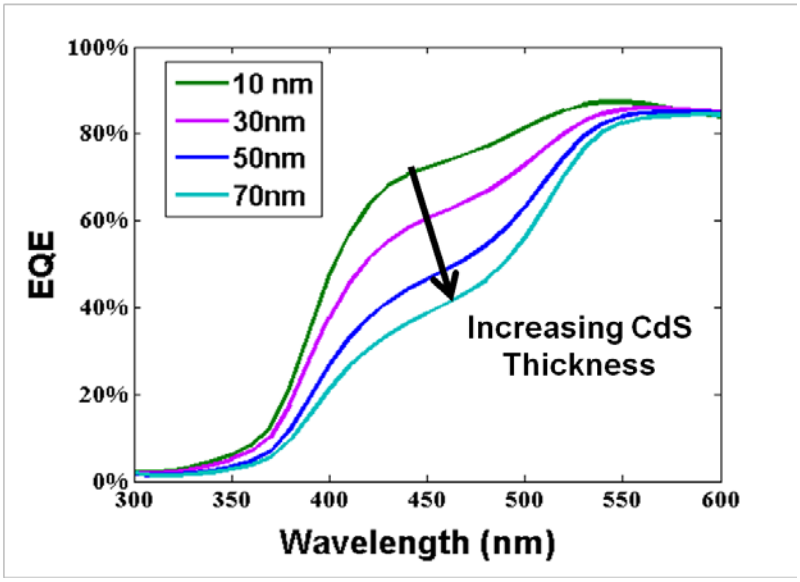

Figure 1.7 The decrease in collection efficiency caused by cadmium sulfide.

two distinct materials meet, the energies of their conduction bands and valence bands are different, as well as their band gaps. These different band structures are generally classified by the way they overlap, with band energies defined relative to the vacuum level, which remains locally continuous. When the smaller band gap lies completely within the bandgap of the larger material it is referred to as a type I band alignment. When the band gaps overlap partially, they have a type II band alignment. When they do not overlap at all they have a type III band alignment.[42] It is usually best for the band containing the minority carrier of the narrower bandgap material to be nearly continuous within a few kT. (where k is the Boltzmann and T is the absolute temperature). Since p-n diodes are minority carrier devices and most thin film cells rely on a p-type absorber with a narrower bandgap than the n-type layer, we will confine our discussion to such a system, though the principles can be easily generalized for other systems. If the n-type conduction band is slightly higher than the p-type material (type I alignment), then only electrons with an energy higher than that barrier can cross into the n-layer and then through the device, effectively lowering the J_{sc} of the device. This effect becomes very significant if the barrier is more than a few kT as very few electrons will have enough energy to cross the barrier. If instead, the n-type conduction band is slightly lower than in the p-type material, then any electrons moving to that material lose a small amount of potential, reducing the maximum effective V_{oc} of the device. This could also be viewed as losing current due to unabsorbed photons in the band gap compared to a theoretical device of lower bandgap with perfect conduction band alignment. These effects can be modeled using thermionic emission theory.[43] Figure 1.8 shows a diagram of these effects.

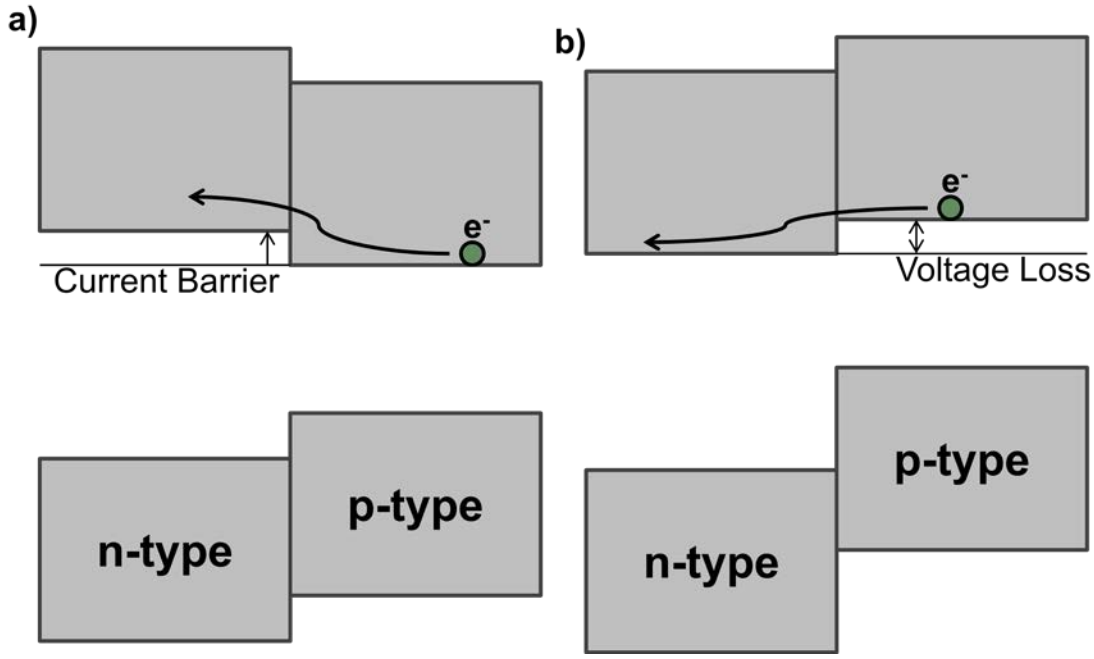

Figure 1.8: The effect of band alignment on semiconductor heterojunctions: (a) the barrier to electron flow caused by a type I alignment and (b) the voltage loss between materials with a type II alignment.

1.3 Routes to CIGS and CZTS

Researchers have produced CIGS and CZTS solar cells and thin films by a wide variety of routes. The most basic structure of these solar cells generally consists of a molybdenum(Mo) back contact sputtered on soda lime glass. Mo is chosen because of the formation of molybdenum diselenenide ($MoSe_2$) at the back contact which is credited with creating an ohmic contact and increasing adhesion.[44] The CZTS or CIGS absorber layer is formed on this back contact. A CdS buffer layer is deposited via chemical bath deposition,[45] and a sputtered layer of zinc oxide (ZnO)[46] is added to complete the buffer stack. Finally, a layer of tin-doped indium oxide[47] or aluminum-zinc oxide[48] is added as

a transparent conductor before a final nickel-aluminum grid is added to complete the cell. Figure 1.9 shows a schematic of these solar cells.

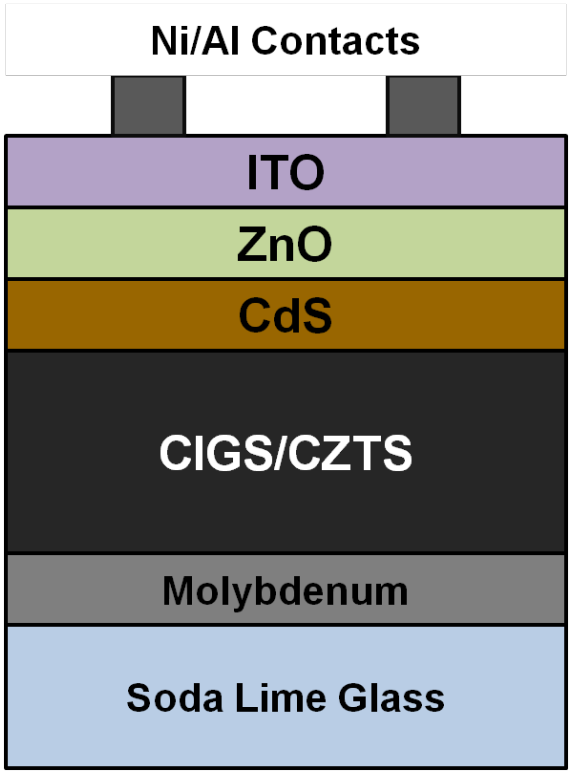

Figure 1.9: Schematic diagram of a standard thin film solar cell.

There are several methods for producing the various layers on the solar cell stack. CIGS and CZTS have been made from coevaporation,[49] thermal evaporation of the metals,[50] nanoparticle inks,[51,52] electrodeposition[53] and molecular precursors.[54] The highest efficiency CIGS cells are produced by the coevaporation of Cu, In, Ga and Se.[55] This method uses a 3-stage process with an initial In/Ga/Se deposition using coevaporation, followed by a Cu/Se deposition with the intent of forming large grains, and finally another In/Ga rich stage to control surface properties.[56] This allows for band gap grading by tuning relative ratios of In/Ga throughout the process, improving the electrical and optical performance.[57] Alternatively, individual metal layers can be

deposited via sputtering or thermal evaporation, and then reacted in selenium or hydrogen selenide atmospheres to create CIGS thin films.[50]

As both of these methods require high vacuum deposition equipment, researchers have developed alternative methods for making these cells. Electrodeposition involves applying a potential to a solution to cause ions in the solution to migrate toward and deposit on an electrode. This can be done either sequentially[58] or directly in one bath.[59] These cells, however, still lack the efficiency of some of the other methods due to challenges incorporating the elements at the right ratios as well as avoiding oxygen contamination from the generally aqueous solution.[60]

Nanoparticle inks provide an alternative method to produce CIGS and CZTS films. Nanoparticles are formed via the reaction of metal and chalcogen precursors, and hot injection into oleylamine produces a colloidal suspension of nanoparticles.[61,62] Purifying and dispersing these colloids in a suitable solvent as an ink, generally hexanethiol, allows them to be coated on Mo coated glass substrates which can then be annealed in a selenium environment to create large grain CZTS[63] and CIGS.[64] This method has been used to create 15.0% efficient CIGS solar cells,[51] and 9.0% efficient CZTS solar cells.[52]

Alternatively, pure solution methods utilize dissolved precursors in various solvent systems to spin coat material that can be annealed under inert or selenium-rich atmospheres to create films of the desired absorber layer. The best solution processed method for CIGS and the record of any method for the production of CZTS involves the dissolution of individual precursors in hydrazine: copper (I) sulfide (Cu_2S), Zn, S and Se with suspended Sn powder in the case of CZTS,[65] or Cu_2S, In_2Se_3, Ga, S and Se in the

case of CIGS.[66] This method has been remarkably successful, yielding 15.2% efficient CIGS cells[67] and a record 12.6% efficient CZTS cells,[23] but it requires the use of highly toxic and flammable hydrazine.[66]

Alternative solution systems allowing for the substitution of hydrazine are of great interest; however, they have yet to match the efficiencies of the hydrazine route. One potential alternative is dimethylsulfoxide (DMSO). Copper (II) acetylacetonate($CuAcAc_2$), zinc chloride($ZnCl_2$), tin (II) chloride ($SnCl_2$) and thiourea can be spin-coated into a precursor film. Annealing in a selenium rich atmosphere forms large grain CTZS films that have been used to make 8.3% efficient solar cells.[68] Similarly, by replacing the zinc and tin compounds with indium chloride($InCl_3$) and gallium chloride ($GaCl_3$), CIGS cells of 14,7% can be fabricated.[69]

Thiols and amines when mixed also dissolve many of the precursors for these materials. Zhang et al. prepared a 7.86% efficient CZTS solar cell by dissolving chloride precursors (CuCl, $ZnCl_2$ and $SnCl_2$) in hexylamine (HA) and propanethiol (PT) and then mixing these solutions with sulfur and selenium solutions in the same solvent. These solutions when spin coated and annealed in a selenium atmopshere produced 7.86% efficient CZTS solar cells.[70] Alternatively, Cu_2S, tin (II) sulfide (SnS) and zinc metal can be used to create a chloride-free process yielding 6.84% efficient solar cells.[71] Similarly, Zhao et al. dissolved copper (I) selenide (Cu_2Se), indium acetylacetonate ($InAcAc_3$) and gallium acetylacetonate ($GaAcAc_3$) in hexylamine and ethanedithiol (EDT) to create 10.3% solution-processed CIGS solar cells.[54] Alternatively, if ethylenediamine (EDA) is combined with EDT, thin films of CIGS can be prepared via the dissolution of elemental Cu, In, Ga and Se.[72]

In all of these cases, the absorber material is combined in a similar fashion on Mo substrates and uses the chemical bath deposition technique to deposit CdS, and RF sputtering to deposit ZnO and conductive oxides and complete the device stack.

1.4 The Structure and Use of Titanium Dioxide in Solar Cells

A popular alternative buffer or electrode material for solar cells and photocatalysis is titanium dioxide (TiO_2). Titanium dioxide is used as the sensitized layer in dye-sensitized solar cells,[73] as a common photocatalyst for the oxidation of organic molecules[74] and for the photo-electrolytic splitting of water into hydrogen and oxygen.[75] Three distinct phases of TiO_2 occur naturally: rutile, anatase and brookite,[76] while several high-pressures phases exist, the most well known of which is referred to as TiO_2(II).[77] The main phases of interest are rutile and anatase, as brookite is very difficult to produce, and the other phases are not stable at atmospheric pressure. Rutile is the most thermodynamically stable polymorph, however anatase is metastable at low temperature leading to an analogue of a phase diagram composed of reaction boundaries. This diagram is shown in Figure 1.10. Most solar and photocatalytic applications utilize the anatase phase due to the wider bandgap and improved performance of anatase.[75] This imposes a 600ºC limit on all processing steps to avoid a phase transition to rutile.

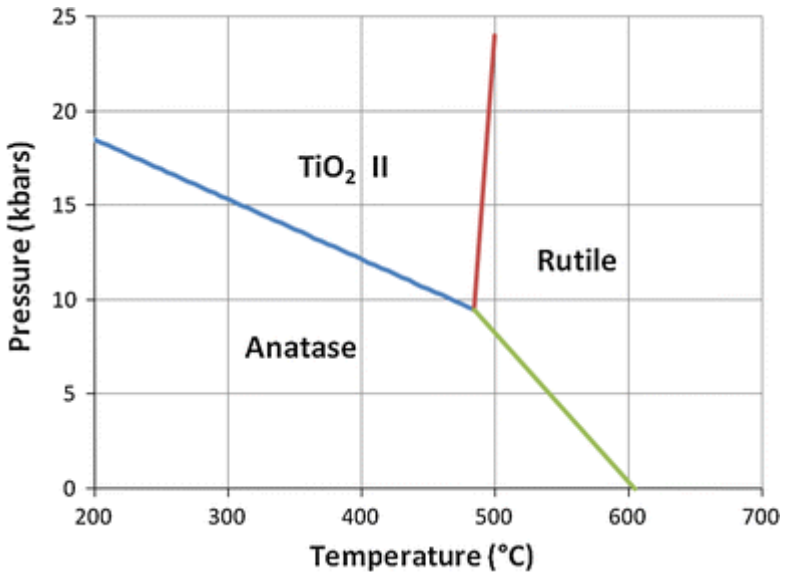

Figure 1.10: Reaction boundaries for the titanium dioxide system. *Reprinted with permission from Hanaor et al.*[77] *© Springer Science+ Business Media, LLC 2010.*

The three naturally occuring phases of TiO_2 all have octahedrally coordinated Ti^{4+} centers bound to six O^{2-} ions which are bound in a trigonal planar coordination to three Ti^{4+} centers. The major difference between phases is the relative arrangement of the ions as well as the strain and distortion from ideal bond angles. Figure 1.11 shows the unit cells of the anatase, rutile and brookite structures of TiO_2. These crystal structures yield different electrical properties for the material. As previously stated, anatase has a broader band gap than rutile, with anatase having an indirect 3.20 eV bandgap, while the rutile structure has a direct band gap of 3.03 eV.[78] Until recently the exact relative alignment of the two phases has been debated, but recent work suggests that anatase and rutile have a type II band alignment, with both the conduction and valence bands of anatase below those of rutile TiO_2.[78]

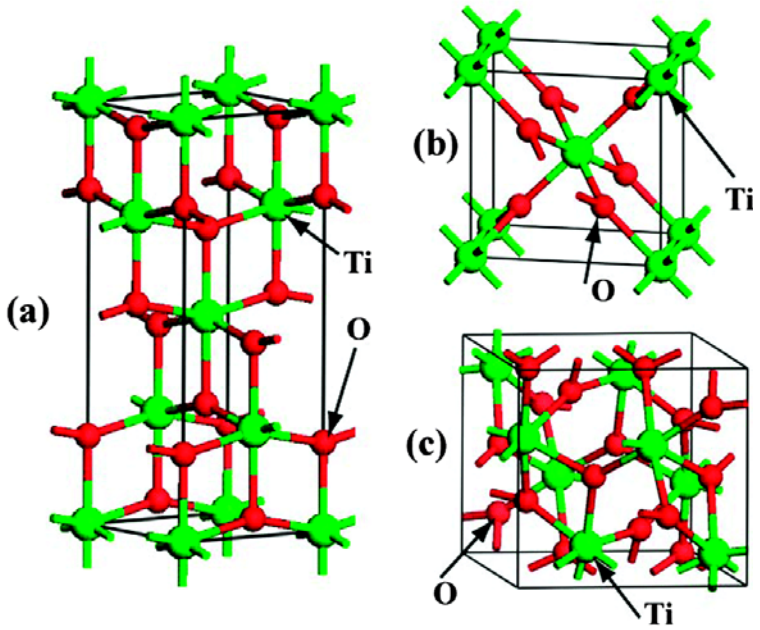

Figure 1.11: Conventional unit cells of (a) anatase, (b) rutile and (c) brookite titanium dioxide films. *Reproduced from Zhang et al. with permission from the PCCP Owner Societies.*[145]

Both the band gap and the conduction band edge are essential properties for matching a TiO_2 buffer layer with a potential absorber material. This is particularly complicated because the electron affinity of the material is surface dependent and can therefore vary with surface orientation and the methodology used to take these measurements. In 2013 two papers utilizing x-ray photoelectron spectroscopy (XPS) claimed different values for the band separation between rutile and anatase, with rutile being higher in both cases, with a conduction band offset of 0.22 eV versus 0.5 eV and a valence band offset of 0.39 versus 0.7 eV. This measured difference of approximately 0.3eV in the relative band alignment of the two materials is approximately 12 kT at ambient temperatures, and is larger than the optimal band offsets for heterojunction solar cells, and therefore makes it very difficult a priori to predict the band alignment of either phase with another solar absorber material, which would also be subject to a similar level

of error in band position measurements using XPS. As such, a relative method, such as capacitance-voltage admittance spectroscopy would be necessary to measure the band offsets between two semiconductor materials, which would require the creation of a well-bonded heterojunction between these materials.[79]

TiO_2 is commonly used as an electron-selective layer in solar cells, particularly dye-sensitized and ammonium-lead halide perovskite solar cells. Anatase TiO_2 has an electron carrier density of approximately $10^{18}/cm^3$, depending on the processing methods, resulting from shallow donor defects within the material.[80] The selective n-type conductivity is expected to occur due to oxygen vacancies intrinsically present or caused by impurities.[81] Dye-sensitized solar cells pioneered by Michael Grätzel use a mesoporous structure of ~25nm TiO_2 particles sintered together to create a high surface area compact to adhere sensitizing dye molecules. These cells are created using a viscous paste of TiO_2 deposited on fluorine-doped tin oxide (FTO) coated glass, which are then annealed to sinter the lose particles and oxidize and remove organic binders and solvents in the paste. Finally the films are soaked in an aqueous titanium tetrachloride ($TiCl_4$) solution to precipitate fine grains of TiO_2 inside the pores to increase the surface area of the material.[82] This $TiCl_4$ treatment also affects the surface electrochemical and physical properties of the TiO_2 surface, lowering the conduction band and increasing the charge transfer to the material. Organo-ruthenium complex based dyes have created some of the most efficient dye-sensitized solar cells, but other organic dyes, including naturally occurring chlorophyll and porphyrin derivatives, can be utilized as well to make these solar cells.[73] An electrolyte is used for charge selective transport to a back electrode. The highest independently verified dye-sensitized cells have an 11.9% total power conversion

efficiency (PCE) though there are more recent reports of 13% efficiency cells with novel π-conjugated sensitizing dyes. These cells also perform slightly better at intensities below 1 sun, likely due to charge transfer limitations.[83]

Most modern dye-sensitized cells utilize a TiO_2 bilayer structure with a thin blocking layer of compact TiO_2 between the mesoporous layer and the underlying FTO substrate. This layer can be formed primarily in four ways, through vacuum-based sputtering techniques, chemical vapor deposition, via the sol-gel method or via spray coating. Xia et al. used radio frequency magnetron sputtering to deposit a thin metallic titanium film under 1Pa argon, which was converted to an oxide upon annealing the film after deposition of the mesoporous TiO_2 film, improving the performance of the TiO_2 electrode.[84] Reactive sputtering with oxygen and thermal evaporation is an alternative to metallic Ti. Chemical vapor deposition involves the deposition and breakdown of gaseous species of titanium alkoxides, such as titanium isopropoxide or ethoxide, or $TiCl_4$ with water to grow thin films on a heated substrate. The substrate temperature and precursor source determine the phase of the resulting TiO_2 film, with temperatures below 400ºC yielding amorphous TiO_2, while rutile phases formed over 800ºC and 400ºC for the $TiCl_4$ and titanium isopropoxide precursors respectively. A pure anatase phase is obtained in the range between 400ºC and 600º for the alkoxide precursors.[85] The sol-gel method also uses titanium alkoxides, which are added to solutions containing water and other organic solvents such as acetic acid or alcohols. The alkoxides undergo hydrolysis as the solvents evaporate, creating an inorganic polymer as the Ti-O-Ti bonds form and alcohols are created from the alkoxy ligands. This increases the viscosity of the solution, creating a sol, or colloidal solution, that eventually forms a xerogel, which when heat

treated forms a dense film with appropriate optical and electrical qualities.[86] Spray pyrolysis is the most common method of depositing uniform, dense TiO_2 films. In this method, a solution of titanium diisoproxide bis(acetylacetonate) (TIA) in ethanol or butanol is sprayed on a heated substrate using a ultrasonic spray nozzle. Ideally this method is similar to chemical vapor deposition as the volatile solvent evaporates almost complete before reaching the substrate surface, and a smooth layer of TiO_2 is formed by the breakdown of the gas-phase titanium complexes, though some droplets may land on the surface and evaporate leaving small particles on the surface.[87]

Ammonium-lead halide perovskite cells, also known as solid state dye sensitized cells, are one of the areas of greatest scientific interest in emerging photovoltaic technologies today. Alkylammonium lead halide perovskites have been of interest since at least 1978 due to their unique layer structure and their properties as a mixed organic-inorganic semiconductor.[88] A two-step process involving the deposition of lead iodide films in ammonium iodide solutions was pioneered in the late 1990's by David Mitzi which provides a basis for most perovskite films today.[89] Perovskite materials were combined with the structure of dye-sensitized solar cells, with a thin dense buffer layer of TiO_2 combined with a mesoporous structure of TiO_2, initially yielding 3.8% efficiency.[90] The most efficient perovskite solar cells currently utilize a thin, ~200nm, layer of mesoporous TiO_2 on a 50-80nm dense TiO_2 layer, though competitive devices have been made in a purely planar structure omitting the mesoporous layer.[91] The major challenges for commercializing perovskite solar cells are stability and toxicity. Perovskite solar cells are very sensitive to moisture and heat and somewhat sensitive to oxygen, and upon breaking down contain water-soluble lead iodide which is a serious pollution concern.

Including cesium ions in the material increases the thermal stability of these cells while maintaining high initial efficiencies of 21.2% which degrade more slowly over time, though they still degrade to 18% efficiency after 250 hours of operation.[92]

Between the perovskite layer and the back contact mad of silver or gold, a hole-selective organic transport is necessary to prevent the shunting of the cell by the direct contact of the p-side electrode with the n-type TiO_2. A variety of large molecule or polymeric π-conjugated semiconducting organic materials have been used for this purpose. spiro-OMeTAD (2,2′,7,7′-tetrakis-(N,N-di-p-methoxyphenylamine)-9,9′-spirobifluorene) is the most readily available and one of the most commonly used organic hole transport layers, however alternative materials show potential for higher efficiency devices due to the low conductivity of spiro-OMeTAD.[91] Other potential materials include poly(3-hexylthiophene-2,5-diyl),[93] poly-triarylamine, PCPDTBT (poly-(2,1,3-benzothiadiazole-4,7-diyl(4,4-bis(2-ethylhexyl)-4H-cyclopenta(2,1-b:3,4-b′)dithiophene-2,6-diyl))) and PCDTBT ((poly-((9-(1-octylnonyl)-9H-carbazole-2,7-diyl)-2,5-thiophenediyl-2,1,3-benzothiadiazole-4,7-diyl-2,5-thiophenediyl)).[94] Alternatively, interest has been shown in the para isomers of spiro-OMeTAD in place of the ortho isomers to slightly alter the energy levels of the organic semiconductor.[95]

Recently there has been interest in utilizing TiO_2 as a substitute for the toxic cadmium sulfide to create a buffer layer for InP, CZTS and CIGS inorganic films and hopefully improve performance. Hsu et al. recently published CIGS solar cells created using a combination of copper and indium oxide powder precursors which were annealed in a selenium atmosphere to create thin-film CIS cells with either a CdS or a TiO_2 buffer layer. The TiO_2 buffer layer yielded slightly higher average efficiencies for this material:

9.9% vs 9.5% for the TiO_2/CIS . Atomic layer deposition utilizing alternating layers titanium isopropoxide and water was used to produce a 10nm uniform film on top of the finished device as a buffer layer.[41] TiO_2 has also been used between the conducting oxide and the CdS layer for CdTe/CdS devices as a resistive blocking layer, with a 15nm film yielding 12% efficient CdTe devices.[96] Recent work also has examined the use of the successive ion layer adsorption reaction (SILAR) to intermix a CZTS film with a mesoporous TiO_2 film with the expectation of creating a novel solar cell.[97]

1.5 Amine-thiol Solution Chemistry for Molecular Precursors

As previously mentioned, the combination of amines and thiols are a solvent of interest for a wide variety of semiconductor compounds. The use of this combination of solvents for semiconductor applications dates to 2012 when it was first used to remove excess selenium from selenide nanoparticles.[98,99] This solution gained interest for the ability of the thiol to act as a reducing agent, forming disulfides, and strongly enhance the dissolution of selenium and tellurium in amines and diamines respectively. Further, the thiol component can be removed via distillation to create a sulfur and phosphorous-free alternative to phosphine based reagents.[100,101]

More recently these solvents have attracted attention for their unusual ability to dissolve many binary semiconductors, salts and metals that normally would be insoluble or minimally soluble in either solvent alone, or most other organic solvents. As previously mentioned hexylamine and propanethiol have been used to fabricate CZTSSe solar cells with efficiencies comparable to many other solution methods.[70] When a dithiol is substituted for the primary thiols a variety of other precursors to thin film

semiconductors are soluble, including chalcogenides of copper(Cu_2S, Cu_2Se, CuS and CuSe), tin (SnS and SnSe), indium (In_2S_3, and In_2Se_3), silver (Ag_2S and Ag_2Se), as well as the pure Cu, Sn, In and Zn metals, as shown in Figure 1.12[71,102] This is particularly notable as many of these compounds are insoluble in most organic and pH neutral aqueous solutions. Also a variety of chloride and acetylacetonate salts are soluble in the amine-thiol solvent pairs. These metal chalcogenides and salts have shown themselves to be useful precursors for CZTS, CIS and CIGS films.[71,54,103] Further, Webber et al. showed that the chalcogenides (S, Se and Te) of several group V elements (Sb, As and Bi) are soluble in diamine-dithiol solutions.[104] These solvents have been used to make CuSbS2 films.[105] Similar solutions containing sulfur and amine functional groups have shown similar behavior including solutions of ethanolamine and thioglycolic acid.[106]

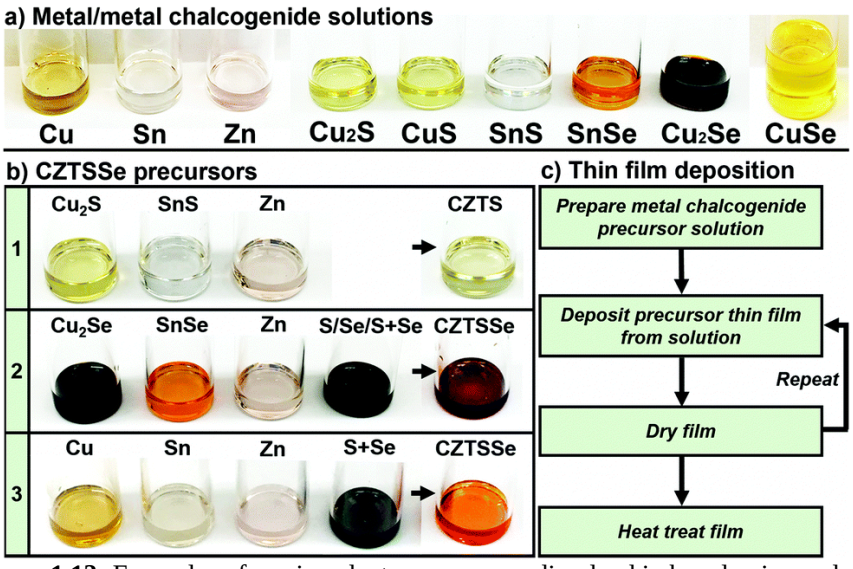

Figure 1.12: Examples of semiconductor precursors dissolved in hexylamine and ethanedithiol. *Reproduced from Zhang et al.*[71] *with permission from The Royal Society of Chemistry.*

Some preliminary work has gone into determining the structure of these compounds. A wide variety of copper, gold and silver thiolate complexes are known in

literature. In many of these structures complexes are formed by the agglomeration of several copper centers bridged by sulfur atoms bonded to two copper atoms each. Several of these compounds have been observed as ions stabilized by additional ligands as ions, as well as some neutral species. The most common of these species have 1, 2, 4 or 6 copper ions and equal or slightly greater numbers of thiolate ions depending on charge. Arylthiolates appear to be the most easily isolated, but akylthiolates are not unknown.[107] Compounds where sulfur atoms are bonded to three sulfur atoms also occur for larger structures, which have structures similar to very small clusters of Cu_2S crystals.[108] Thiolates are also known to bond to copper and gold surfaces. The copper-sulfur bond is stronger than the gold-sulfur equivalent, to the extent that the sulfur-carbon bond is more likely to break than the copper-sulfur bond when these bonds are mechanically strained.[109] The commonplace nature and stability of these complexes makes them likely to occur when dissolved, especially as ammonium ions and thiols have similar values for their pK_a. Thiolates are also reported for lead and cadmium precursors dissolved in thiols.[110]

The solutions themselves provide some evidence that the effectiveness of these solutions relies on the formation of ions pairs, as mixtures of thiols and dithiols with ethylenediamine show a sharp increase in conductivity relative to the pure solvents.[71,104] Buckley et al. have recently combined ^{119}Sn NMR, raman spectroscopy and thermogravometric analysis to suggest that tin ethanedithiolate complexes are the likely species in solution for tins complexes.[102]

CHAPTER 2. CADMIUM SULFIDE AS A BUFFER LAYER

2.1 Introduction and Motivation

Cadmium sulfide has been a common feature of thin film solar cells since their initial creation in the 1950's.[7,9] When used in solar cells, optimization of the thickness of the cadmium sulfide layer is essential for efficient device performance, and several publications discuss the importance of optimizing this value to minimize optical losses without degrading device diode performance.[111–113] This optimization had not been performed on our specific nanoparticle ink device structure, as the CdS recipe we used was copied exactly from literature. Additionally, the only process control was the deposition time, as no in situ measurements were implemented and post-treatment measurements are difficult and unreliable due to the surface roughness and the need to proceed with device fabrication without excessive exposure to air and moisture.

The goal of the research presented in this section was to optimize the deposition conditions and thickness of the CdS layer for nanoparticle-based CZTS films, which would hopefully apply as well to CIGS films. Further, an in situ measurement technique was implemented to monitor and optimize the deposition thickness and provide a more effective control for the film properties. A liquid-phase quartz crystal microbalance was used to measure the thickness while a Teflon(PTFE)-coated type T (Copper-Constantan) thermocouple was added to measure the bath temperature during the process.

When an electromagnetic wave traverses a barrier between to transparent or semi-transparent materials with different dielectric functions (and therefore indexes of refraction), part of the light is reflected backwards. When multiple thin layers of with thickness similar to that of the wavelength of the electromagnetic wave are present, these reflections interfere with the incoming radiation, and form a standing wave interference pattern within these layers. Depending on the ratio between the wavelength and the thickness, this interference can be constructive or destructive resulting in increased transmission through the barrier or increased reflection at the barrier.[114] This is the same principle by which anti-reflective coatings are added to solar cells. Optical management of transmission, reflection and absorption is essential to ensure the maximum amount of light is transmitted through the barrier layers of the device stack and absorbed within the absorber layer. Winkler et al. modeled the optical behavior of ITO-CdS stacks on their CZTS devices, showing that the minimum thickness that obtains good coverage gives the best transmittance of light to the absorber layer as shown in Figure 1..

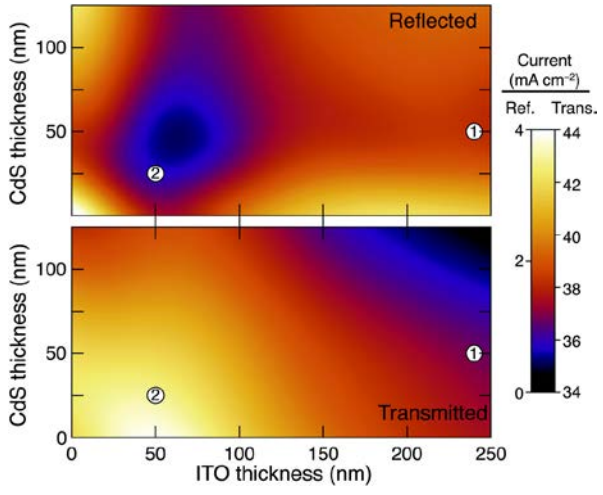

Figure 2.1: Optical reflectance and transmission based on CdS and ITO thickness. *Reproduced from Winkler et al.*[146] *with permission from The Royal Society of Chemistry.*

Earlier research showed that increasing the thickness of the CdS layer by increasing deposition time generally increased open circuit voltage (V_{oc}), shunt resistance (R_{SH}) and fill factor (FF) increasing the efficiency of these devices while having few changes in short circuit current (J_{SC}) as increased overall carrier collection offset some of the losses due to the undesired absorption of photons in the CdS layer.[113] Optimal thicknesses were found to be between 60 and 80nm. However, a partial electrolyte treatment of the absorber film by soaking in aqueous cadmium sulfate ($CdSO_4$) and ammonium hydroxide solution (NH_4OH) solution has been shown to increase the performance of thinner films, allowing a higher J_{SC} without sacrificing a V_{OC} and R_{SH}. It is expected that diffusion of cadmium into the top few angstroms of the absorber film helps reduce shunting and improve performance.[113,115]

For CdS bath deposition two deposition mechanisms are used to explain the behavior of CdS bath deposition. The aqueous solution is made by the mixing of $CdSO_4$, NH_4OH and thiourea. The reaction process begins with the addition of the thiourea, at which point CdS begins to nucleate and deposit. Cadmium sulfide particles can nucleate in solution and then precipitate out of solution, depositing on the film surface, or cadmium sulfide can grow expitaxially, atom by atom, directly on the surface.[116] Either process may occur independently, or both may occur simultaneously, depending on the relative growth and nucleation rates. These mechanisms are shown in Figure 2.2. Past studies have found that the surface-mediated deposition mechanism begins first, forming a dense layer, but over longer reaction times, a porous layer begins to be incorporated from solution-deposition.[117] Higher cadmium concentrations and lower pH tend to promote solution precipitation, while lower pH and smaller NH_4OH concentrations,

higher temperature, and higher $CdSO_4$ and thiourea concentrations speed deposition rates.[118] Where reported, the structure of the CdS films has generally been reported as hexagonal-wurtzite, though a cubic zincblende-like structure also exists for CdS.[112]

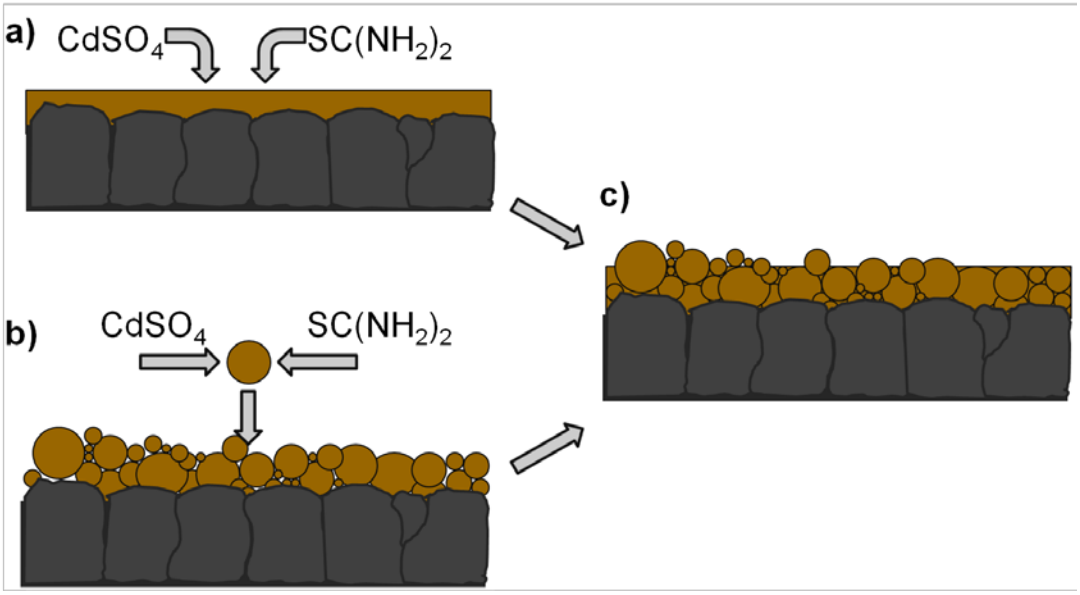

Figure 2.2: Three possible mechanisms can occur for CdS deposition: (a) surface-mediated expitaxially growth, resulting in a dense film (b) solution-precipitation growth resulting in a porous film, or (c) mixed growth incorporating both mechanisms (a) and (b)

2.2 Experimental

For these experiments devices were made using several batches of CZTS nanoparticles with the recipe and procedure more fully explained in Miskin et al.[52] All chemicals were ordered from Sigma Aldrich and used as provided unless otherwise noted. Oleylamine (OLA) was obtained from Acros Organics with 80-90% C-18 content and purified using a freeze-pump thaw to remove entrained gases. All water used is filtered using a Milipore ultrapure water filtration system with approximate resistivity of 18 MΩcm.

The nanoparticles are prepared by dissolving 1.65 mmol copper(II) acetylacetonate , 0.984 mmol zinc acetylacetonate dihydrate and 0.93 mmol tin(VI) bis(acetylacetonate) dichloride, (99.99% trace metal basis) in 7.5mL OLA at 60ºC, and for a basis of slightly less than 0.5M metal precursors (adjusted for non-stoichiometric compounds). In a separate flask, 6.0 mmol of sulfur is dissolved in 6.0mL of OLA to make a 1M sulfur solution. In a three-neck flask 12mL of OLA is purified under argon atmosphere using a schlenk line attached via a condenser. Three purges under vacuum lasting 5 min each are performed at room temperature, and three more at reflux temperatures between 130ºC and 140°C. The three-neck flask is then heated to 225ºC and 6mL of the metal precursor solution are added using a 6mL disposable syringe and a rubber septum. Thirty seconds later, 4.5mL of the sulfur solution was added to the flask. The temperature drops slightly on injection to slightly below 200ºC, but an Omega PID temperature controller maintains the flask at the desired 225ºC. The flask is kept at 225ºC for 1hr after injection, at which point the heating mantle is removed and the solution is allowed to cool naturally to ambient temperature. The resulting mixture is separated into two 30mL PTFE centrifuge tubes with the remainder filled with isopropanol (IPA) and spun or 5min at 14000 RPM in a Beckman Coulter X22 series centrifuge. The particles are decanted re-suspended as a colloid with 1-2mL of hexanes with a vortex mixer and then washed again. Any dark supernatant is collected and added incrementally with methanol and spun down again to minimize any losses. Three total washes with IPA and three more with 30 %IPA and 70% methanol are performed before the particles are dried under argon and weighed, yielding approximately 250-300mg of nanoparticles per batch.

Inks are prepared by suspending nanoparticles in hexanethiol at 200mg of nanoparticles per 1mL of hexanethiol. On each 2"x1" molybdenum coated (800nm) piece of glass, 15μL of ink are spread in a line, and the sample is coated by passing a rounded glass rod three times back and forth while supported on rails that are thicker than the sample by the width of one layer of Scotch^{TM} magic tape. After each coating, the samples are heated on a 300°C aluminum hotplate in air to remove excess solvent. Two coatings are performed per sample to give an approximately 1 micron nanoparticle film. These films are annealed for 40min in a 3"x1" graphite box with 260mg of gray selenium pellets in a tube furnace under argon at 500ºC for 40min.

After annealing in a selenization furnace, the samples are stored in a vacuum desiccator between all other steps. The CdS deposition is carried out differently depending on whether the quartz microbalance is used. For the standard conditions without the quartz microbalance, a jacketed flask is heated with 65ºC water, and the samples are suspended inside the flask from polypropylene clips. A solution containing 150mL of ultrapure water, 22mL of .015M $CdSO_4$ (Alfa Aesar 99.996%) stock solution and 28mL of ammonium hydroxide (30% by weight, JT Baker) is added to the flask, and the samples are added soaked in the solution while stirred by a magnetic stirrer. After 1minute from the addition of the first solution, 22mL of .75M thiourea (>99% Alfa Aesar) solution is added directly to the stirred solution. The deposition continues for 11min and the solution should slowly become a slightly opaque yellow by the end of 11min. The samples are the removed and quickly rinsed with ultrapure water and IPA and dried in an oven at 120ºC for 5minutes before 150nm of ZnO and 300nm of ITO are deposited using

a radio-frequency magnetron sputtered. Finally Ni-Al grids are deposited using an electron-beam evaporator.

When a quartz microbalance is used, the experimental setup is slightly changed. An Inficon Research Quartz Crystal Microbalance controller is used with a 1" liquid-cell holder. The capacitance cancellation for the microbalance is carefully adjusted to remove any effect of the capacitance from the holder and connections before use. A specially designed 500mL jacketed flask with a 1" port and O-ring replaces the standard flask. Inficon 1" 5Mhz polished quartz crystals with a Ti-bonded gold contact are used to measure the deposition rate. These contacts are chosen for their acid resistance allowing convenient cleaning and reuse. This crystal is cleaned via immersion in hydrochloric acid immediately after deposition and further rinsed with ultrapure water. Since the microbalance frequency is sensitive to temperature and environment, the 150mL of ultrapure water is added and stirred in the covered flask for 1hr to equilibrate with the jacketed beaker. A thermocouple monitors and records the temperature of the bath. The remaining procedure proceeds as previously stated, except that the computerized data logging begins immediately after the addition of thiourea and proceeds until the monitor first reaches the desired thickness. The quartz microbalance is expected to show a reduced resonance frequency of 27.5 hz per 1nm of CdS deposited on the crystal, and a tooling factor of approximately 1 is found for the solution (which is expected according to the surface-mediated growth mechanism[117]). The stirring and liquid motion gives the quartz microbalance much lower resolution than a comparable gas-phase reaction, and approximately 10-20hz of noise is observed, resulting in resolutions of approximately 1nm. Further, the temperature of the solution varies slightly and in all cases is

significantly lower than the jacketed beaker temperature. For these runs, a beaker temperature of 50ºC, 65º and 80ºC results in an equilibrium deposition temperature of 47ºC, 59ºC and 67ºC ±1ºC respectively. For convenience we will report results with the jacketed flask temperature, as temperature fluctuates and cools approximately 7-10ºC upon the addition of the reagents.

Powder x-ray diffraction (pXRD) on selenized films was performed using Bragg-Bretano focusing in a Rigaku Smartlab X-ray diffractometer with a flat plate stage. For nanoparticle films and CdS films, grazing inident pXRD (GIXRD) is used with a 0.5º incident angle to provide greater sensitivity to these very thin films.

External quantum efficiency (EQE) data was obtained by using a xenon arc lamp with a monochrometer at a wavelength resolution of 10nm. A motorized chopper operating at 60hz and a lock-in amplifier were used to separate the response from any ambient light. The AC current response was compared to that of silicon and germanium standard solar cells obtained from Newport Corporation with known wavelength responses as a calibration to determine the relative response of the devices.

2.3 Results and Discussion

When measured using the quartz microbalance, a non-linear early growth rate is measured, appearing to have a short induction period. In all cases, the temperature drops immediately after added the thiourea solution, and as a quartz microbalance is sensitive to temperature changes, it is unclear if the behavior is due to a delay in nucleation, or simply due to the temperature drop. A temperature drop of about 7°C-10°C is observed upon adding the thiourea solution. Since the microbalance returns to its initial

temperature before the reaction is complete, this will not affect the final deposition measurement, but the initial rate is not observable in the quartz microbalance frequency, as the effects of temperature on reaction rate, the temperature effect on the vibration frequency, and any induction or nucleation period are convoluted in this range. Figure 2.3 shows the thickness as measured using the quartz microbalance and the temperature through a standard deposition process, with time t=0 corresponding to the addition of the thiourea. Note that the negative initial thickness is a temperature-based anomaly in the crystal behavior.

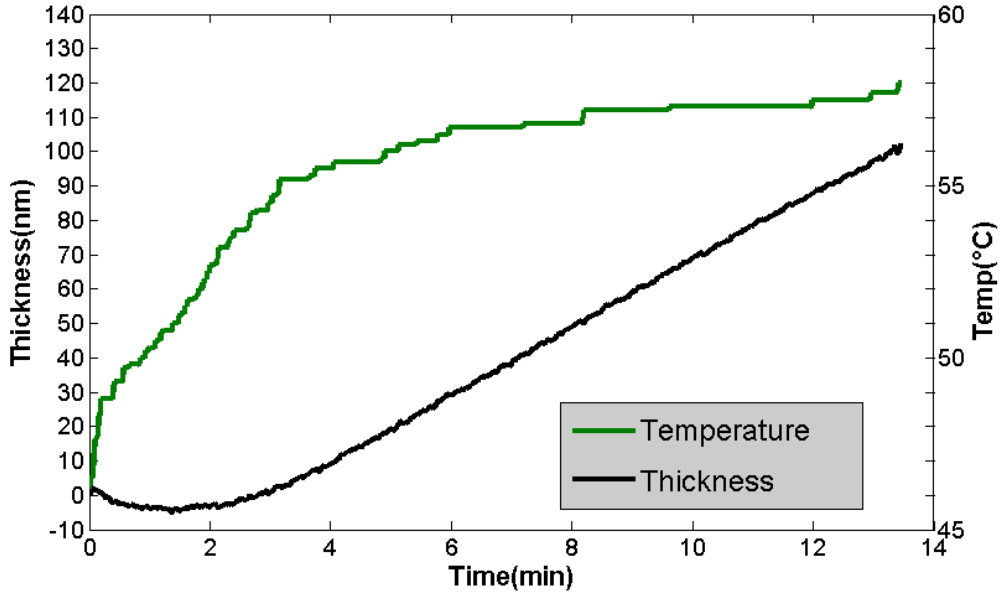

Figure 2.3: The measured thickness of deposition with a 65°C water bath showing both the temperature decrease and the apparent induction period in the deposition rate.

As would be expected, the hotter reactions proceed much more rapidly, however they show less uniformity. Particularly, at 80°C, the deposition is clearly uneven with colored streaks appearing due to the flow lines around the surface of the material. Below this temperature, remarkable uniformity in thickness and appearance is observed

throughout the device. Reducing the temperature gives better control over thickness and uniformity at the expense of longer reaction lengths. Figure 2.4 shows the thickness profile during the reaction for three nominal temperatures, 50°C. 65°C and 80°C. Note that the measured temperatures are 47°C, 59°C and 67°C respectively. In each case there is an immediate decrease in measured thickness (increase in frequency) as the temperature drops on addition of the thiourea solution. It is also important to note that 50nm of CdS are deposited at 10 min into the reaction, about 1min earlier than when the reactants are not preheated. This can be explained by the slightly higher starting temperature since the water is preheated for use with the microbalance.

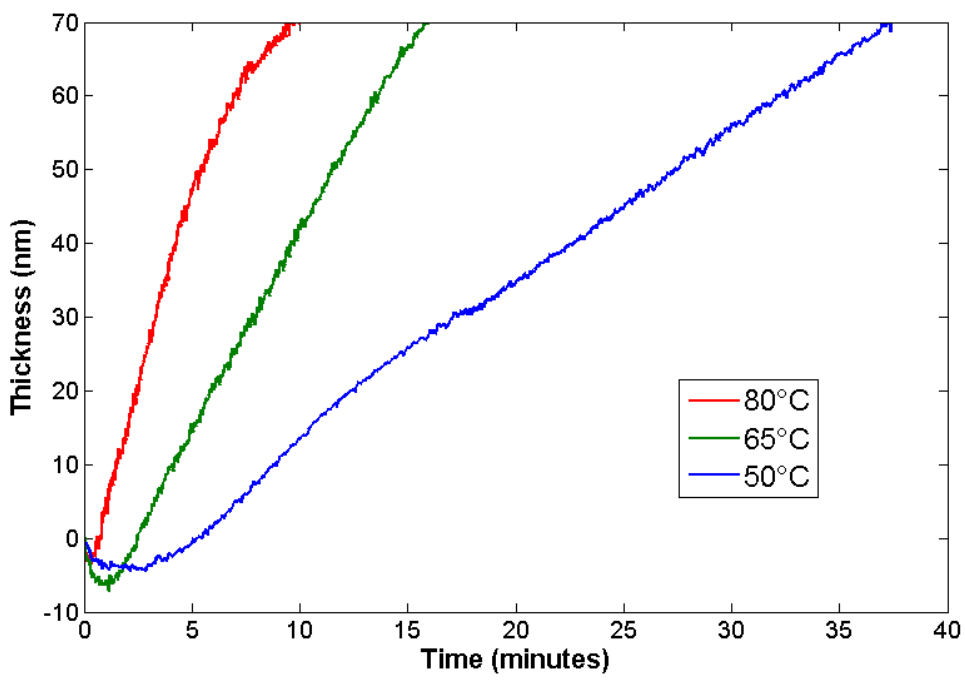

Figure 2.4: In situ thickness measurements showing the growth rates at various temperatures of water bath.

The reaction appears linear initially, but over long periods of time as the quantity of $CdSO_4$ in the solution depletes, the reaction rate decreases, effectively limiting thicknesses obtainable in a single deposition at just over 200nm. Figure 2.5 shows the slowing behavior over long periods of time for CdS deposition. The reaction proceeds mostly linearly for the first 70nm of deposition, but slows afterwards as the limiting reactant is depleted. As such, for deposition thickness much over 70nm it may be beneficial to utilize multiple bath depositions to achieve that thickness.

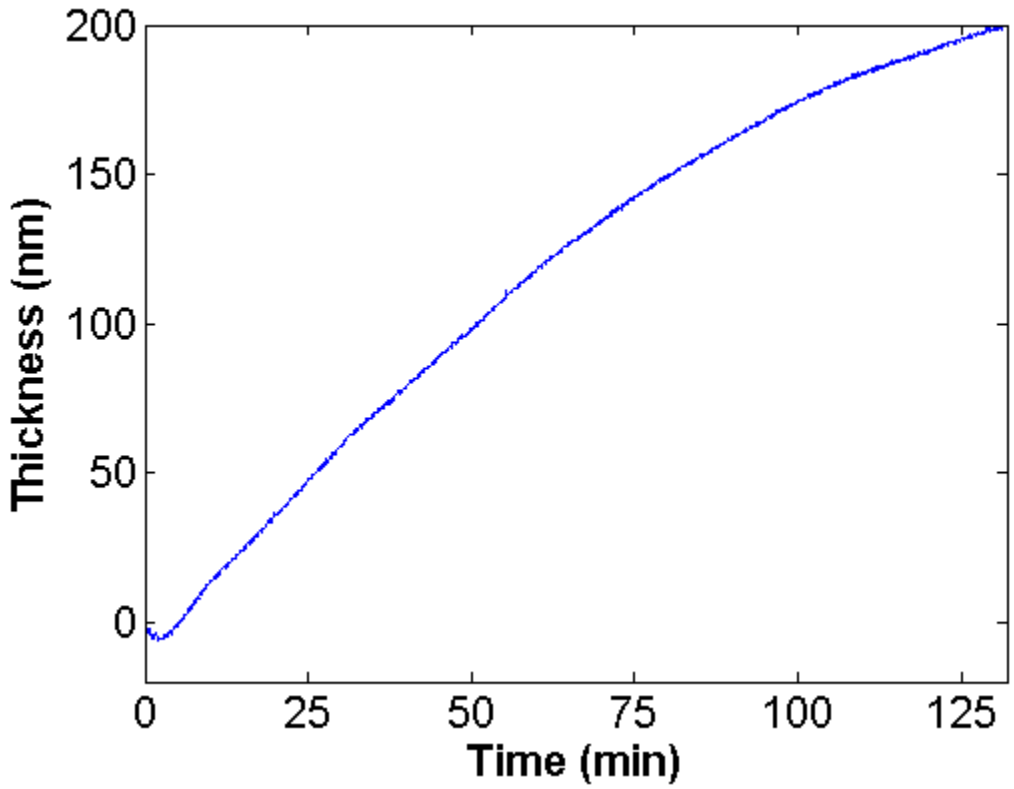

Figure 2.5: The measured CdS for a much longer run length with a bath temperature of 50°C, clearly showing the nonlinearity of the deposition process. The reaction rate slows significantly after the first 70nm of deposition.

Unlike what is commonly reported in literature, the cadmium sulfide does not form a pure hexagonal phase. Figure 2.6 shows the GIXRD diffraction pattern of a

200nm CdS film on soda-lime glass with an incident angle of 0.5°C compared to reference standards for both phases.[119] The cubic-zincblende phase is dominant, though the shoulders on the 26.75°C peak indicate that there is likely some presence of hexagonal-wurtzite regions. The lack of secondary peaks for these phases indicates that their percentage is likely small. It is unclear why we observe different phases than reported from literature from an identical process. The full width at half maximum (FWHM) of the dominant peak at 26.75° indicates approximately 5nm crystal domains according to the Sherrer equation, though some angular broadening is likely from the parallel beam x-ray focus necessary for GIXRD, so this estimate is likely an underestimate of the actual crystallite domains.

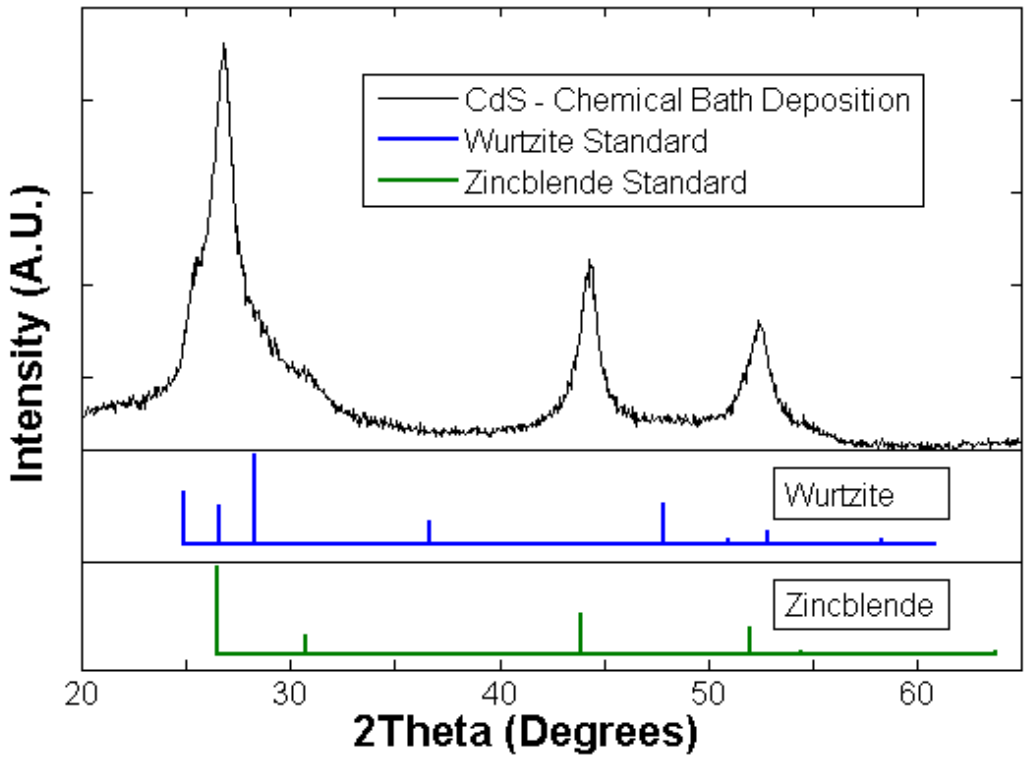

Figure 2.6: Observed GIXRD spectrum of as deposited CdS filmwith an incident angle of 0.5°C compared to known standards of both the known zincblende and wurtzite phases.[119]

When deposited on CZTS the color spectrum is a strong indicator of thickness. The color of the original film is a medium gray, however upon deposition of the CdS the color ranges from gray-violet at 10nm thickness, to deep purple, blue and finally teal at 30nm, 50nm and 70nm respectively. This is a useful approximate check to ensure that deposition has been carried out to the desired thickness. These color differences remain even after deposition of the ZnO/ITO buffer stack. There is no noticeable variation in color between samples with the same thickness but deposited at different temperatures. Figure 2.7 shows these various colors of CdS films at these thicknesses as well as a coating on CdS on glass. This color difference is not due to the intrinsic yellow color of cadmium sulfide, but instead the effect of reflection and absorption-based interference patterns in the thin film.

Figure 2.7: Physical appearance of CdS films on CZTSSe at various thicknesses (a) before application of the buffer layer, (b) after application of the buffer layer, and (c) of 200nm CdS on soda lime glass.

Over these ranges, the increased CdS thickness improves device performance by significantly increasing the shunt resistance and open circuit voltage while only slightly decreasing the short circuit current. Sets of 12 devices (.47cm^2 area) for each condition were prepared with equivalent thicknesses of CdS at 10nm, 30nm, 50nm, and 70nm with nominal bath temperatures of 50°C, 65°C and 80°C. Figure 2.8 shows the effect of the CdS thickness on the key device parameters, with the solid lines representing averages while the error bars represent one standard deviation on the mean for the set of devices. Efficiency, V_{OC} and fill factor all increased over this thickness range while J_{SC} was only minimally affected. This performance is mostly due to the greatly increased shunt

resistance that comes from thicker CdS buffer layers, which increases from 77 Ωcm^2 to 1140 Ωcm^2 as the thickness increases from 10nm to 70nm, as shown in Figure 2.9. This resulted in an increase in average efficiency from 6.4% to 7.3% between the standard 50nm layer and the 70nm thickness. These devices remain below the efficiency of the champion devices reported at 9.0%, though as a direct comparison partly due to the lack of antireflective coatings, a thick unsintered layer observed as shown in Figure 2.10, and partly because Miskin et al. only report their champion device efficiency.[52] By comparison, our champion device at 70nm shows 8.7% efficiency without antireflective coating, and is comparable, if slightly lower than the best reported in literature. Table 2.1 shows a summary of the key device performance values by thickness.

Table 2.1: Device performance

Thickness (nm)	Efficiency	Voc (mV)	Jsc (mA/cm2)	Fill Factor	Shunt resistance (Ωcm2)
10	4.1% ± 1.4%	287 ± 50	30.7 ± 2.2	54.8 ± 6.8	77 ± 34
30	5.6% ± 1.2%	338 ± 26	30.1 ± 1.2	62.0 ± 6.3	250 ± 140
50	6.4% ± 0.7%	359 ± 12	30.0 ± 1.5	63.5 ± 3.1	880 ± 380
70	7.3% ± 1.0%	381 ± 22	30.2 ± 1.8	65.7 ± 2.0	1140 ± 370

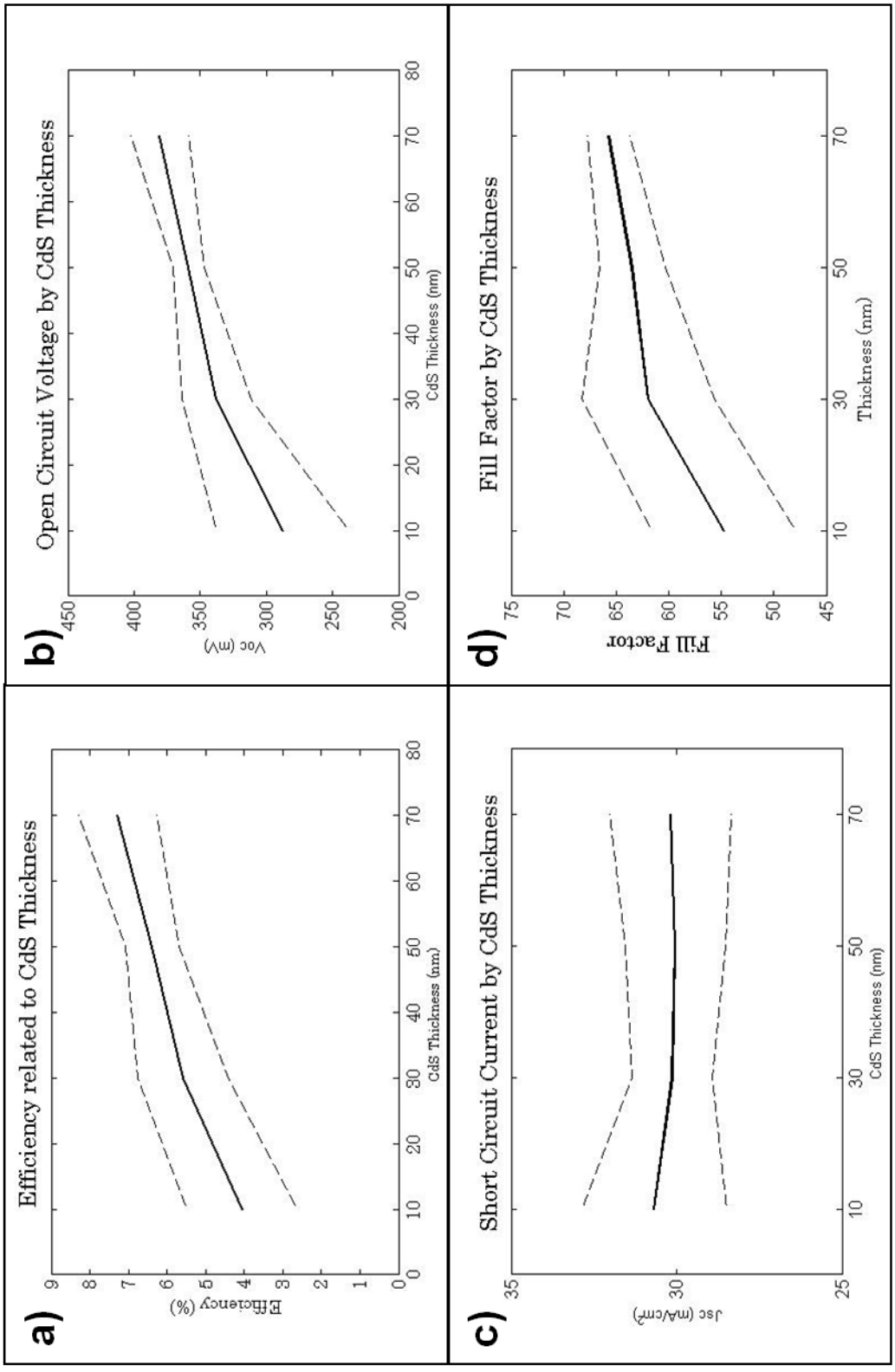

Figure 2.8: The effect of CdS film thickness on major device parameters,(a) efficiency, (b) V_{OC}, (c) J_{SC} and (d) fill factor.

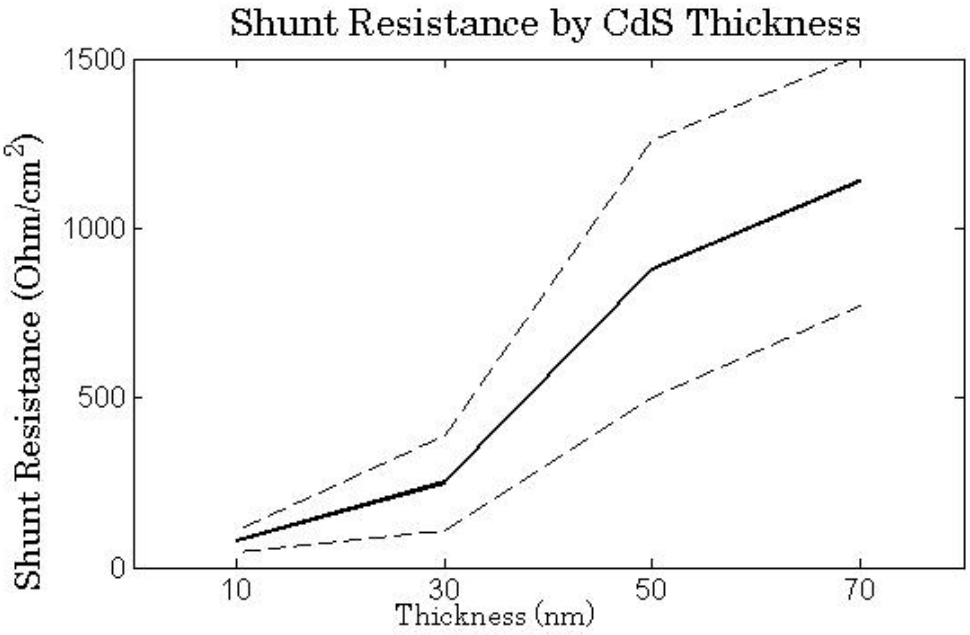

Figure 2.9: The increasing shunt resistance for increasing CdS thicknesses.

By comparison, temperature has only a modest effect on the device performance; however the lower temperature at 50°C give a slightly better and better controlled device performance. This may be simply due to the longer exposure effectively recreating the effect of partial electrolyte treatment as discussed in literature, or it may be due to better control and slower deposition rates relative to the convective mass transfer rates. For the 50°C devices the JSC decreases far less at higher thicknesses of CdS relative to the 65°C case, giving better efficiencies. Also, the 80°C case shows the erratic nature and irreproducibility that results from the very rapid reaction rate. Figure 2.11 shows the device performance with respect to temperature for the various thicknesses.

Figure 2.10 shows a cross-section of a completed CZTS nanoparticle device. The large fine grain layer is the likely cause of the lower performance relative to the champion cells in literature.

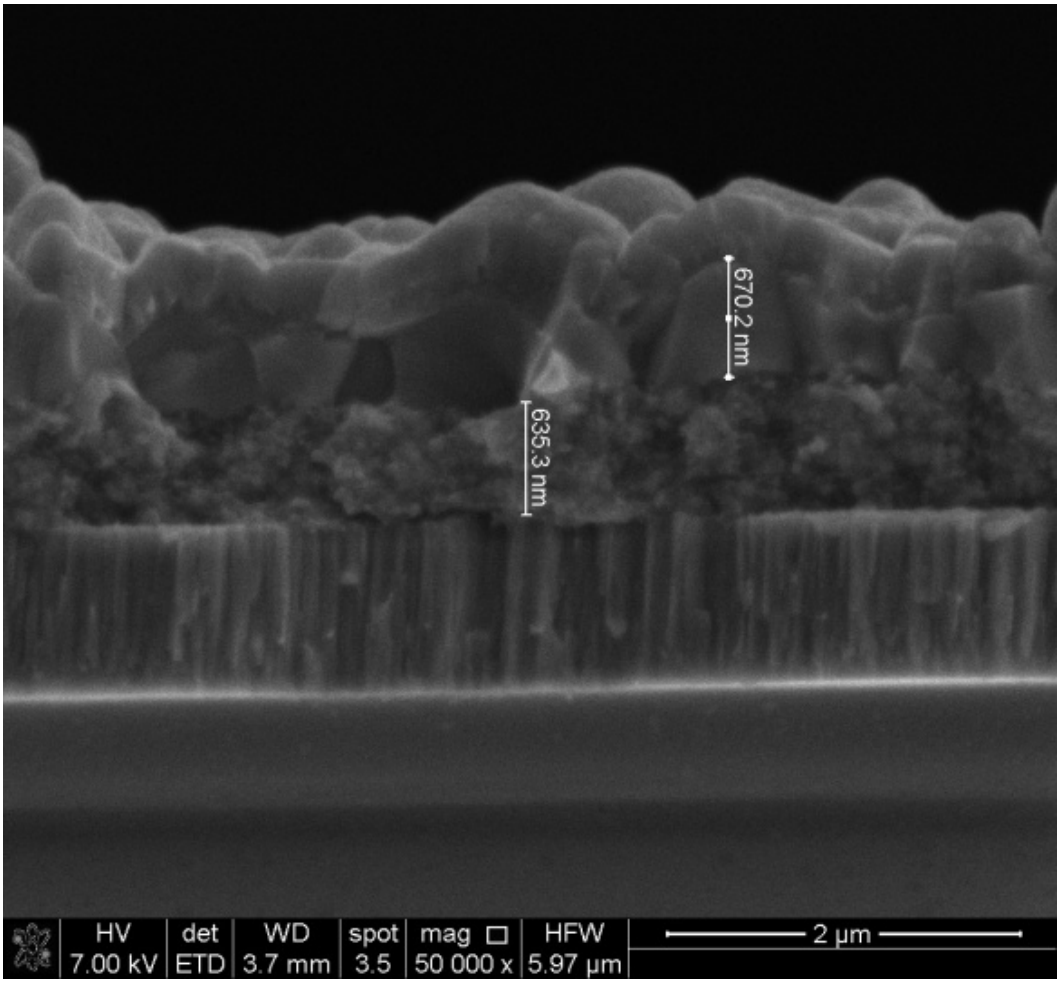

Figure 2.10: Cross section SEM image of a CZTS device showing the relatively thick 635nm fine-grained CZTS layer and the 670nm large grain layer.

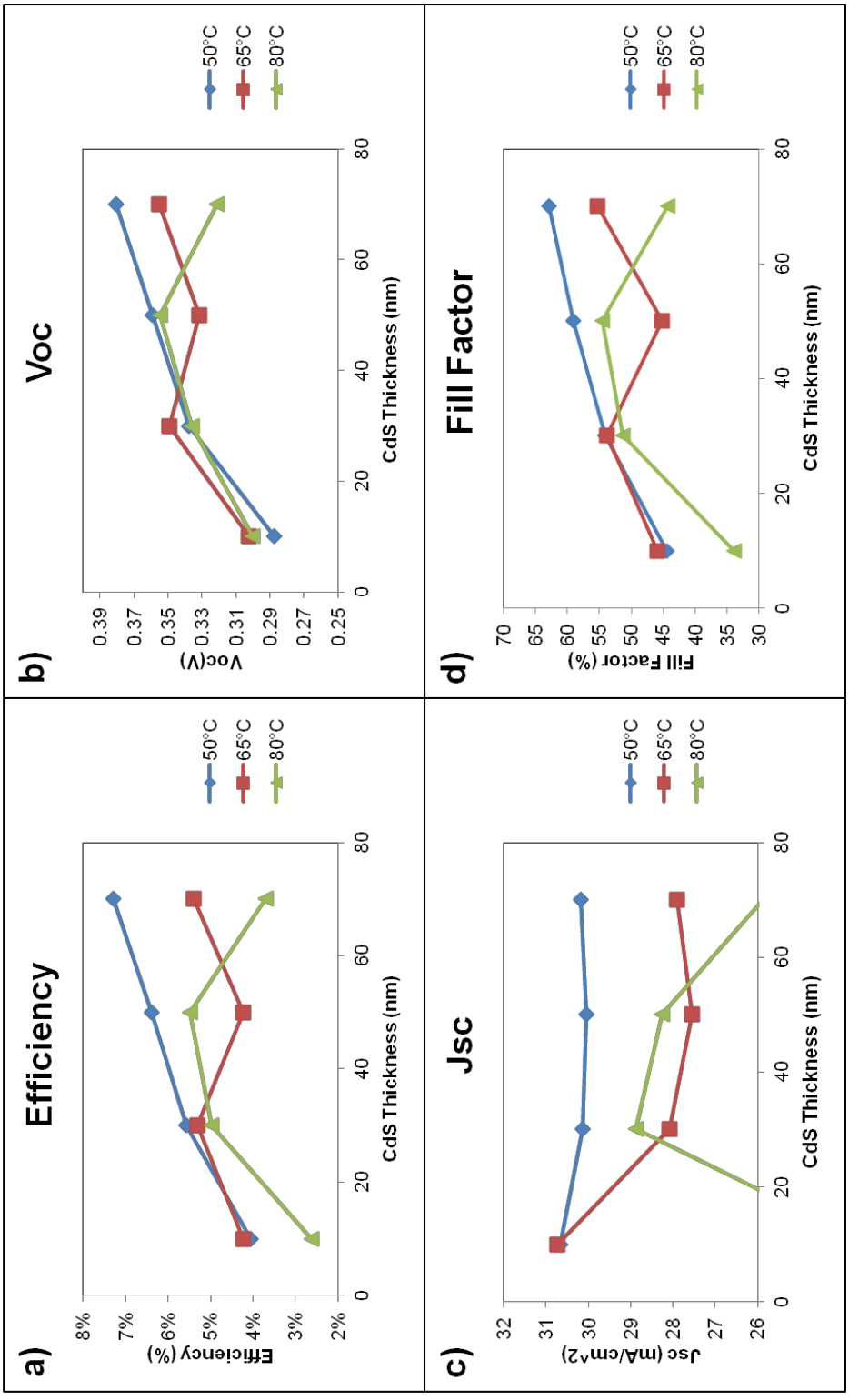

Figure 2.11: The mean device parameters separated by temperature of CdS deposition bath: (a) efficiency, (b) VOC, (c) Jsc and (d) fill factor.

It is surprising that the device short circuit current only decreases slightly though the CdS thickness increases, absorbing more light. From the current-voltage (J-V) data, it is not possible to determine if this is because the light absorbed in the CdS creates electron-hole pairs that are able to reach the device contacts or if the devices absorb more efficiently at all wavelengths to make up for the electrons lost at the blue end of the visible spectrum, especially as the solar spectrum contains far more photons in the infrared than the blue end of the visible spectrum. EQE data as shown in Figure 2.12 clearly shows the reduced absorption below 500nm, as well as the better overall collection over a range of longer wavelengths with the thicker CdS layer. The slight anomaly at 1050nm is the result of a shift between the Si and Ge calibration standards.

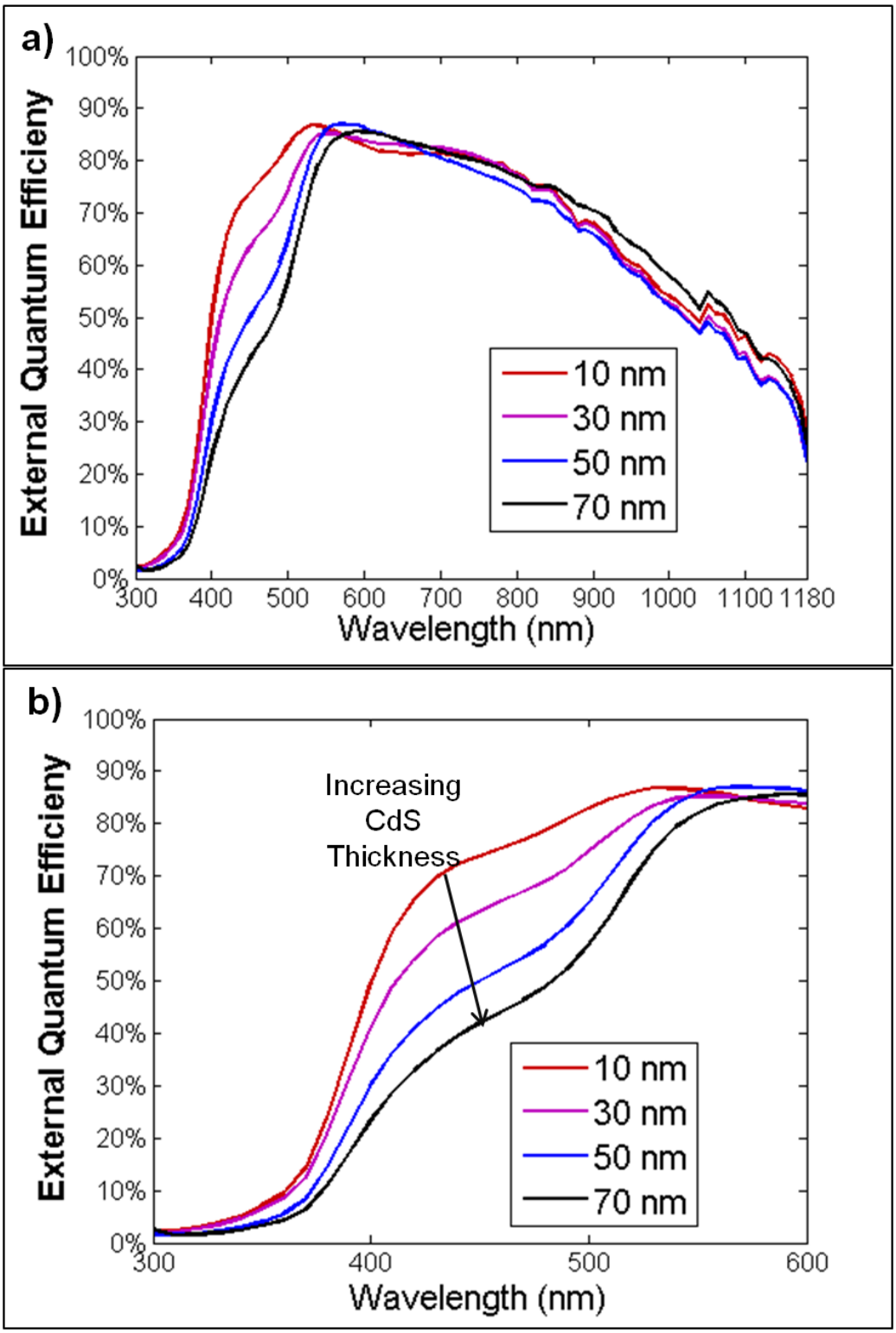

Figure 2.12: (a) EQE of CZTS devices with CdS deposited at 50°C averaged from 3 locations on 2 devices. (b) A detail of the wavelengths below 600nm illustrating the absorption by the CdS layer.

2.4 Conclusions and Future Work

The use of a liquid phase quartz crystal microbalance has been shown to allow an effective in situ control for the deposition of CdS thin films on nanoparticle-based solar materials. For these devices, CdS thicknesses of around 70nm were found to be optimum in agreement with the results of Contreras et al.[113] This result does not preclude the development of an optimal device created with a thinner CdS layer, allowing more current into the device, as a partial electrolyte treatment is reported as improving the performance of thinner CdS layers in literature. The role of this partial electrolyte treatment also indicates the importance of the timing of placement of the absorber layers in the $CdSO_4$ bath, as the length of time constitutes a short partial electrolyte treatment. Further, the initial temperature of the bath is a key factor in the early reaction rate for deposition. It may also be necessary to obtain a smoother surface to minimize shunting and allow a more uniform and therefore thinner layer of CdS. Lower temperatures also offer more reliability and control for devices, at the expense of longer deposition times, but will save research time by increasing repeatability and efficiency.

Further work should be performed integrating this process into the standard production for high-efficiency CIGS and CZTS devices to ensure the results are the same for all nanoparticle devices. Further, work should be performed to determine if the effects of partial electrolyte treatments found for vacuum-processed cells has a similar effect on nanoparticle-based solar cells. Finally, an investigation of the phase purity of the CdS layer could improve the device efficiency by reducing defects caused by the intermixing of the two phases which exhibit slightly different band structures, which could create defects and increase recombination in the CdS layers.

CHAPTER 3. FABRICATION OF TITANIUM DIOXIDE FILMS

3.1 Introduction and Motivation

Titanium dioxide films on fluorine-doped tin oxide coated (FTO) glass have been used as electrodes for dye-sensitized solar cells and emerging perovskite solar cells.[87,94] Various methods have been used to make these films, including spray pyrolysis, spin coating, atomic layer deposition and dip coating.[86,87,120] This chapter explores the creation and characterization of TiO_2 films that can be combined with traditional and thin-film inorganic semiconductors such as CZTS and CIGS or novel, emerging materials such a copper antimony sulfides ($CuSbS_2$).[121] Only very recently have devices using these combination of materials in a heterojunction cell been reported.[41] Structures include a dense TiO_2 blocking layer directly on the FTO with or without a mesoporous layer formed atop using TiO_2 nanoparticles.

These methods rely on a variety of metal-ligand complexes derived from titanium tetrachloride ($TiCl_4$) which is hydrolyzed with water directly to form TiO_2 or reacted with alcohols or acetylacetone derivatives to form titanium alkoxide compounds. These reactions have been known for more than sixty years, but only in the last twenty have been used to manufacture solar cells.[122] The most common material for spray pyrolysis is a solution of titanium diisoproxide bis(acetylacetonate) (TIA) . Several alcohol solvents are commonly used to dilute and stabilize the TIA solution, including ethanol,

isopropanol and butanol.[123,124] Until recently ethanol was the most common solvent used, however research has shown that the formation of ethoxide-complexes such as titanium diethoxide bis(acetylacetonate) (TEA) is detrimental to the film properties because it is more stable and breaks down at higher temperatures. This improved stability results in more liquid droplets hitting the surface as opposed to vapor phase complexes, creating pinholes and rougher surfaces for TiO_2 films deposited via spray pyrolysis when ethanol is used, decreasing device performance.[123] Reported concentrations of the TIA in solution range from 0.05M to 0.2M. Substrate temperatures during deposition must be at or above 400°C in order to form anatase TiO_2 with lower temperatures yielding amorphous TiO_2 layers, possibly due to incomplete dehydration of the hydroxyl terminated titanium intermediates.[125] Thicknesses from 25-100nm are commonly reported as blocking layers, with layers needing to be thick enough to minimize the effect of pinholes while remaining thin enough to not impart significant series resistance to the device.

The mesoporous layers are traditionally formed from the deposition of TiO_2 nanoparticles in a paste with organic binders such as ethylcellulose and stabilizers such as α-terpineol. These pastes can be made from a variety of commercially available TiO_2 particle sources and sizes, including mixed phase $TiCl_4$ fumed gas particles, or pure anatase particles from sulfuric acid synthesis. Pastes are reported in literature with average sizes from 20nm to 160nm, but as the larger particles are no longer commercially available, most pastes are formulated using the 25nm anatase powders.[126] Fully prepared pastes tailored for screen-printing are available commercially from the Swiss-based Solaronix and Australian-based Dyesol. While these pastes are optimized for screen

printing the ~20μm layers commonly used for dye-sensitized cells, they can be diluted shortly before use in ethanol and spin-coated onto substrates to get thinner layers, such as the ~200nm layers commonly used for perovskite solar cells.[127]

In all cases a high temperature anneal in air occurs after deposition for both the dense and mesoporous TiO_2 layers at 450-500°C to burn off excess organics and to sinter the particle layers. A treatment with an aqueous $TiCl_4$ solution follows, altering the surface chemistry and morphology to better adhere dyes and accept excited electrons. While this step has been used to improve performance for a significant amount of time, more recently it has been shown to deposit small nanoparticles in the pores, theoretically increasing surface area. Additionally, the treatment also slightly alters the surface band structure encouraging charge transport to the TiO_2 buffer layers.[120,128]

3.2 Experimental Setup and Procedures

Titanium diisopropoxide bis(acetylacetonate) was obtained from Sigma Aldrich as a 75% by weight solution in isopropanol and used as provided, as was the 99.8% anhydrous n-butanol. Solutions of the two were made in a nitrogen-atmosphere glovebox with the butanol measured by weight and the TIA solution by volume. Dyesol 18NR-T titania paste was diluted with Coptec 200 proof ethanol from Decon Labs, and then mixed using a vortex mixer until the suspension appeared uniform and no separate paste was visible adhered to the side of the vial. This suspension was the sonicated for 20min in vial in a water bath to ensure uniform mixing. The FTO glass substrate was obtained from Sigma Aldrich as 12"x12" pieces with 13Ω/sq nominal resistance, which were scored and broken down to 1"x1" pieces. Van der Pauw sheet resistivity measurements

on 1"x1" pieces confirmed the resistance was between 13-14Ω/sq for all measured samples.

The spray pyrolysis was carried out using a Sonotek 20W ultrasonic atomizing nozzle, with a 20mL glass syringe and syringe pump. Deposition was carried out at 30% of maximum power and 120khz sonic frequency with the nozzle mounted 15cm above the mounted substrate. Nitrogen at 5PSIG was used as a carrier gas. The nozzle was mounted above a custom-built hotplate, consisting of a 1"x4"x1/2" steal plate with 4 300W 1/4" diameter cartridge heaters spaced evenly within the plate, attached to a perpendicular set of Lexium MDrive stepper motors. A 3/16" ceramic plate was placed between the hotplate and the motors to protect the motor assembly from any damage from the high temperatures used for the hotplate. The stepper motors raster the sample over a 1.4"x1.4" area centered on the nozzle flow. Each individual pass of the substrate consists of 7 passes spaced by 0.2" each with the entire pass over the substrate requiring a total of 1min. Calibrations with a type k (nickel-chromium) thermocouples inside the hotplate and atop the hotplate correlated the surface temperature of the hotplate to the internal temperature of the hotplate which is controlled by an Omega PID controller. The temperature was calibrated to 520°C internal temperature which correlates to a 400°C temperature atop a 2mm sample of FTO glass. The TIA concentrations, flow rates of the solution and the number of passes were adjusted to control the thickness and quality of the film. If the flow rate becomes too low or unsteady, the nozzle "spits" or has intermittent flow, resulting in incomplete atomization which creates sub-micron droplets on the surface of the TiO_2 substrate, resulting in a rough texture and individual spots that can create pinholes. The films were examine using a Quanta 3D FEG scanning electron

microscope and a KLA-Tencor profilometer to measure uniformity and thickness of the samples.

To prepare the dense layer films, FTO glass was cut into 4"x4" pieces by scoring from the back. This glass was then carefully cleaned by the following protocol: rinsing thoroughly with water, drying under nitrogen, wiping thoroughly with isopropanol, methanol and then isopropanol again. It was washed with water then sonicated for 20 min in Alconox detergent. Another rinse removes the residual alconox, and the sample is sonicated in ultrapure water for 20 minutes. Finally, the sample is rinsed again with ultrapure water, dried under nitrogen, and placed on a spincoater at 2500 RPM for 1 minute. During the first 20s of the spin coating cycle, the sample is sprayed with ultrapure water from a spray bottle. The resulting glass should not show any hydrophobic spots during the last rinses. This glass is cut in 1"x1" pieces which are stored until use.

After solutions of TIA in butanol are prepared, they are added to a glass syringe and attached to the syringe pump and spray nozzle. The stage is preheated, while the spray nozzle is started up at 30% power and 120khz. It is important to visibly inspect the spray stream to make sure no intermittent spitting behavior is observed. If it is, lubricating the syringe body can help. If no carrier gas is flowing, this spitting noise is audible from the ultrasonic nozzle. Once the stream is regularized, carrier gas can be turned on, and the spray nozzle temporarily covered to prevent deposition on the sample during preheating. If the liquid flow is stopped, the solution may heat and deposit TiO_2 in the nozzle, or begin spitting upon resuming, so instead it should be physically covered while the sample glass s heating. A thin glass slide acting as a mask should cover ~3mm

of one side of the FTO to present a future electrical contact. When the sample is equilibrated, the cover is removed and the sample stage proceeds to raster back and forth across the sample for the desired number of passes. The spray nozzle should be covered immediately after, and the sample carefully removed and placed on aluminum rails with minimal contact to cool and minimize the thermal shock on the glass. To remove any organics and further sinter the TiO_2 grains, the sample is annealed on a ceramic hot plate at 500°C in air for 1 hour, while covered with an aluminum foil or other metallic coating less than 1cm in height to minimize heat losses to convection and radiation to maintain a more uniform heat profile across the glass substrate.

The mesoporous layers are prepared directly on these films if desired. The uncoated part of the FTO should be marked from behind as it becomes difficult to see upon deposition of the mesoporous layer. The dilution of Dyesol 18NR-T paste in ethanol is prepared as previously stated. The FTO sample is placed on a spin coater and 200μL of the diluted paste is applied roughly uniformly to the surface. Spreading the suspension across all parts of the surface minimizes the effect of surface tension and yields a more uniform final film. The spin coater is then immediately run. The mesoporous layer was optimized at approximately 400-500nm per coat under the following conditions: TiO_2 paste is prepared by dilution at 100 mg of paste per 1mL (789mg) of ethanol, and the spin coater is run for 10s at 1000 RPM, which is increased to 2500 RPM for 10s, then decreased to 1000 RPM for 10s providing a slow spin down. Wiping the uncoated FTO edge with a lint-free wipe or q-tip soaked in isopropanol easily removes the paste from the contact region. The film is then annealed on a hotplate at 300°C for 5 minutes to remove any organics before a second layer is applied, effectively

doubling the thickness to 800-1000nm. Thicker films can be obtained by using lower spin-coater speeds, however films thicker than ~500nm tend to show visible wave patterns radiating from the center of the glass substrate, indicating uneven thicknesses, and are more prone to cracking. A thickness of 200-400nm is suitable for perovskite devices, but for inorganic absorbers, a thicker layer of around 1micron maximizes optical absorption. These mesoporous films are then annealed on a hotplate at 500°C for 30min and covered as previously described. Before heating, the films should be transparent or semi-transparent and white. Small defects may be present at the corners of the square devices from the spin-coating stage but should not exceed 1mm. During heating, the films should turn a caramel-brown color briefly before returning to a clear state. Examine the films in reflected light to observe any major non-uniformities in the film quality before proceeding.

Before deposition, a $TiCl_4$ treatment is used to prepare the pore surfaces for use. $TiCl_4$ reacts strongly with water vapor and water at ambient temperature, fuming and creating TiO_2 smoke and hydrochloric acid, so safety is of utmost concern. It should only be exposed to air in a fume hood, and only when completely unavoidable. 100mL of a 0.2M $TiCl_4$ solution in water is prepared by measuring 97.8 mL ultrapure water and transferring to a 500mL Pyrex beaker, creating water just over 1" deep. A larger quantity of solution can be prepared if 100mL will not completely cover the TiO_2 samples. This water must be cooled below 4°C in an ice bath before proceeding. Higher temperatures increase the premature precipitation of TiO_2 and may pose a safety risk. Under and inert atmosphere in a glovebox 2.2mL of $TiCl_4$ should be transferred to a sealed vial. If this $TiCl_4$ contacts air it will immediately begin to fume. When the water has reached below

4°C, the $TiCl_4$ is carefully added to the water in a fume hood using appropriate PPE. A yellow residue may form on the side of the beaker or vial if the $TiCl_4$ is exposed to water vapors. A few mL of cooled water will immediately dissolve this allowing the $TiCl_4$ to be more accurately transferred. A magnetic stir bar is added and the beaker placed on a hot plate to stir. Polypropylene clips can secure two films back to back touching only the uncoated FTO portion, and the films are then placed in the solution. The solution should be heated to 60-65°C for 20min to allow the $TiCl_4$ to react. After 20min, the samples are removed and rinsed thoroughly with ultrapure water and then baked a final time at 500°C for 30 minutes. The samples are now ready to use.

3.3 Results and Discussion

A variety of TIA concentrations and numbers of passes were tested to build a correlation between the deposition thickness and the parameters such as the number of passes, concentration of TIA, and flow rate. A reasonable simplistic correlation should assume that the thickness is proportional to the amount of TIA sprayed on the material. A constant deposition rate should be expected after a possible short induction period as the surface properties should remain approximately constant once deposition has begun. As such a simple model for low to moderate flow rates can be predicated with C_{TIA} being the concentration, n_{passes} being the number of passes, and $\dot{V}$ being the volumetric flow rate:

$$C_{TIA} n_{passes} \dot{V} = constant$$

However, while this simple assumption applies relatively well for ethanol based solutions, for the butanol solutions some non-linear behavior is observed with regards to

concentration. This may mean the kinetic rate law for the deposition is different for the two precursors, as the ethanol solutions appear linear, while the constant appears to have some quadratic basis with regards to concentration for the butanol solutions. Figure 3.1 shows the calculated constant from 0.05M solutions to 0.2M with apparently linear dependence with a non-zero intercept. This may be because while TEA is known to be in monomeric form in solution,[122] a butanol-substituted derivative may stabilize better in dimers compounds as was originally hypothesized for the TIA solution due to steric hindrance though to my knowledge no work has been done to confirm this for the butanol form. Alternatively, the liquid phase of the ethanol solutions may predominate, while for butanol it remains a gas-phase reaction.

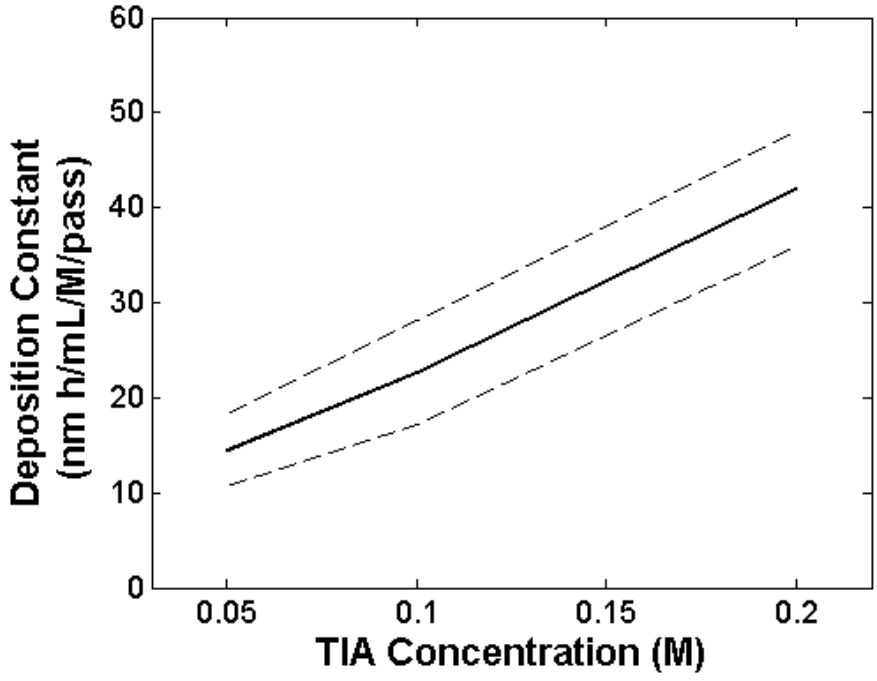

Figure 3.1: The observed constant measured by TiO_2 thickness obtained from various TIA solutions in butanol divided by the TIA concentration, flow rate and number of passes. The dotted lines are one standard deviation for the population of measurement, showing relatively similar variability.

However, the constant remains relatively similar with regard to number of passes and flow rate, as predicted before. Figure 3.2 shows the obtained measurements for the 0.2M TIA solutions in butanol. The mean stays relatively constant, however for lower flow rates and numbers of passes, there is significantly more variability. This is due to the lower total film thicknesses, which result in much more significant errors in the profilometer measurement due to differing thicknesses in the glass and the slight gradient at the edge due to shading from the mask. At flow rates below 6mL the nozzle was much more prone to intermittent spraying and spitting, resulting in more variable film thickness and quality.

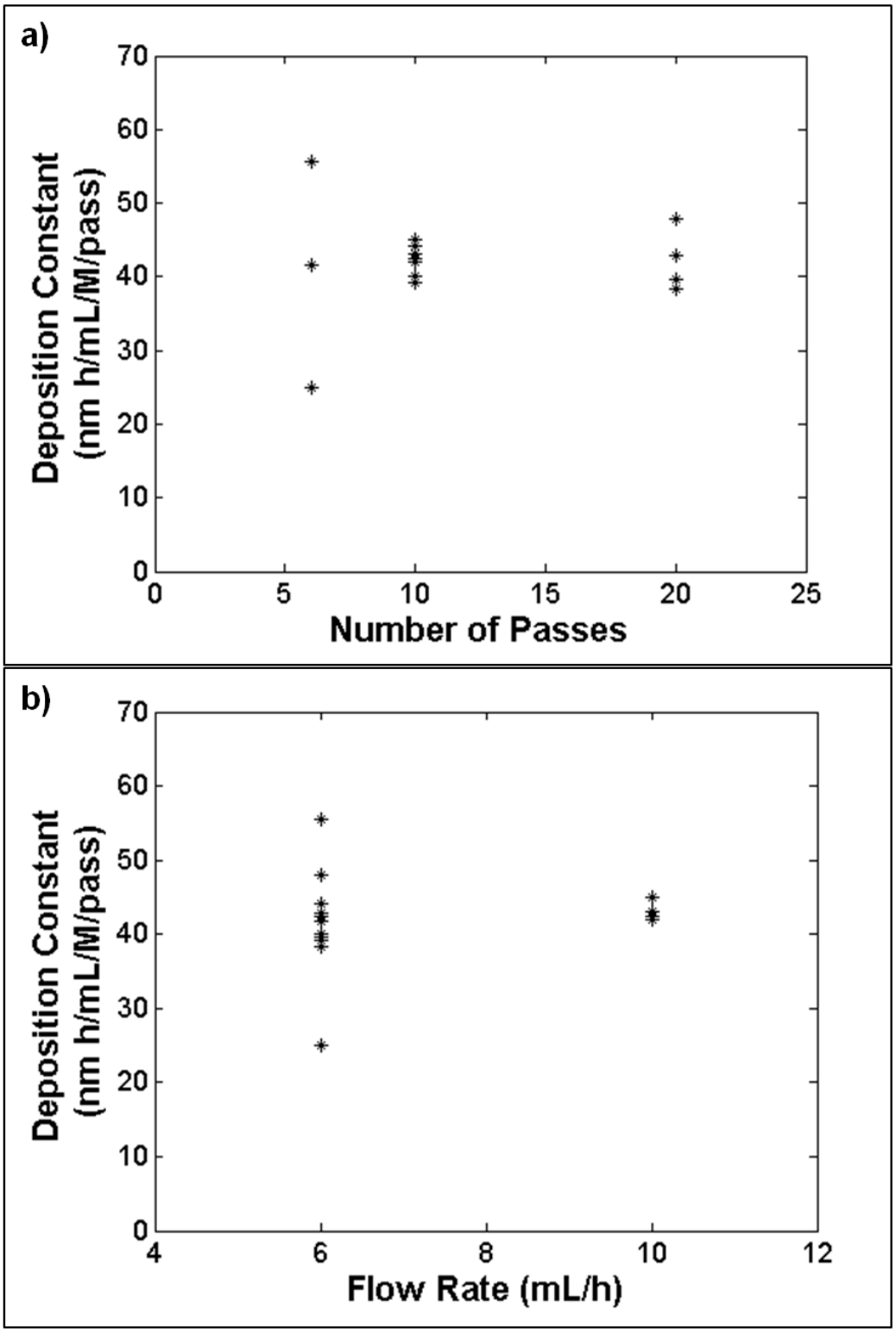

Figure 3.2: The effect of (a)number of passes and (b) flow rate on the deposition of dense TiO_2 films, showing the relative linearity of the deposition with regards to these variables.

The phase of the TiO_2 films was determined by creating thicker films at multiple TIA concentrations of 0.2M and 0.1M solution in ethanol with 16 passes each. When the sample was maintained above 400°C, an anatase structure was observed in a thin-film pXRD measurement. Below this temperature the films remained slightly dark and showed no XRD signal. Figure 3.3 shows the XRD pattern of each film which both agree strongly with a database anatase standard, though they exhibit some preferred orientation as shown by the relative intensities of the first and second peaks between the two samples.

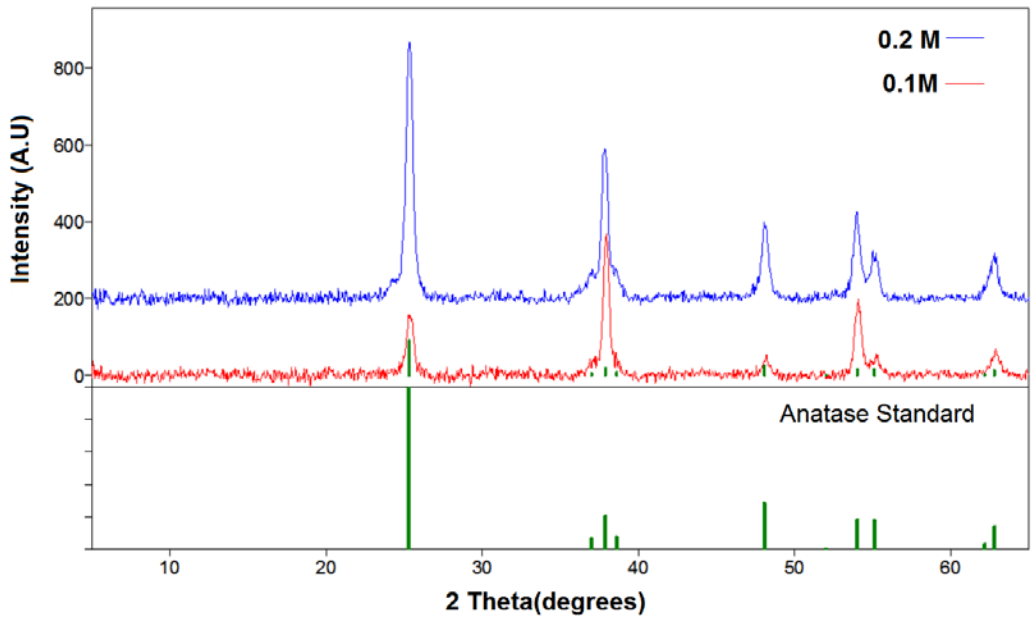

Figure 3.3: X-Ray Diffraction pattern of TiO_2 as deposited for 0.2M and 0.1M TIA solutions in ethanol.

SEM images illustrate and support many of the observations made, particularly in terms of film quality. Significant charging occurs due to the low conductivity of TiO_2 and glass, so these images do show some blurring. Figure 3.4 shows commonly observed defects resulting from liquid droplets forming on the surface either due to intermittent operation or due to the use of ethanol as a diluent resulting in incomplete breakdown in

the gaseous phase. The samples shown were deposited using 0.2M TIA in ethanol at 20mL/h with 16 coats and 2 coats respectively.

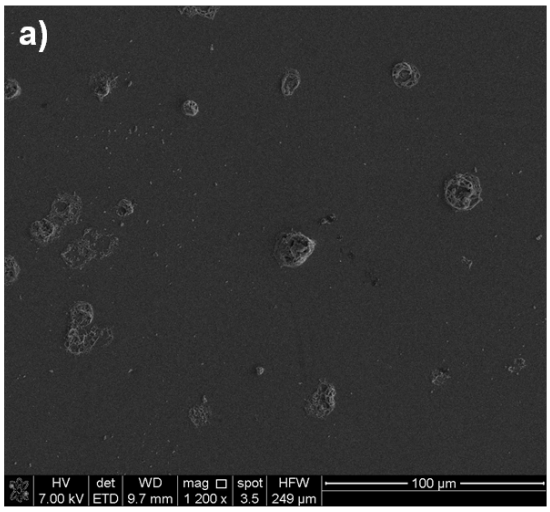

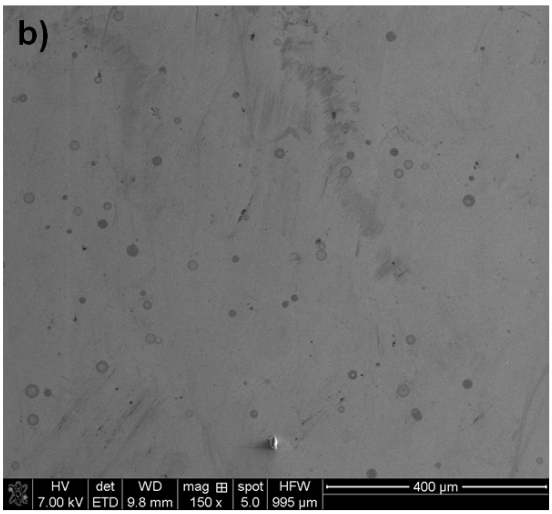

Figure 3.4: SEM images of common defects associated with liquid droplets reaching the surface, (a) showing the pinholes created by larger droplets from intermittent spitting, and (b) showing the defects created by smaller droplets creating by the slower breakdown of ethyl derivatives of TIA.

Figure 3.5 illustrates the surface texture of FTO glass and the fine conformity of the TiO_2 films to the surface for the butanol solutions. These involve 0-4 coatings of 0.05M TIA solution in butanol at 10mL/hr. The rough structure of the bare FTO glass is preserved, but slightly blurred by the deposition of thin layers up to about 25nm as shown, however even after 10 coatings we observe similar structures. The butanol solution gives much more uniform coatings.

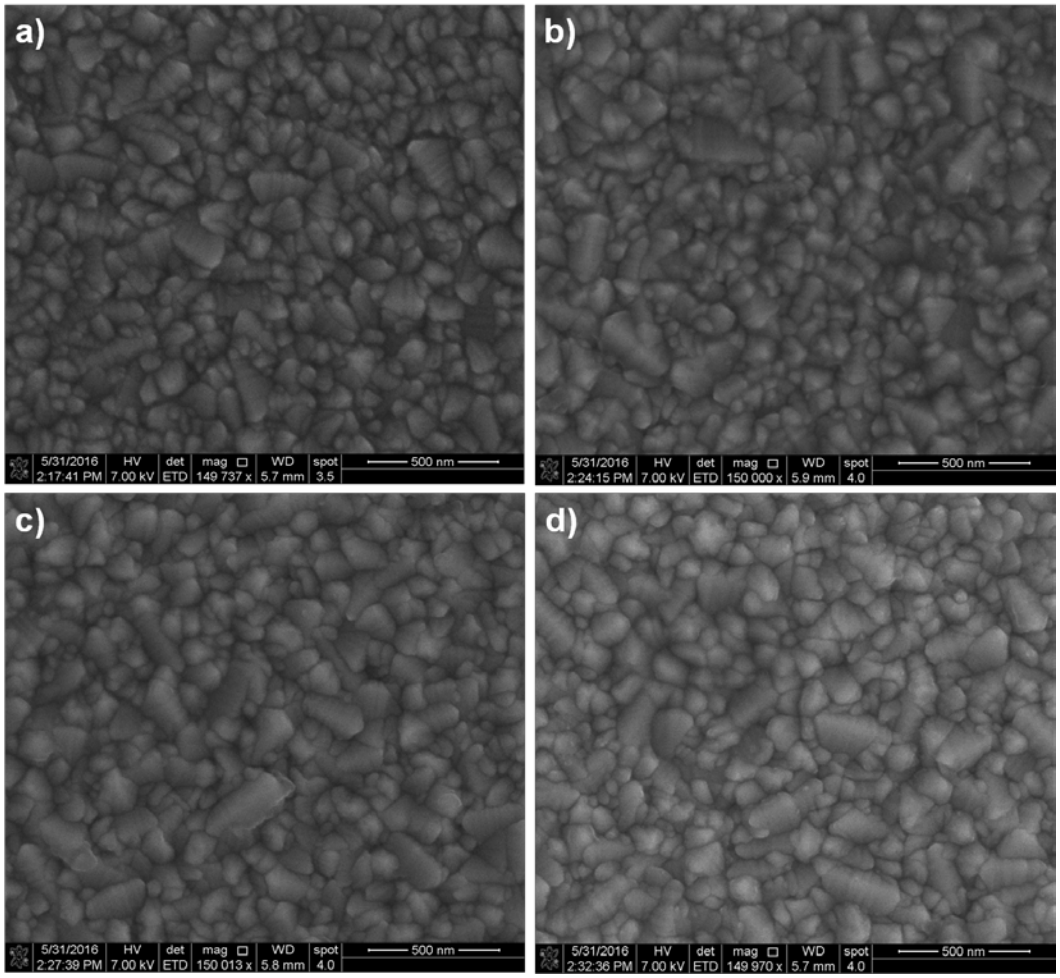

Figure 3.5: The surface texture of the FTO glass is preserved during the deposition of thin coatings of TIA in butanol. (a) The surface of uncoated FTO glass (b) the surface after 1 coat of 0.05M TIA in butanol (c) after 2 coats and (d) after 4 coats.

Figure 3.6 illustrates EDX site mapping of the Ti-α x-ray line to show the distribution of titanium in the film. The amount of titanium grows linearly with the increased number of coatings, and shows no specific pattern, indicating uniform coverage. Note, that as a bulk technique, the EDX measures a depth of 1μm into the substrate, depending on the x-ray extinction coefficient of the substrate material, so the EDX signal mostly comes from the FTO glass below with the Ti signal being roughly proportional to its thickness for very small thicknesses.

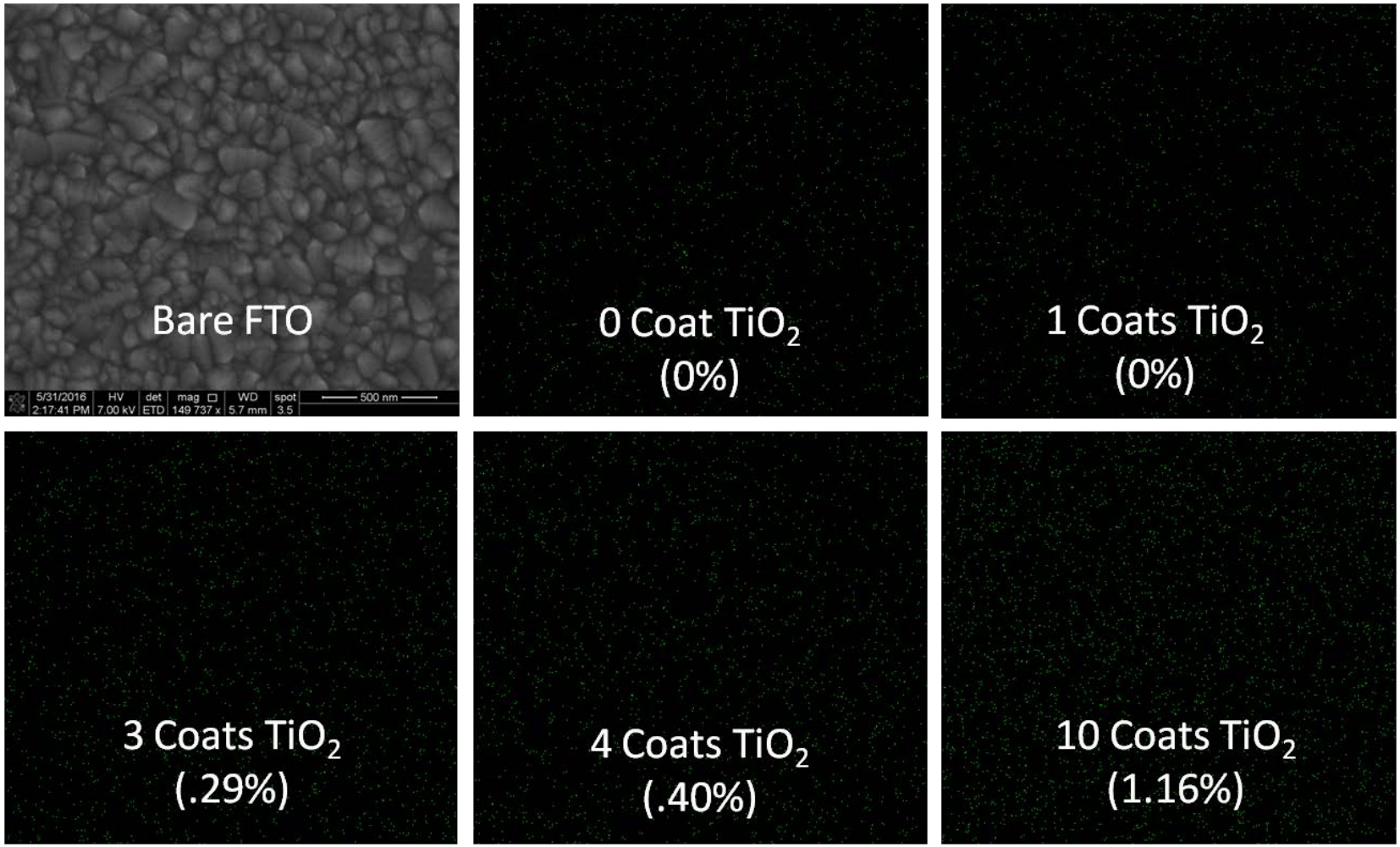

Figure 3.6: EDX map of Ti-α line for various thicknesses of TiO_2 film showing the uniformity of Ti deposition and the roughly linear relationship between the number of coats and approximate thickness of TiO_2.

Even so, some imperfections do remain due to the imperfections associated with spray pyrolysis. Figure 3.7 shows some of these imperfections on the surface due to uneven coatings that are difficult to completely avoid using spray pyrolysis. These imperfections can affect electrical properties and resistance, and may hide pinholes, and should be minimized as much as possible, but are likely present. Also, note the imperfections in the glass edge. These are likely related to poor fracture which is observed in most cases once TiO_2 is deposited and annealed on the surface.

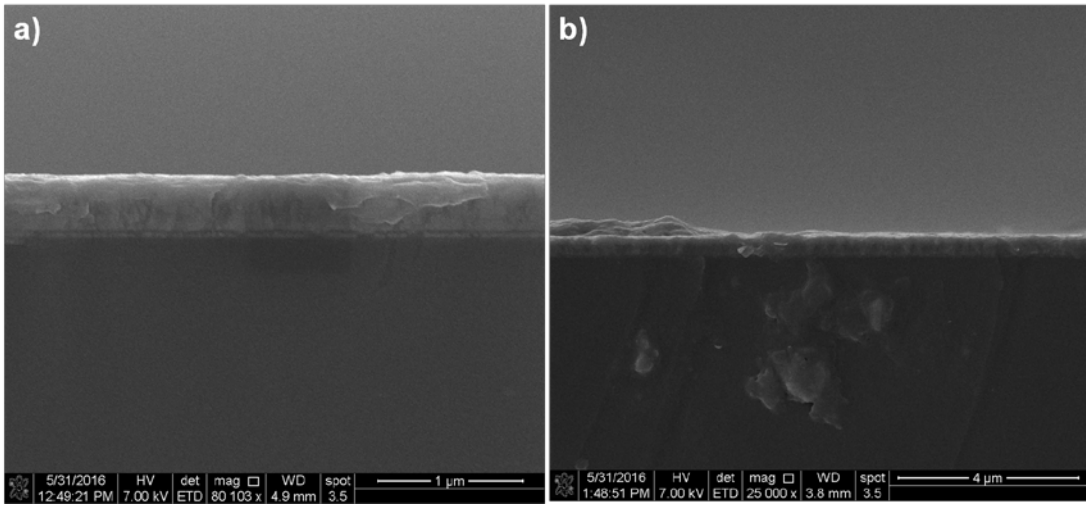

Figure 3.7: Cross sectional view of (a) FTO glass and (b) 4x8nm layers of TiO_2 from 0.05M TIA in butanol showing a large raised area of higher thickness in addition to a mostly smooth area.

The thickness and uniformity of the mesoporous TiO2 layers can be seen in Figure 3.8. This consists of 2 layers of Dyesol 18NR-T paste diluted in ethanol and deposited on soda lime glass to calibrate the thickness as compared to the profilometer and confirm uniformity. The films are of relatively uniform 1µm thickness in good agreement with the profilometer results, and they show few major surface defects.

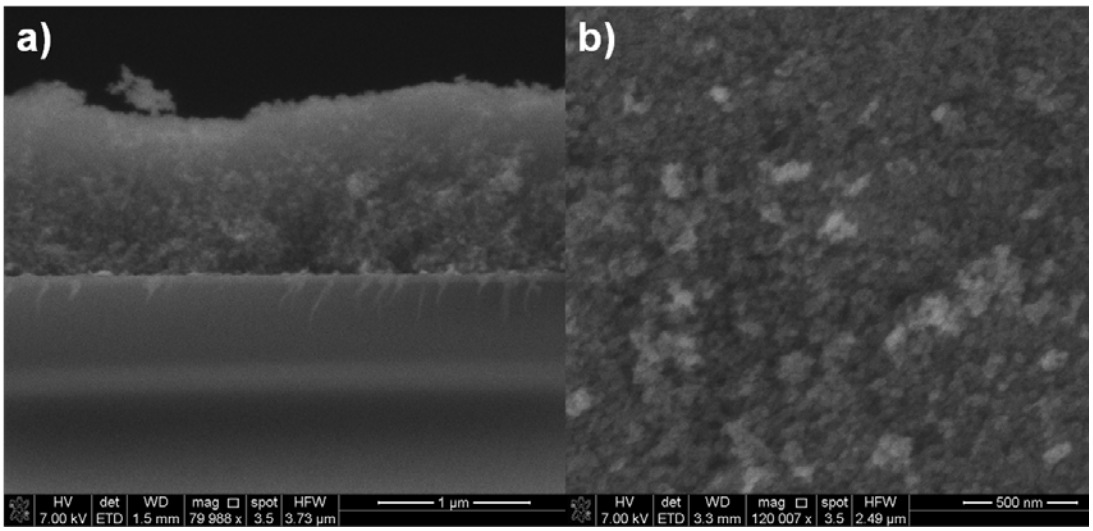

Figure 3.8: (a) Side view and (b) top view SEM images of the mesoporous TiO2 film on soda lime glass.

Confirmations of the effectiveness were performed by having our collaborators in Dr. Yanfa Yan's group at the University of Toledo deposit perovskite cells and measure their efficiencies on as-made TiO_2-FTO glass, as well as a variation that only includes 1 400-500nm coating of mesoporous TiO_2 film to be more optimized for traditional perovskite architecture. These cells yielded 13.2% efficient perovskite solar cells for the 1 micron mesoporous layer and 14.0% efficiency for the thinner layer with some hysteresis present. This indicates that while the films are functional, they could be improved for use with perovskite cells. Figure 3.9 shows the J-V characteristics under 1 sun illumination for these devices and the hysteresis that occurs, indicating some transport or trap limitations within the layers.

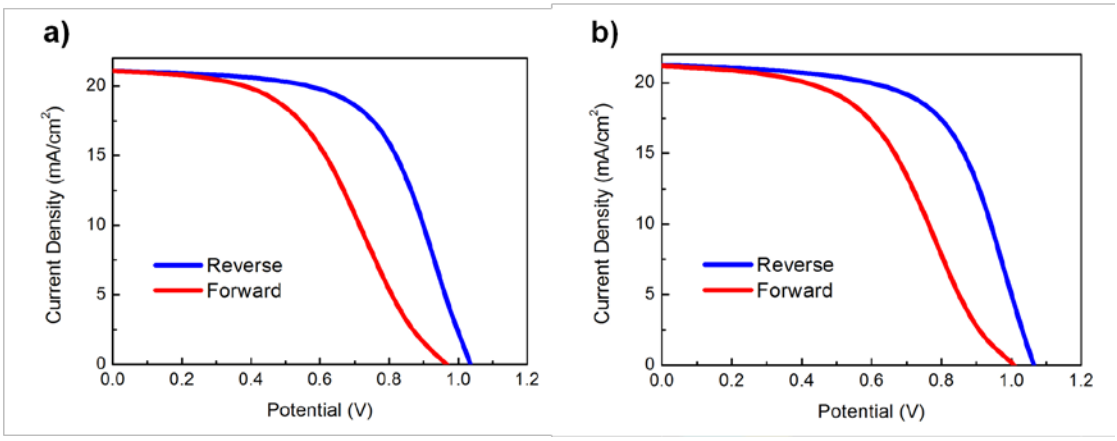

Figure 3.9: J-V performance of perovskite devices obtained from (a) films with a normal 800-100 micron mesoporous layer and (b) with a half-thickness 400-500nm mesoporous layer.

3.4 Conclusions and Future Work

FTO glass has been coated with both dense TiO_2 blocking layers and mesoporous TiO_2 scaffolds that can create reasonably efficient perovskite solar cells, indicating that the TiO_2 processing has been in general successful. Future work on these films should include the optimization of the spray-coater setup to minimize non-uniformities and imperfections in the dense layer. Further, as the dense layer's thickness could not be confirmed in SEM, due to the charging effects and resolution limitations for thin films, ideally another method should be used to corroborate the thickness of the as-deposited dense TiO_2 layer. This layer could then be further optimized for the desired device architecture.

CHAPTER 4. CZTS/CIGS SOLAR DEVICES WITH TIO_2 BUFFER LAYERS

4.1 Motivations and Background

Various derivatives of CIGS and CZTS have been hypothesized and created, including I_3-V-VI_4 materials, such as Cu_3SbS_4, Cu_3AsS_4,[36] and Cu_3PS_4,[34] or substitutions involving elements that are less likely to exhibit multiple oxidation states such as silver in $Ag_xCu_{1-x}In_yGa_{1-y}Se_2$,[31] or $Ag_xCu_{2-x}ZnSnS_4$,[30] or barium, as in $Cu_2BaSnSe_4$.[129] Some combinations have been reasonably successful, such as $CuZnInS_4$-CdS devices which showed initial performances of 6.7%;[28] however, many of these materials have struggled to form efficient devices due to the difficulty of forming large grains or the lack of a known compatible buffer material. The first goal of this research is to examine the potential of TiO_2 as a buffer material for thin film inorganic devices, in either a mesoporous bulk heterojunction form, or in a planar device structure.

The second goal is to create device structures for these conventional CIGS and CZTS materials that are more compatible with the manufacturing of bifacial solar cells. Bifacial solar cells are able to absorb light from both sides, absorbing any reflected light on the surface behind. Since solar panels are spaced to absorb shading, the reflection of the light from behind can be harvested in a bifacial cell improving efficiency by as much as 50% depending on the albedo of the ground behind the cells.[130] Bifacial silicon solar cells have been developed with similar efficiencies on either face, with efficiencies

comparable to commercial solar cells.[130] Bifacial solar cells based on transparent electrodes for dye-sensitized cells have also been reported.[131] However, it has been difficult to create bifacial CZTS and CIGS cells due to the continuous metal back contact, often Mo, which reflects any incident photons from behind. These devices use a substrate structure with the light coming from above without passing through the glass, while some materials, such as CdTe-CdS are more traditionally manufactured in the superstrate structure where the light passes through the glass support before reaching the cell, though they can be manufactured both ways.[132] An interesting alternative to conducting oxides has been sheets of silver nanowires that create a transparent and conductive film.[133] If these nanowires could be used to replace a solid metal contact on the back of thin-film devices as well, a bifacial solar cell could be made. This would be easiest in a superstrate configuration where the silver nanowires do not have to undergo repeated high-temperature annealing, potentially altering shape or reacting with the material or Se atmospheres. These nanowires are known to condense into droplets of silver with annealing of over 200ºC for 40mim, and are unlikely to withstand the harsh environment used for grain growth of CZTS and CIGS materials.[133]

The substitution of elements in a crystal lattice can have a dramatic impact on the band structure of a semiconductor. This is commonly exploited to optimize the band gap of thin film materials, with CIGS being one of the most notable examples, with the In:Ga ratio being tuned both to optimize the band gap and alter the band structure within the device. The addition of gallium raises the conduction band edge relative to CIS, as shown in Figure 4.1.

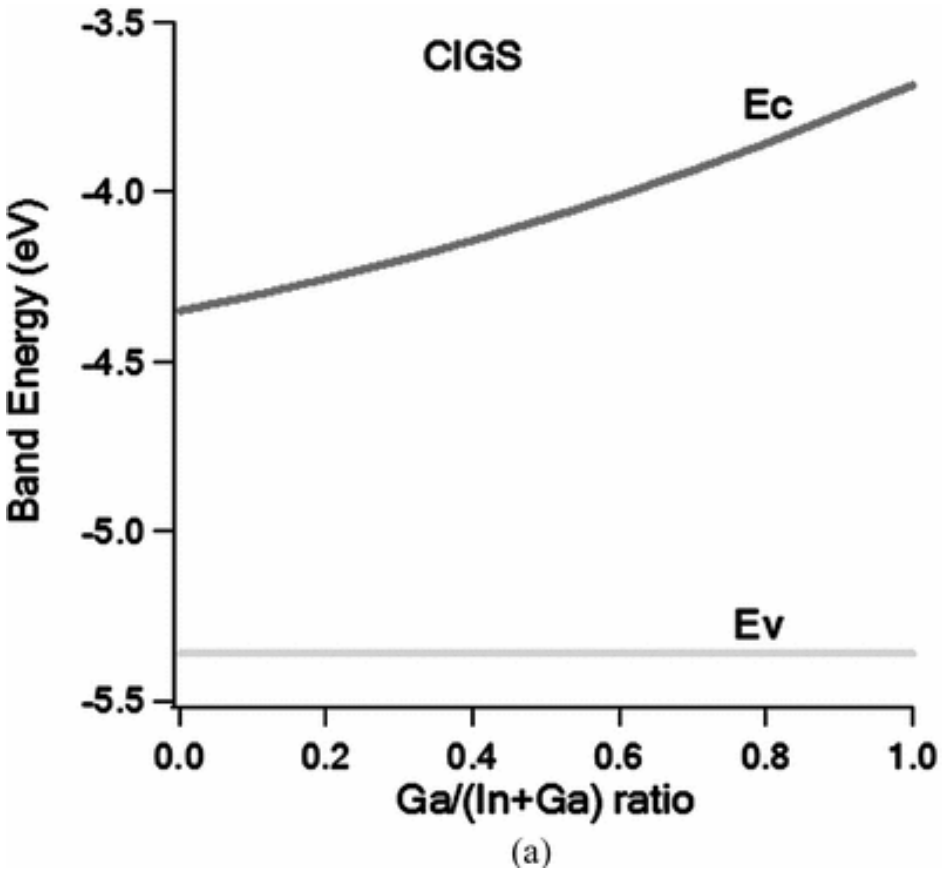

Figure 4.1: The effect of Ga-In Alloying on the band structure of CIGS. *Copyright IEEE 2014. Reprinted, with permission, from Sharbati, Samaneh and James Sites Impact of the Band Offset for n-Zn(O,S)/p-Cu(In,Ga)Se_2 Solar Cells, IEEE Journal of Photovoltaics vol. 4 iss. 2 January 2014.*[147]

Traditionally, the conduction band position is predominantly affected by cation substitution while the anion has a dominant effect on the valence band position, though many exceptions exist to this pattern.[134] Larger ions tend to decrease band gap, while smaller atoms tend to increase it. Figure 4.2 shows band positions for a variety of materials measured by photoemission spectroscopy. While band gap is easily measured, depending on measurement an manufacturing conditions, relative band alignment can vary with surface defects and alignment.[134]

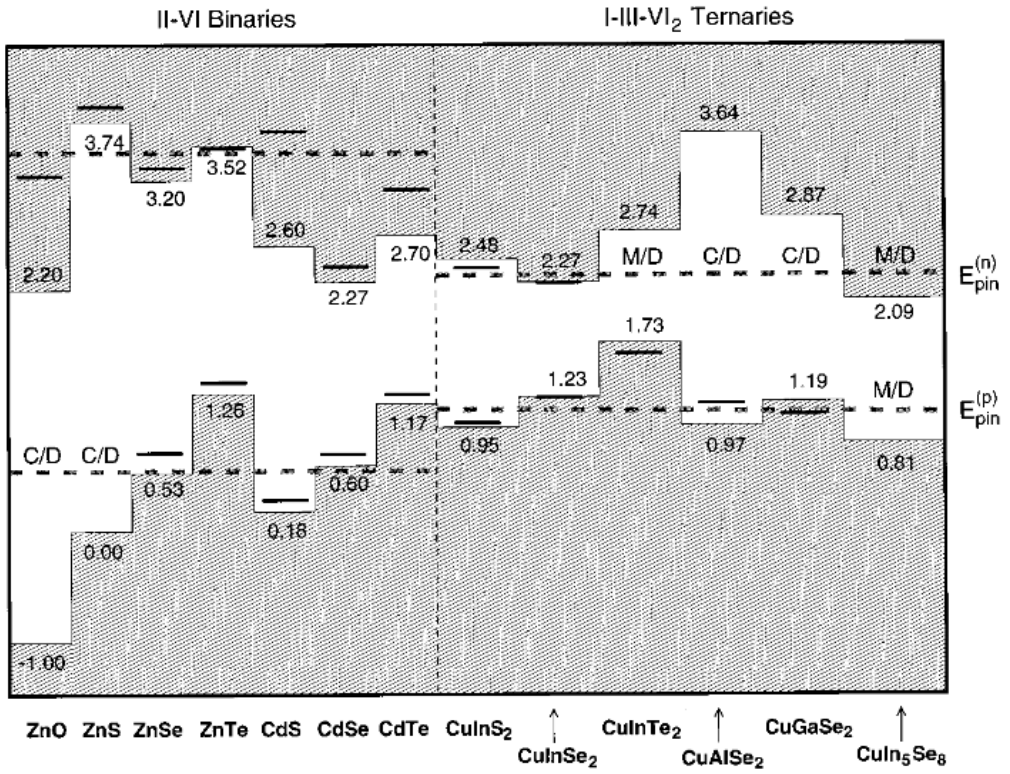

Figure 4.2 Band alignment of common thin film materials. *Reprinted from Zhang S. B, Su-Huai Wei and Alex Zunger. Journal of Applied Physics, Volume 83, Issue 6, 1998. with the permission of AIP Publishing.*

As previously mentioned, the band alignment of the conduction edge is very important for solar cells with a p-type absorber layer. Too large of a barrier limits the amount of current that can flow, while a drop results in lost voltage at the junction. This is one of the reasons CIGS-CdS cells tend to be most effective with Ga:In ratios around 30% where the conduction band of CIGSe aligns closest with that of CdS. Anatase TiO_2 is expected to have a lower conduction band than CdS at about 4.5eV below vacuum level compared to 4.3eV.[135] This aligns well with the relatively lower conduction band of CIS.

As previously mentioned CIGS cells with a TiO_2 blocking layer have been made; however, they utilize atomic layer deposition. Scanlon et al. also specifically identify

indium segregation near the junction and model the device as a CIS-TiO_2 junction to best describe their results, indicating that CIGS and CIS may be good candidate materials for pairing with TiO_2.[41]

Other effective solar cell combinations include the use of a thin blocking layer of TiO_2 for InP thin films,[135] as well as a mesoporous layer for dye-sensitized cells utilizing CZTS as a sensitizing agent with a liquid electrolyte.[136,137] These show that there is a wide potential for various inorganic materials to be paired with TiO_2 films as a replacement for CdS.

The sintering of particles or films to form large grains is expected to depend on the presence of liquid selenium wetting the surface of the particles.[138] Liquid phase sintering is a well-known processes for the sintering and coarsening of metal and ceramic powders for materials processing. The addition of a flux material that melts at a lower temperature can act as an agent for sintering and grain growth as the solids can dissolve in small quantities in the liquid flux and diffuse away from high energy, highly curved smaller particles and redeposit on larger, lower energy particle surfaces resulting in rapid grain growth.[139] For CZTS and CIGS, condensed selenium is expected to play that role, but for materials that are not phase stable when heated in a selenium environment, or that do not interact with selenium as favorably to form large grains, it may be advantageous to be able to use a bulk heterojunction structure to bring the n-type and p-type materials into close contact to get a more efficient device. A bulk heterojunction is formed when two dissimilar semiconductors are locally phase separated, but are intermixed on the scale of a few tens of nanometers, creating contact over a large surface area. They are most well

known and commonly studied in the case of polymer mixtures and block-copolymers that phase segregate on a small scale.[140,141]

4.2 Early Experiments with CZTS on TiO_2

The earliest experiments performed utilized doctor-blading for the deposition of mesoporous TiO_2 and the use of amine-thiol CZTS molecular precursors also deposited by doctor-blading to make a first set of devices. The TiO_2 deposition was carried out as explained in chapter 3 with some notable exceptions. The spray-pyrolysis was carried out with 16 coats of 0.2M TIA in ethanol, resulting in TiO_2 films 150-200nm in thickness. The deposition of mesoporous TiO_2 was carried out via doctor-blading 3 coats of 30μL Dysesol 18NR-T paste in ethanol with a 2:7 mass ratio. Unless otherwise noted, all chemicals were obtained from Sigma Aldrich and used as provided.

The CZTS cation precursors consist of solutions of 0.153M copper (I) chloride (CuCl), 0.105M zinc chloride ($ZnCl_2$) and .1M tin (II) chloride ($SnCl_2$) dissolved in a 1:1 volume ratio mixture of hexylamine (HA) and propanethiol (PT). Chalcogenide precursors consisted of 2M sulfur solutions in a similar 1:1 HA:PT solvent. These solutions are based off of and similar to those presented by Zhang et al.[70] An equimolar amount of sulfur in HA:PT solution was combined with the cation precursors once they had all dissolved. An adjustable pipette with polyproylene tips was used to deposit 30μL of this solution on the prepared TiO_2 substrate. A 1/4" diameter borosilicate glass rod resting on similar pieces of glass covered by one layer of Scotch Magic Tape was passed over the top of the film to spread and smooth the solution. Between CZTS coats, the

sample was annealed for 5 minutes at 300°C. After finishing, the sample was annealed for 30 minutes at 500°C.

Spiro OMeTAD soltuions in chlorobenzene were prepared for the deposition of a hole-transport layer. These consisted of 100mg of spiro OMeTAD dissolved in 0.444mL of chlorobenzene. A stock solution of bis(trifluoromethyl)sulfonimide lithium salt (TFS-Li) in acetonitrile was prepared with a concentration of 170mg TFS-Li per 1mL of acetonitrile. Then 8.33μL of the TFS-Li solution and 3.85μL of tert-butylpyridine were added to dope the spiro OMeTAD solution. A similar doctor-blading procedure deposited 30μL of this solution on the top of each device as a hole-transport material to block contact between the TiO_2 and the top metal contact. The device was completed by the deposition of a 250nm gold (Au) layer using an MBraun glovebox resistive thermal evaporator with tungsten evaporation boats. The thermal evaporator operated at a pressure below 10^{-5} torr, with a rate of 0.01 Å/s for the first 1nm, a rate of 0.1 Å/s for the next 9nm, and a rate of 1 Å/s for the remainder of the duration.

These devices were completed by scraping and mechanically cleaning a side of the 1"x1" substrate and depositing indium contacts on the ITO conductive coating. Four-point probe current-voltage (IV) measurements were performed using a calibrated Oriel Solar Simulator at 1 sun and a Keithley benchtop voltage and current source. These IV measurements showed no diode behavior, and followed an almost perfectly straight line, indicating that the devices were shorted out or otherwise faulty and functioned merely as resistors. A cross-sectional SEM shown in Figure 4.3 indicates that uniform films were obtained, and that the absorber material penetrated into the mesoporous structure, however no visible spiro OMeTAD layer or Au metallic layer appears in these SEM

cross-sections indicating they may have also penetrated the lattice. EDX line-scans of the cross section confirm relatively uniform distributions of Cu, Zn, Sn and S in these films, indicating a relatively uniform concentration of deposited CZTS and relatively uniform composition. Figure 4.4 shows the results of this line scan for the Cu, Zn, Sn and S EDX spectrum. While these preliminary devices did not produce measurable efficiencies, they do indicate that the infiltration of amine-thiol precursors into mesoporous TiO_2 is possible.

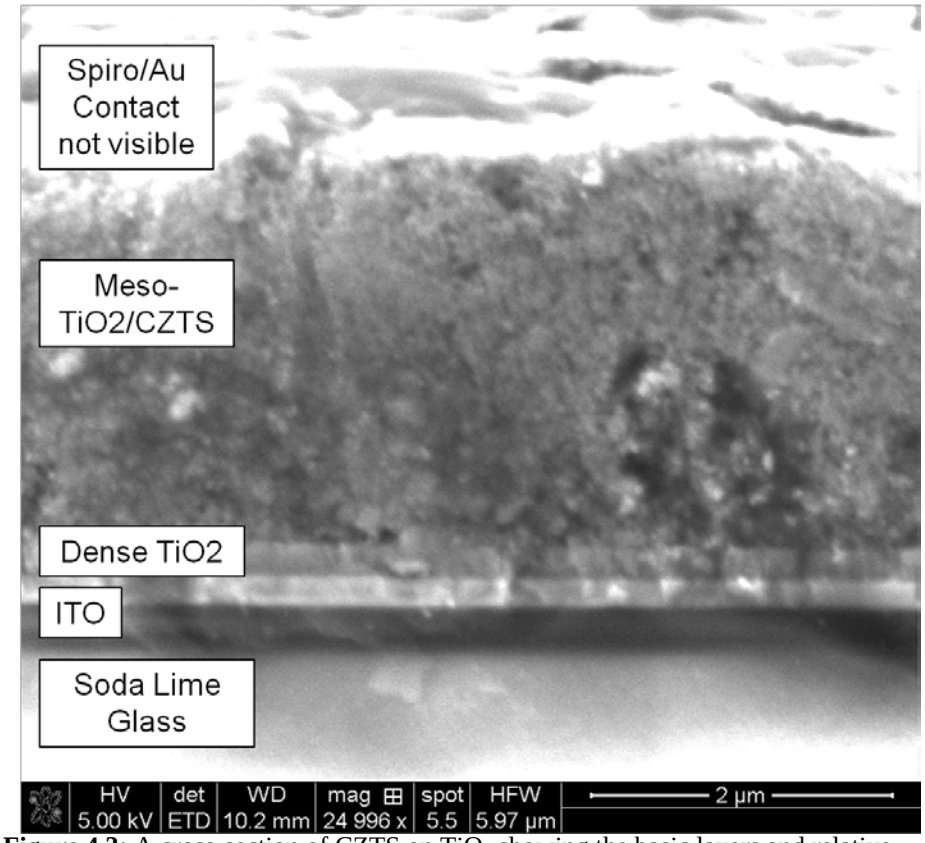

Figure 4.3: A cross-section of CZTS on TiO_2 showing the basic layers and relative uniformity of the layers for the device.

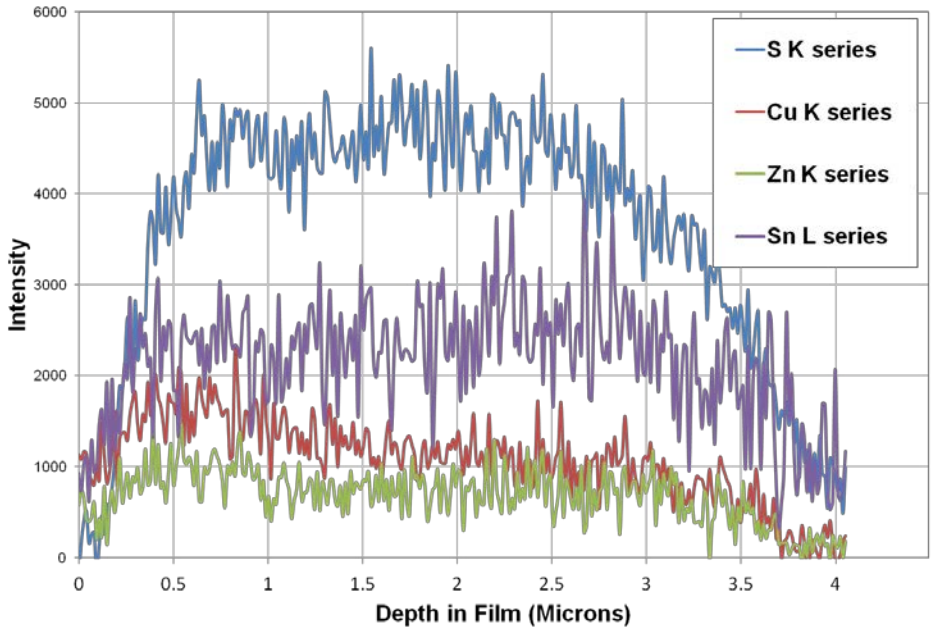

Figure 4.4: EDX linescan showing the uniform composition of CZTS through the film.

4.3 CIGS on Mesoporous TiO_2

Later experiments replaced the CZTS with CIGS, as it is known to provide better semiconductor behavior and yield more efficient devices. Initial substrates were made identically to the CZTS devices previously described. Better substrates were made using the methods described in chapter 3 of this thesis. The CIGS molecular precursors were slightly more concentrated versions of those used by Zhao et al.[54] Individual cation precursor solutions were made by dissolving 0.4M of copper (I) selenide (Cu_2Se), indium acetylacetonate ($InAcAc_3$) and gallium acetylacetonate ($GaAcAc_3$) separately in a 10:1 volumetric ratio mixture HA and 0.2mL ethanedithiol (EDT). A 1.0M selenium solution was prepared by dissolving 2.2mmol of selenium in 2.2mL of an identical 10:1 HA:EDT mixture. These solutions were allowed to fully dissolve overnight for at least 12h before

mixing to ensure complete dissolution. A CIGS precursor was made by combining 1.44mL of Cu_2Se solution, 2.20mL of $InAcAc_3$ solution and 0.94mL of $GaAcAc_3$ solution, and then adding 1.89mL of the Se solution, creating a 30:70 Ga:In ratio and a slightly copper deficient 92:100 Cu:(In+Ga) ratio in the mixture and a 25% excess of selenium. Layers were deposited using 150μL of solution per layer on a spin-coater in a nitrogen-atmosphere glovebox operating at 800 RPM for 30s. Ten or twenty layers were applied, with a 5 min 300°C anneal between layers and a 30min anneal at 500°C following the final layer.

The spiro OMeTAD layer is also deposited differently, as reported by NREL in Zhao et al.[124] 80mg of spiro OMeTAD were dissolved in 1mL of chlorobenzene. Following the dissolution of the spiro, 30μL of TFS-Li solution (500mg in 1mL acetonitrile) and 30μL of tert-butylpyridine are added to the solution. A single layer is spin-coated on the film using 80μL of solution at 4000RPM for 35s. A proper coating should look glossy with no build-up around the edges. The deposition of a 250nm Au contact is achieved in a manner identical to the preliminary CZTS devices.

The substrates were scribed in a grid of 12 or 16 individual devices with a 3mm x 3mm active area using mechanical scribing, spaced 2mm apart, for an approximate device area of $0.1cm^2$. A measurement apparatus was developed to facilitate the electrical contact with the back side of the devices using a 1/4" steel plate with an aperture drilled in it to allow light to pass through. Dual probe tips mounted on magnetic micromanipulators allow electrical contact to the back of the device, which is clipped to the plate. The entire mechanism can be turned over to illuminate the active side of the device. This setup is illustrated in Figure 4.5.

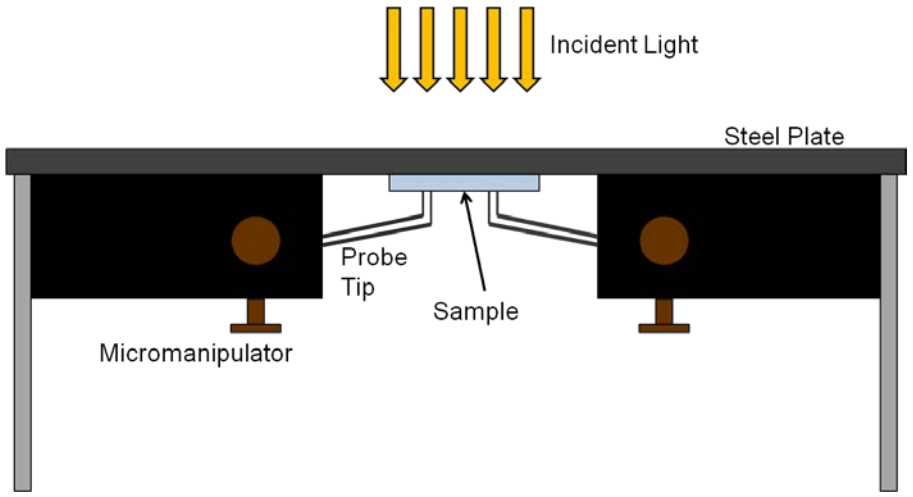

Figure 4.5: Setup for measuring superstrate devices under AM1.5 illumination.

The devices made with the same earlier method of making a TiO_2 layer show a similar cross-section to the earlier CZTS-based devices, as shown in Figure 4.6. These devices also show, as seen in Figure 4.7, a uniform distribution of CIGS within the layers of the device. EDX also shows that the top ~200nm of the CIGS film contains significant amounts of AU, though it is difficult to see in the SEM cross-section.

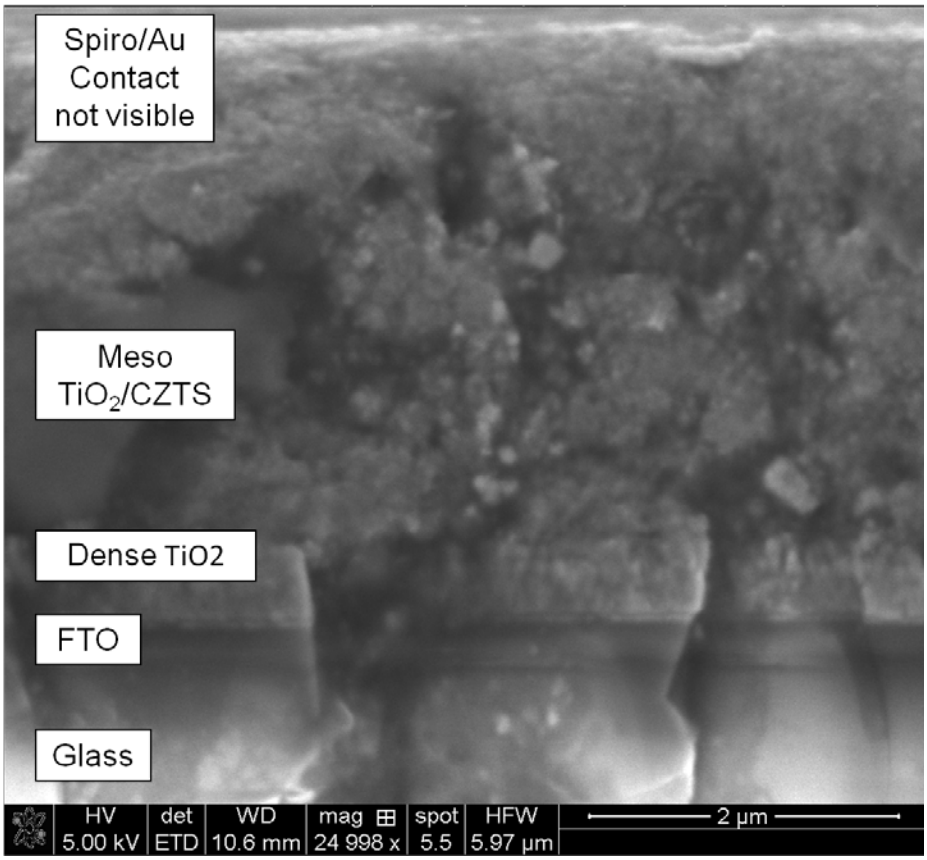

Figure 4.6: SEM cross section of a CIGS on a doctor-bladed mesoporous TiO_2 superstrate.

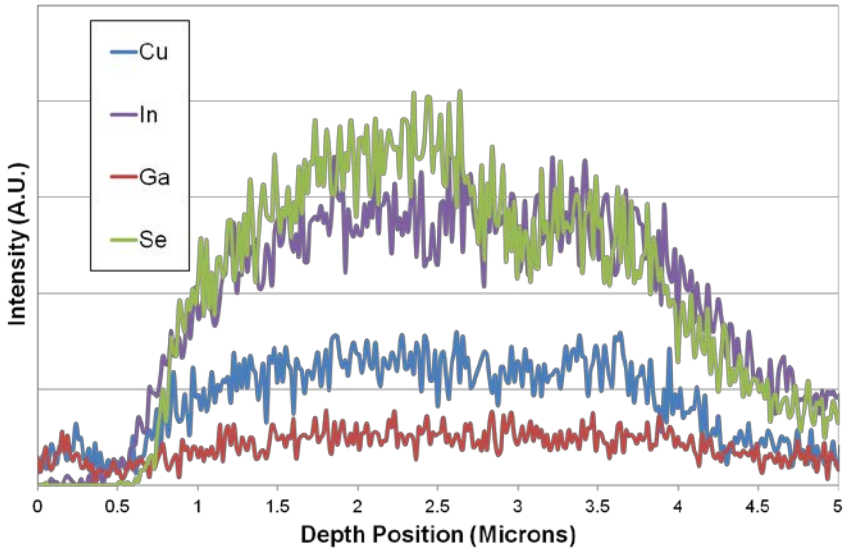

Figure 4.7: EDX line scan intensity showing roughly equal distribution of CIGS through film

Devices made with the thinner dense TiO_2 layer (~30nm) and a mesoporous layer fabricated via spin-coating have a slightly smoother cross-sectional appearance as seen in Figure 4.8.

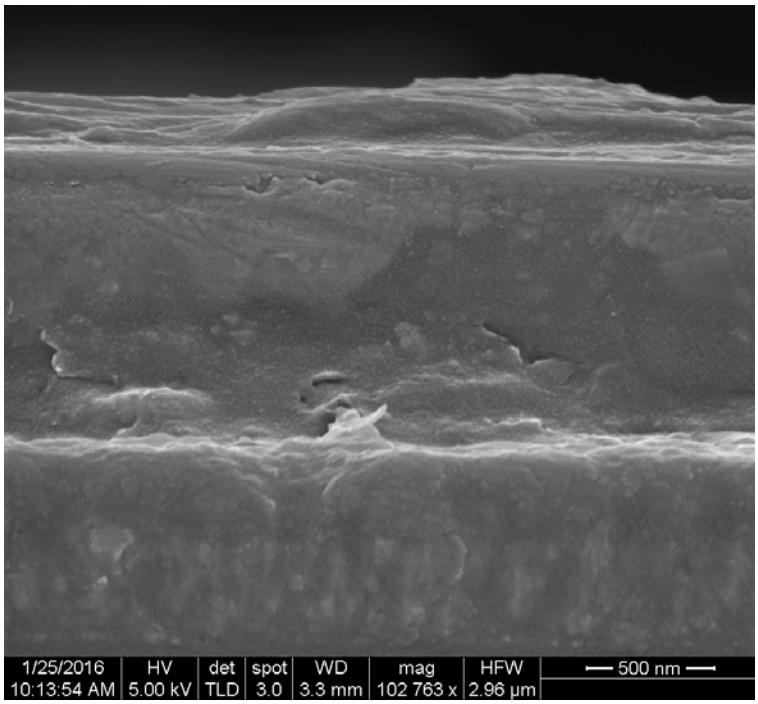

Figure 4.8: Cross section of CIGS in mesoporous TiO2 as deposited in Chapter 3.

An attempt was made at annealing these densely coated devices in a selenium environment after 10 layers of CIGS were deposited, however, the expansion during selenization, and the capillary forces from any condensed liquid selenium disrupted the structure of the mesoporous CIGS device and led to a highly uneven film. A 1"x1" sample as coated was annealed in a tube furnace under argon at 500°C for 20min in a 3"x1" graphite box with 260mg of selenium. The TiO_2 was observed to remain in an anatase phase via post-selenization XRD measurements, and grain growth was observed within the film; however, as a SEM cross section shows in Figure 4.9 the film itself was completely deformed in this process.

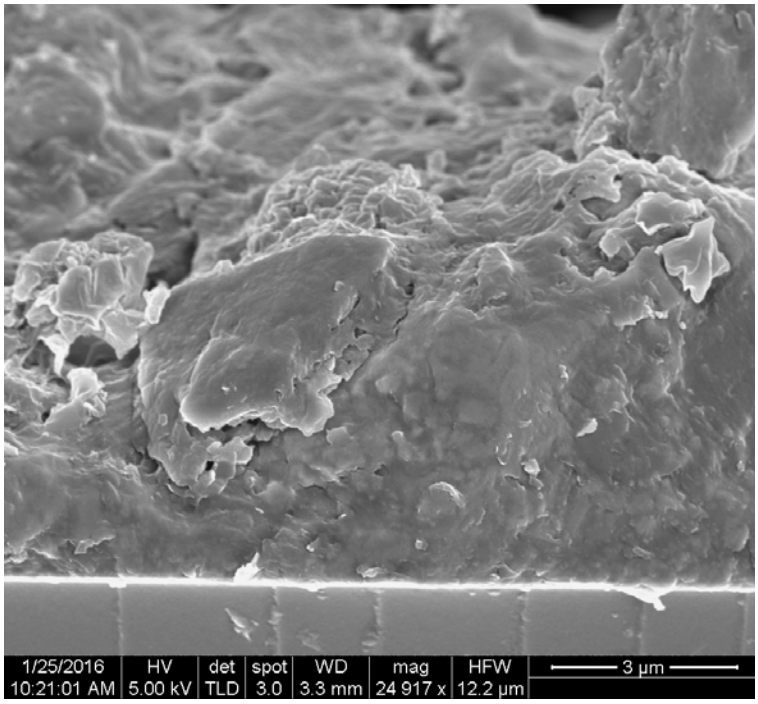

Figure 4.9: Cross section of CIGS deposited in spin-coated mesoporous TiO_2 and annealed in a selenium-rich environment.

That the anatase form is stable even after annealing in a selenium environment is shown by annealing bare dense films of anatase TiO_2 on FTO glass in a selenium rich environment. After annealing, no changes are visible for the films in XRD and Raman spectroscopy, or visibly. The XRD peaks clearly show no difference in the films, though they are dominated by the SnO_2 casserite phase from the FTO. However, due to the wide band-gap of TiO_2 and the long wavelength of our Raman, no signal is evident in the Raman structure, and tin or titanium selenides are dark semiconductors or semimetals and would clearly show an alteration in this spectrum as well as a visible darkening.

The current-voltage (J-V) relationship was measured both under illumination and without illumination. A typical cell with the thicker dense TiO_2 and doctor-bladed mesoporous TiO_2 showed an efficiency of 0.00016%, a V_{OC} of 0.02V, a J_{SC} of 25µA/cm2, and a fill factor of 0.26. This is a highly non-ideal cell, showing significant shunting and

a series resistance of approximates 300Ω/cm^2. Further, the shunting is non-linear and higher under illumination. The parasitic resistances reduce device efficiency, though the diode behavior is clear. The shunt current can be fit to a three-parameter model as shown in Chavali et al. by fitting the data to the following model:

$$J_{sh} = G_{Sh}V + J_{0Sh}V^n$$

where G_{Sh} is the ohmic shunt and J_{0Sh} and n are constants relating to space-charge limitations and shunting, and $1 < n < 2$.[142] Using this model, we can subtract a shunt current from the data, and see more clearly the diode behavior. The increased shunting during illumination is caused by the higher carrier concentrations under illumination, suggesting that the TiO_2 films may suffer from low carrier concentration or that significant recombination is occurring in the space-charge region. The high series resistance is indicative of the high resistance through the TiO_2 and along the conducting oxide. Figure 4.10 shows the JV behavior with and without correcting for shunt current.

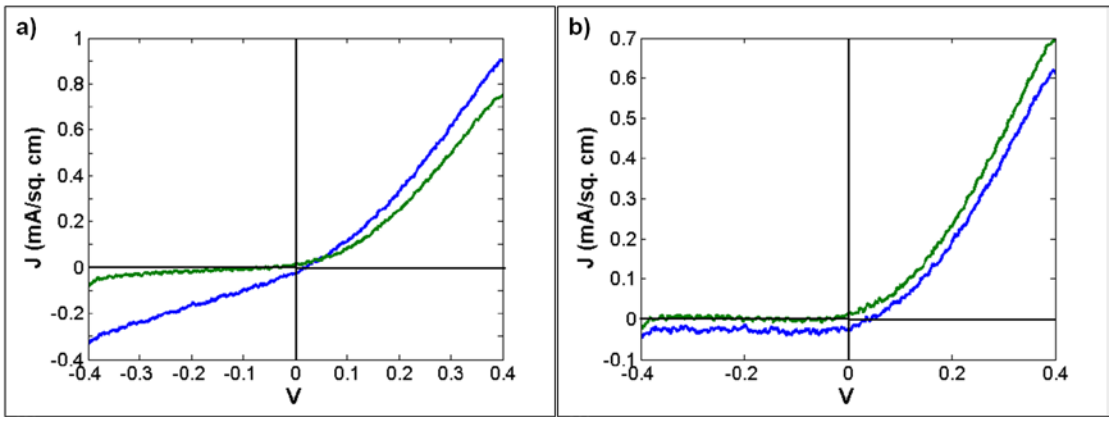

Figure 4.10: J-V behavior of CIGS on early mesoporous TiO_2 exhibiting significant shunting (a) before subtracting shunt current and (b) after subtracting shunt current.

For the device above, the shunt current parameters are calculated as J_{0Sh}=8.5x10^{-4} mA/cm^2 in the dark and 7.3x10^{-4} mA/cm^2 under illumination, G_{Sh}= -7 x10^{-4}Ω/cm^2 and 0, for light and dark respectively and n=1.084 or 1.024 for light or dark respectively. This

indicates somewhat linear shunt, but that the space-charge/non-ideal effects dominate the behavior of the devices, as the traditional shunt current, G_{Sh} is low compared to the non-linear behavior.

Improving the fabrication of the TiO_2 film by spin-coating the mesoporous layer and reducing the thickness of the dense layer to ~30nm by using 4 coats of 0.05M TIA in butanol significantly increases device performance, though many of the same issues are present. By comparison, these devices still show significant cross-over and much higher shunt current under illumination than in the dark; however, much of the series resistance is decreased, allowing significantly more current through the device, indicating that the TiO_2 layer is limiting the series resistance behavior. While the efficiencies are still quite low, they show significantly improved behavior when compared to the less optimized devices. The efficiency increases ~20x to 0.0037%, V_{OC} to .096 V, the J_{SC} increases to 120μA/cm^2, and the fill factor increases to .317. The series resistance decreases drastically to 19 Ω/cm^2. This reduction in series resistance indicates that the thinner, improved TiO_2 is the likely cause of the improved behavior. The J-V behavior is shown in Figure 4.11.

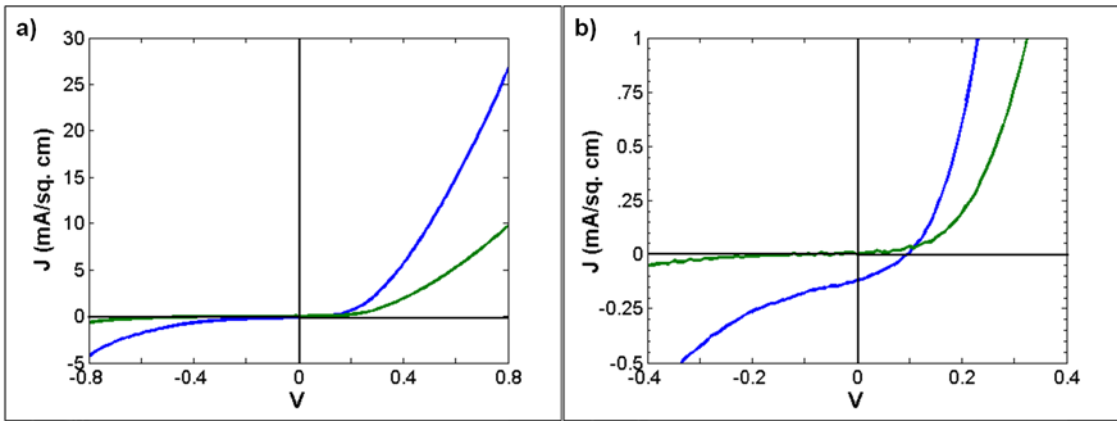

Figure 4.11: The J-V characteristics of the improved CIGS devices on mesoporous TiO_2 over a (a) broader voltage range and (b) a narrower voltage range to show the photovoltaic performance.

However, the major limitation in all of these devices is the short circuit current density. Ideally, this value should be approximately 30mA/cm^2 for a CIGS device having a band gap of about 1.1 eV. The low current density is likely due to the poor grain size grown from the amine-thiol molecular precursors. The electron-hole pairs formed in the CIGS may recombine at grain boundaries and surface defects before they are able to be completely separated by the electric field. Further, the electric field in a bulk heterojunction may exhibit significant local fluctuations on the scale of the pore size, which is a few nanometers in this case, so a larger pore size may be beneficial.

The lack of absorption in the CIGS is supported by the J-V data obtained by creating a device without the CIGS absorber layer, relying only on the contact between the TiO_2 and the spiro OMeTAD. Such a device was created utilizing the same methodology on the optimized TiO_2 substrate, and performed better than either of the prior device types. The device showed an efficiency of 0.052%, with a substantially improved V_{OC} of .785V, a similar J_{SC} of 119 μA/cm^2, and a fill factor of .55. The series resistance, however is higher, due to the low conductivity of the spiro OMeTAD, at

approximately 400 Ω/cm^2. The device yields a similar current density while remaining optically transparent, indicating the CIGS devices have low very quantum yields in the visible spectrum. Figure 4.12 shows the J-V behavior of these devices. Charges may potentially remain trapped in the mesoporous structure due to local fluctuations. Figure 4.13 illustrates how a charge profile within a small pore could result in charge trapping due to the local electrical field. Grain boundaries could further contribute to this effect depending on their location and energy states.

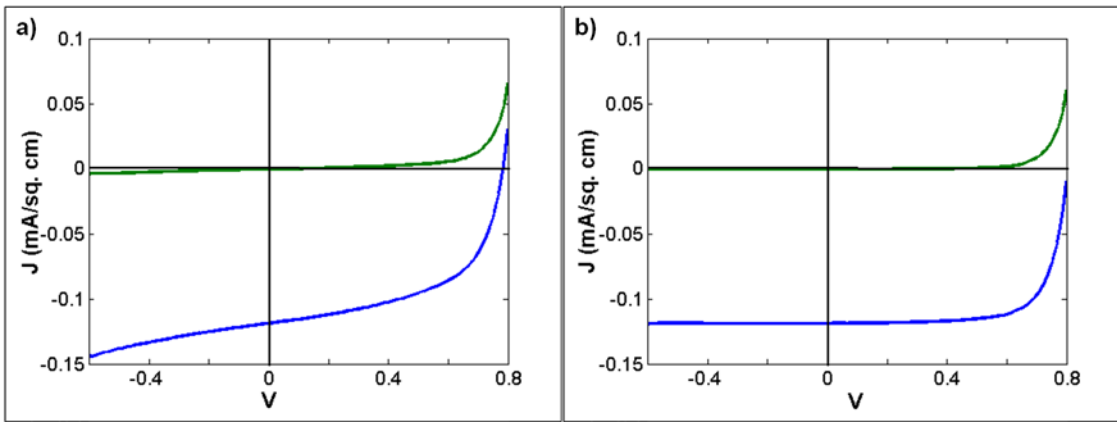

Figure 4.12: Current-voltage response of a spiro OMeTAD-TiO_2 device (a) before and (b) after subtracting shunt resistance.

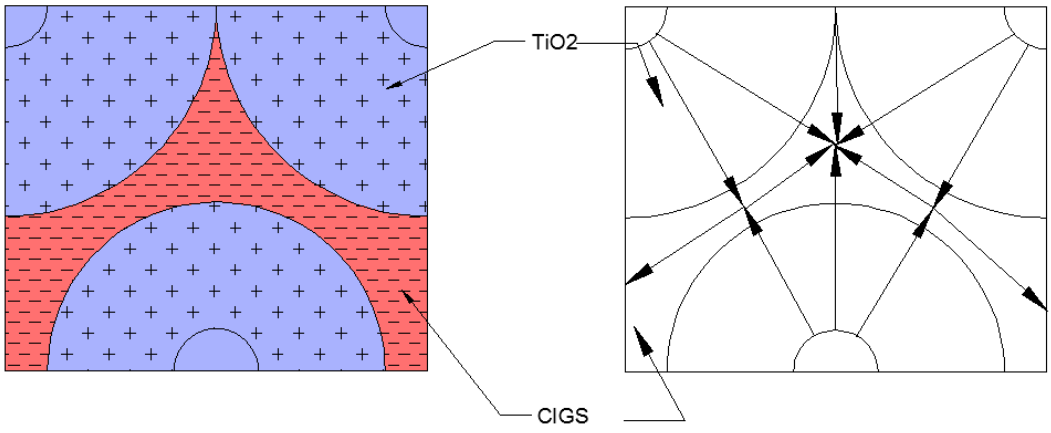

Figure 4.13: An Illustration of how local contributions to a an electrical field caused by the space-charge region in a bulk heterojunction can contribute to cause a trap state when the pore dimensions are uneven. The arrows represent the direction of the electrical field, but not the magnitude.

4.4 Evaporation of CIGS precursors on Mesoporous TiO_2

Larger CIGS grains are necessary to achieve better device efficiency in a mesoporous CIGS-TiO_2 cell. In an attempt to grow larger grains within the pores, CIS precursors were prepared in light amine-thiol solvents and evaporated on top of a 1"x1" mesoporous TiO_2 film prepared as described in Chapter 3. These films were placed in the bottom of a 45mm borosilicate cylindrical glass reactor vessel with a PTFE-coated rubber O-ring seal. A lid with 4 ports was attached, of which 2 would be used: the vertical port connected to a Schlenk line in a fume hood, and a side port covered with a butyl rubber septum for the injection of the precursor materials. Figure 4.14 shows a schematic of the reactor setup. It is absolutely essential for this procedure that the liquid nitrogen trap on the Schlenk line be completely filled with liquid nitrogen to condense the vapors that will be created before they can reach the pump oil and that the pump be safely vented in the case any of the solvents do reach the pump.

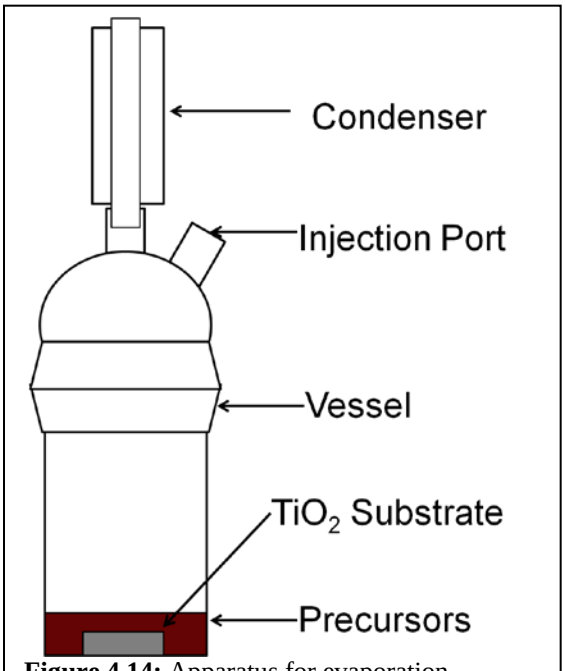

Figure 4.14: Apparatus for evaporation.

CIS precursors were prepared in a nitrogen-atmosphere glovebox by dissolving Se in a 10:1 volumetric ratio mixture of either butylamine and ethanethiol or in hexylamine and propanethiol to create a Se solution with a concentration of 0.021M. In 17mL of the same solvent, copper (II) acetylacetonate and indium acetylacetonate were dissolved to create a solution with a 0.003M concentration of both copper and indium precursors. These were allowed to dissolve for at least 2 hours before adding 5mL of the selenium solution to the copper/indium solution. The reaction setup was evacuated 3 times under vacuum and refilled with argon to remove any residual oxygen. Then, under vacuum, with a closed stopcock between the flask and the Schlenk line, 20mL of the precursors were added using a purged disposable syringe and needle. Immediately some of the solution evaporated to reach saturation, however the remaining solution settled in the bottom of the flask. A heating mantle with an Omega PID controlled was used to maintain the flask at 30°C to provide the heat of vaporization for the precursors, and the flask was opened to vacuum on the schlenk line for 20 minutes to allow the solvent to evaporate. After 20min, the mantle temperature set point was raised to 100°C, and the residual material was heated to 100°C to remove any excess solvent still present. Following this, the sample was removed and placed on a 500°C hot plate in a nitrogen glovebox for 15 minutes to anneal the precursors and remove any excess solvents. Upon removing the liquid nitrogen from the schlenk line, the solvent trap was immediately cleaned to remove the evaporated solvent before it could melt to minimize the release of thiols to the lab atmosphere.

After annealing, the samples had a slight smoky caramel color but were mostly transparent. Excess CIS deposited on the surface that was not in the pores fell off the

surface as a fine powder but did not visibly adhere, though the material within the pores remained. For the HA:PT films a few dark spots were observed well-adhered to the surface.

A part of each of these samples was separated to be individually characterized, while another section of each was annealed at 500°C for 40min in a 3"x1" graphite box containing 360mg of Se pellets under and argon atmosphere. These samples were then examined under a SEM microscope and via EDX to determine the morphology and composition of these films. In each case, a relatively uniform distribution of CIS precursors was observed in the film before selenization, but after selenization, larger isolated particles of CIS were observed irregularly interspersed in a matrix of mesoporous TiO_2 that showed low to no concentrations of CIS material, indicating that the CIS had coalesced into large grains and left the TiO_2 structure. This could be understood as the CIS grains growing through liquid-phase sintering and repelling the TiO_2 particles due to an unfavorable surface energy between the Se or CIS crystals and the TiO_2, indicating that there are potential wetting issues during grain growth with CIS or Se and the TiO_2 substrate.

Where the dark mark was observed for the HA:PT film, SEM revealed an over layer of CIS with a mesoporous Cu deficient TiO_2 under layer. Figure 4.15 shows the SEM images of these films.

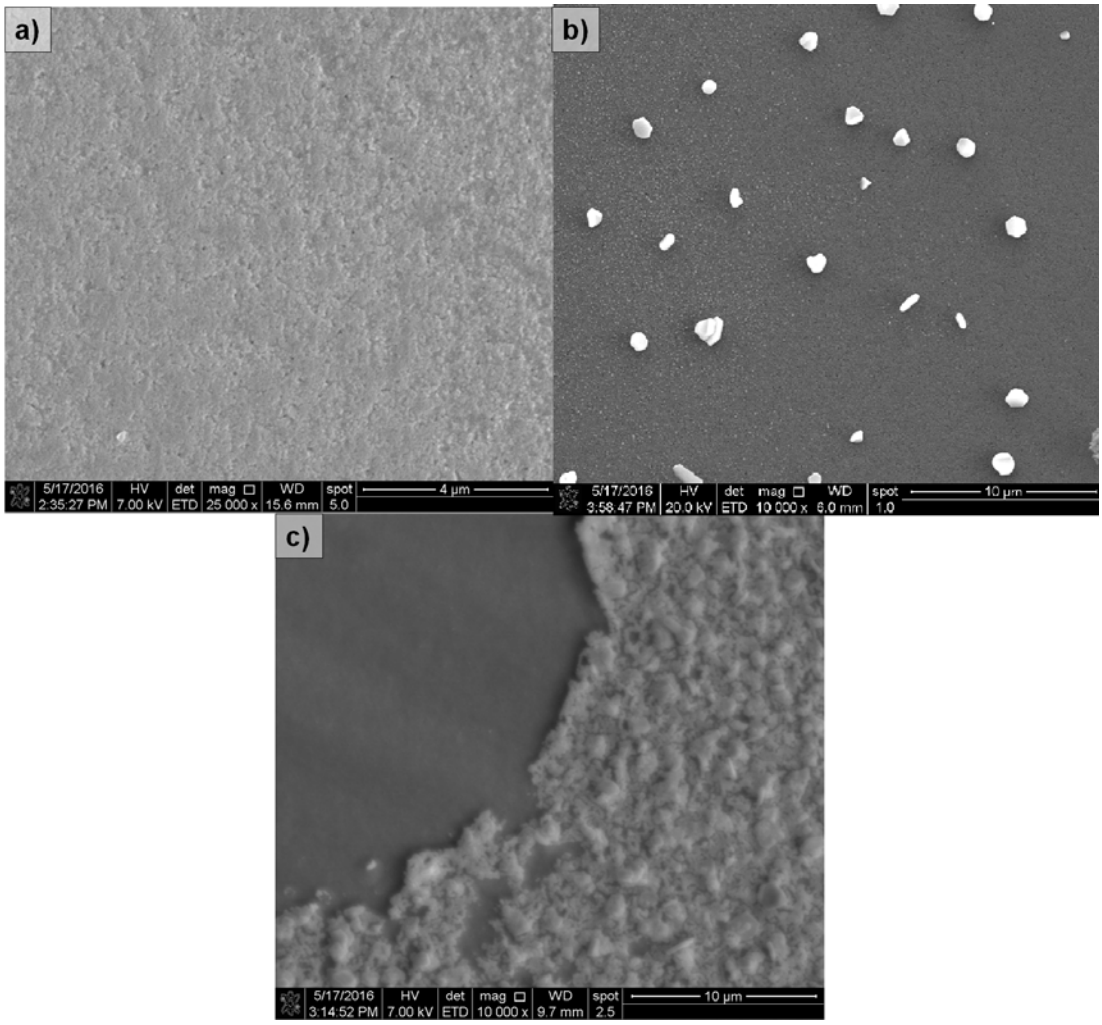

Figure 4.15: SEM images of the surface of evaporated CIS films on TiO_2: (a) Butylamine and ethanethiol film, as desposited before evaporation. (b) The same butylamine-ethanethiol film after selenization showing 2 micron-sized CIS grains, and (c) the CIS rich crust over TiO2 from the hexylamine-propanethiol film after selenization near the dark mark on the surface.

4.5 Nanoparticle Ink CIS Cells on planar TiO_2

For the final class of devices prepared, a planar structure of dense TiO_2 on FTO glass was used instead of the mesoporous layer. It was shown by Dr. Charles Hages that by coating the Mo surface in selenium before depositing a CZTS nanoparticle ink, the large grains would nucleate and grow from the back of the device rather than from the front as is traditionally observed for nanoparticle-based devices.[138] The hope was that the fine grain layer could be completely avoided or removed from the surface leaving only a polycrystalline film composed of large grains. Preliminary results were promising, though the presence of the fine grain layer on top of the film near the junction with the CdS prevented the formation of an effective p-n junction. Also, the bottom-up sintering of the devices proceeded best in the absence of selenium and with fine control provided by a rapid thermal processing furnace powered by halogen lamps, or when the films were covered in a thin silica layer, though this silica layer acts as an insulator preventing device formation.

If the CdS could be replaced with TiO_2, and bottom-up sintering could be achieved on top of the TiO_2, the device would have two advantages. It would not contain a fine grain layer, with the grain boundaries providing potential areas for the excess holes to recombine, potentially lowering device output. The exposed surface could also be covered in a transparent conducting layer such as silver nanowires, creating a bifacial solar cell.[133] CdS cannot be used underneath the absorber as it will become CdSe during annealing and intermix with the absorber, losing its effectiveness. As TiO_2 is a very stable oxide, a TiO_2 film can withstand a high temperature anneal in a selenium

environment, potentially allowing the creation of a large-grain polycrystalline bifacial solar cell.

Semiconductor inks were made via the synthesis method described in McLeod et al. with the exception that the gallium acetylacetonate was replaced with an equimolar amount of indium acetylacetonate to make completely CIS particles.[51] TiO_2 films were prepared as described in Chapter 3. Following their preparation, they were placed in a low-vacuum (30mtorr) thermal evaporator consisting of a bell jar on a hot plate, with Se in a graphite boat. The TiO_2 film was mounted face down on a support with a shutter to allow the deposition of Se after heating. The Se was heated to 500°C for 10min before opening the shutter, and then the Se was allowed to evaporate onto the surface for 6min resulting in an approximately 250nm thick Se coating. This method is described in more detail by Dr. Charles Hages.[138] CIS inks consisting of 250mg of CIS nanoparticle per 1mL of hexanethiol solvent were prepared first by vortex mixing then by sonicating in a water bath for 15min to ensure the ink was thoroughly suspended. These inks were deposited on the TiO_2 surface by doctor-blading using 3 coats with 15μL of ink each coat with a 1 min anneal in air at 300°C following each coat. Three coats were used instead of two because the surface properties of the TiO_2 do not mimic that of Mo, and therefore the films remained too thin after only 2 coatings. These were annealed in a graphite box under argon with 360mg of Se at 500°C for 40minutes. Figure 4.16 shows a schematic of the basic film structure.

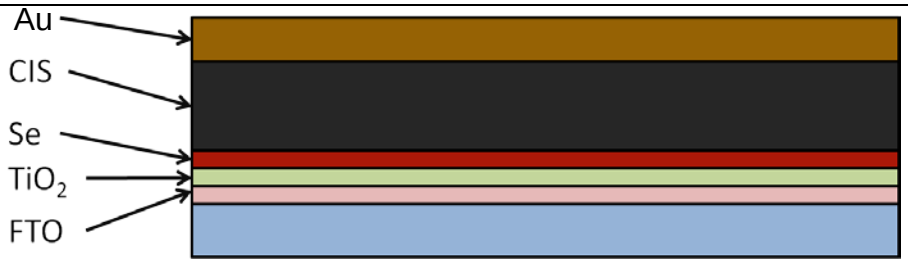

Figure 4.16: Schematic of a planar CIS-TiO2 device.

Several methods of creating a back electrical contact were examined, being roughly separated into methods that involved applying a metal only after the selenization process as an electrical contact, and those involving the deposition of a blocking layer of 50nm molybdenum and/or 250nm of gold as a blocking layer to inhibit nucleation at the top surface. These gold films were applied in manner identical to those described earlier in this chapter. Gold was chosen as it is one of few metals that are inert in the presence of selenium at 500°C and even known gold-telluride complexes break down at those temperatures. Molybdenum was chosen for its known compatibility as a substrate for CIGS and CZTS devices.

Interestingly, whenever gold was applied to these devices and annealed, while it did not react with selenium, after selenization, it coalesced into isolated micron-sized gold particles atop the film, whether of Mo or the bare CIS crystals, preventing it from being an effective contact. When contacted with probe tips, these gold structures showed a contact resistance of approximately 1MΩ. These gold particles are visible both in light microscopy and via SEM microscopy, shown in Figure 4.17. EDS confirmed the micron-sized particles consist almost completely of gold.

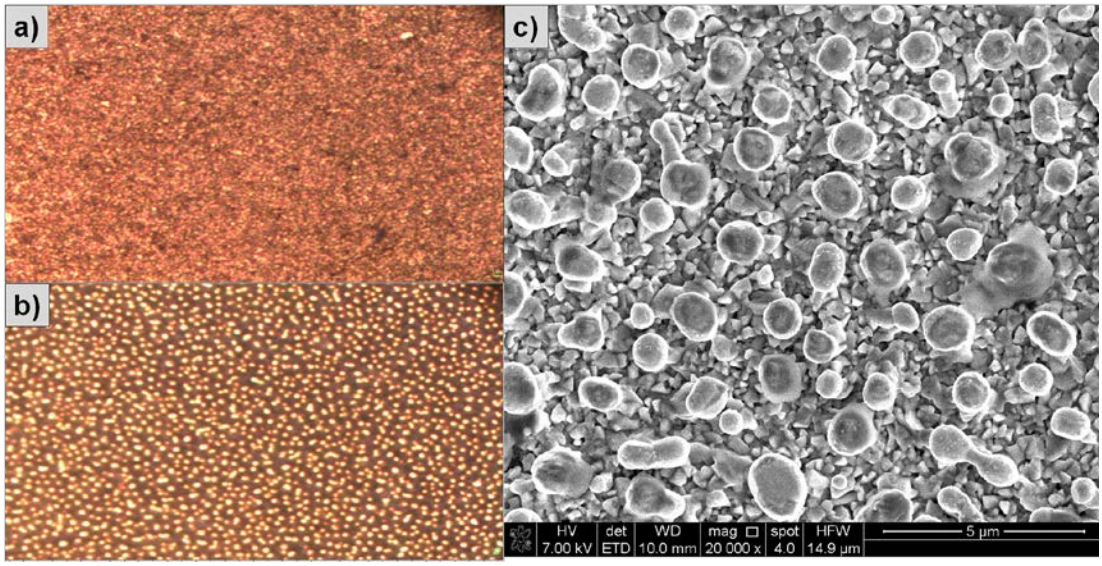

Figure 4.17: 1000x images of (a) an as-deposited 250nm Au film and (b) the isolated gold particles after annealing and (c) a detailed SEM image of the Au particles on CIS.

The XRD spectrum of these films showed no difference whether the Au films were deposited before or after the selenization procedure, with the exception of the relative intensities of the high angle gold peaks due to preferential ordering, as seen in **Figure 4.18**. This confirms that the CIS crystals anneal similarly in both cases and that the Au does not react with the selenium atmosphere.

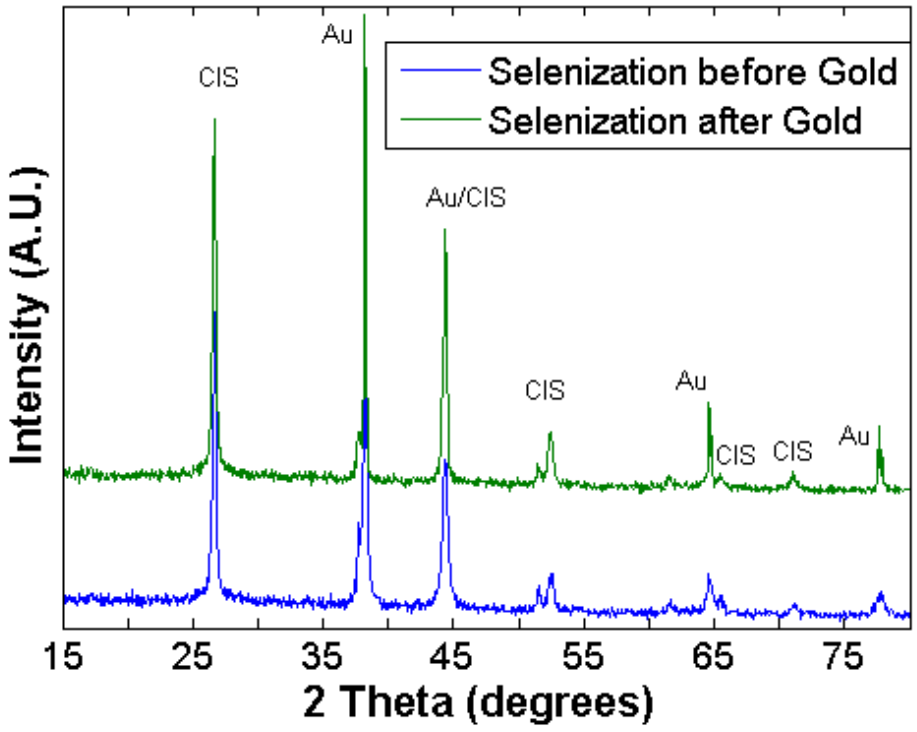

Figure 4.18: XRD spectrum of the gold films on selenized CIS, which are almost identical.

In an attempt to create a blocking layer for selenization and an effective back electrical contact, a variety of procedure orders were attempted to determine which would be most effective. In the simplest case, no evaporated selenium was used, and the CIS ink was selenized and an Au contact applied. In all the others, 250nm of selenium was deposited before the layer of ink. When gold was applied only before selenization, but not after, no electrical contact was formed due to the particle formation. An electron beam evaporator deposited 50nm of Mo at 1Å/s on top of two types of devices, with gold applied before selenization as well as after, or merely after selenization. None of the molybdenum devices showed any significant diode behavior, and acted merely as electrical conductors, indicating shorting within the device. The two cases of most interest are when gold is applied only after selenization, and when gold was applied both

before and after selenization. For simplicity, Figure 4.19 contains a visual layout of these different processes.

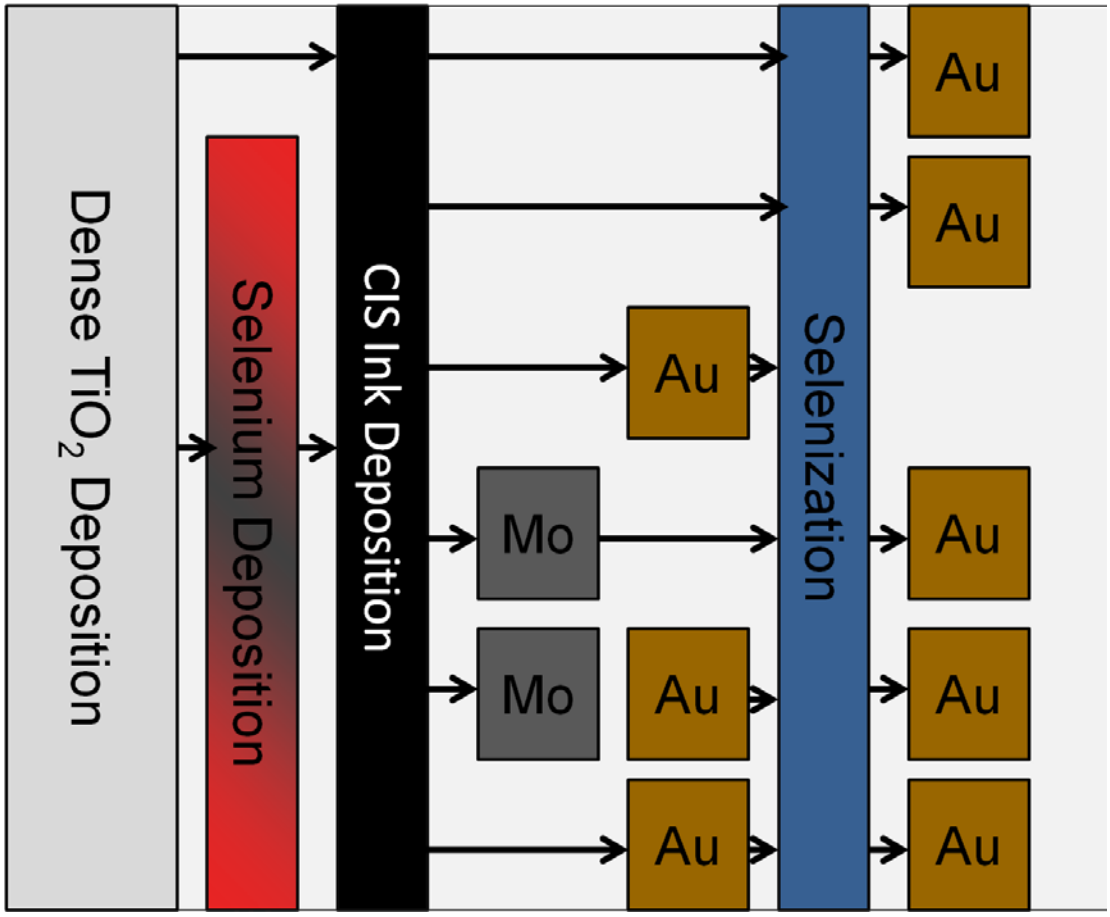

Figure 4.19: A visual representation of all of the blocking and contact layers attempted for planar CIS-TiO_2 solar cells.

The simplest devices prepared with no blocking layer or extra selenium layer showed no photovoltaic or diode activity and were electrically shorted, however they did show grain growth and a fine grain layer as the samples on Mo substrates. They also illustrate a particular challenge in obtaining cross-sections of these devices. They tend to fracture unevenly leaving layers in different planes. Particularly the Au overlayer will often stick out or even fold over. This problem seems to be common for the dense TiO_2

layers and makes it a challenge to measure thicknesses. The cross section of a simple CIS on dense TiO2 device is shown in Figure 4.20.

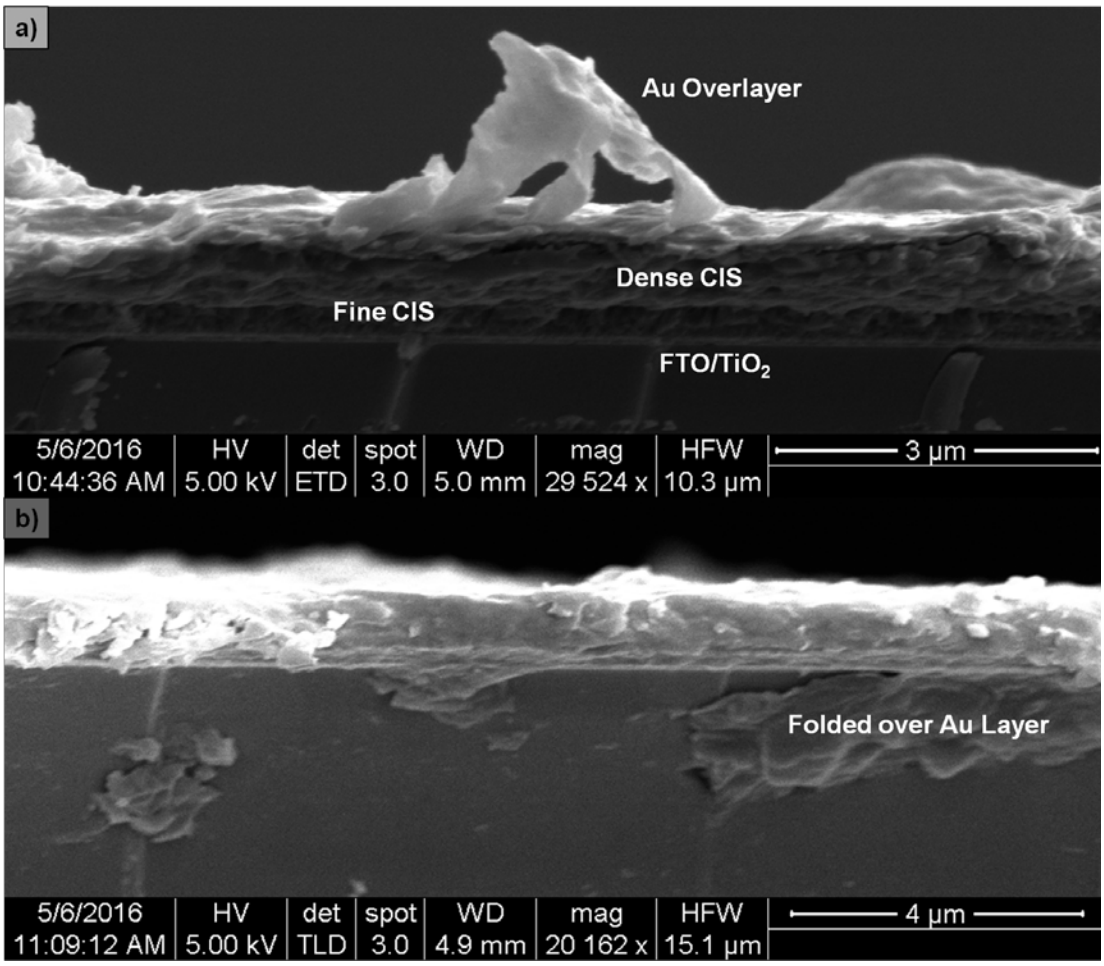

Figure 4.20: Cross section of CIS nanoparticles selenized on TiO2-FTO glass showing (a) a layer of dense CIS sticking forward attached to the Au overlayer, illustrating device structure and (b) elsewhere along the same edge where that overlayer has folded over blocking much of the view of the CIS.

When a selenium layer is deposited first and then the film is annealed in a selenium atmosphere without a blocking layer, and finished with an Au contact, the devices show diode behavior and photovoltaic activity. These cells show a "sandwich" style of grain growth with large grains occurring at both the top and bottom of the device with a fine grain layer in the middle. These devices also show significant uneven edges; however, in some locations this is advantageous as we are able to see a couple of areas lifted up

showing the structure of the film that was in contact with the TiO_2 surface. The bottom of the CIS structure is characterized by significant voids within the film which would significantly reduce the adhesion and quality of the p-n junction. This indicates that either the CIS crystals or the liquid Se during annealing have unfavorable surface interactions with the as-deposited TiO_2, and that some sort of surface treatment is necessary to improve the junction. Figure 4.21 shows the cross-sectional SEM images illustrating the sandwich layer and the porous structure. Figure 4.22 shows the J-V behavior of these devices. Out of 12 devices, 2 were completely shorted and showed little or no diode behavior. The best device exhibits an efficiency of 0.0004%, with a V_{OC} of 0.0475V, a J_{SC} of 24$\mu A/cm^2$, and a fill factor of 0.339. Significant shunting in reverse bias is again observed and this behavior is more significant under illumination.

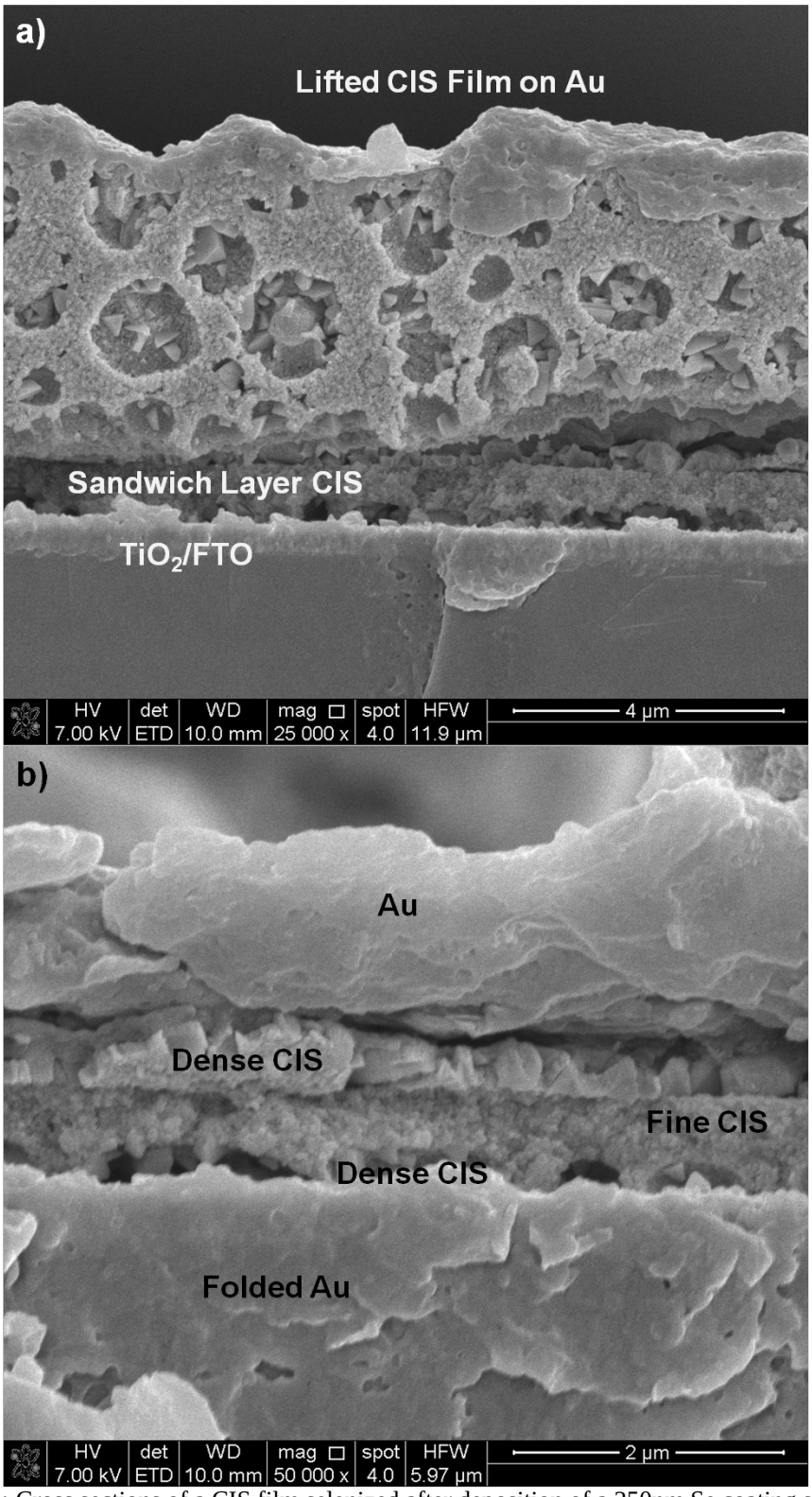

Figure 4.21: Cross sections of a CIS film selenized after deposition of a 250nm Se coating showing (a) a lifted up section showing the voids and poor contact at the be bottom surface and (b) the sandwich structure of the CIS film.

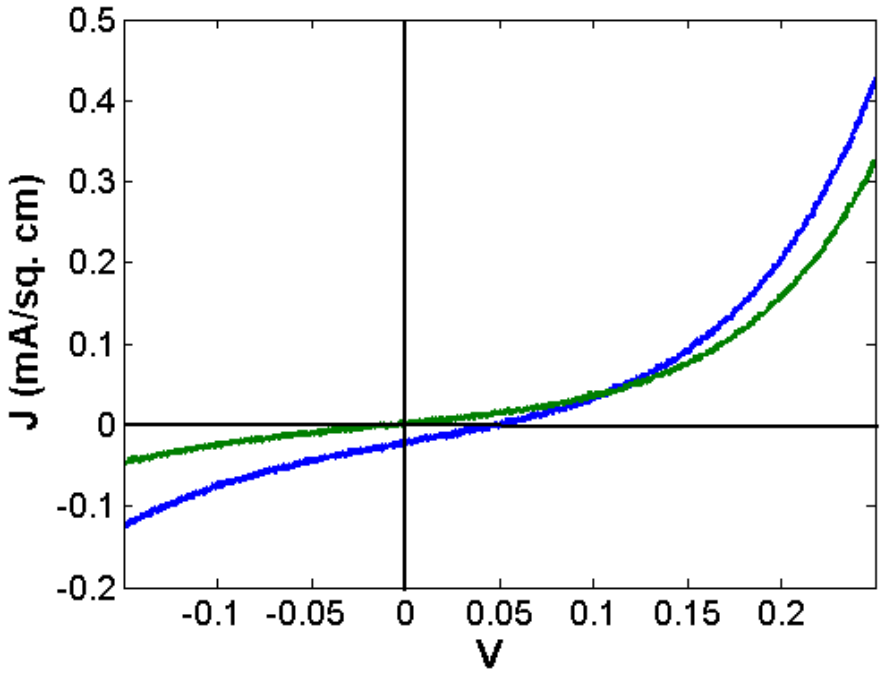

Figure 4.22: J-V behavior of a CIS device deposited on a TiO2 substrate covered in 250nm of Se, annealed in a selenium atmosphere and then finished with a gold contact.

As previously stated, the devices coated with Mo at any stage failed to show any diode behavior. This may because the Mo might have penetrated the surface of the CIS nanoparticles due to the high melting point and therefore high energy of the evaporated or sputtered Mo ions, or it may be due to other shunting within the devices. Figure 4.23 shows the complete lack of diode behavior for these devices. The gold on the Mo surface also forms small spherical particles as before; however, the molybdenum becomes discolored indicating reaction with selenium, but remains a uniform film.

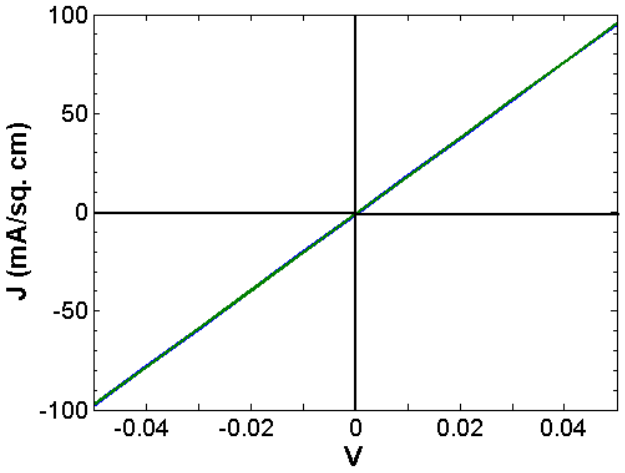

Figure 4.23: The completely shorted cell with Mo deposited on the CIS followed by Au before selenization.

The best devices with nanoparticle-based CIS on TiO_2 were obtained by depositing CIS on TiO_2 pre-coated with 250nm Se, followed by an Au blocking layer. The dense TiO_2 layers here underwent a $TiCl_4$ treatment as described for the mesoporous structure in an attempt to increase adherence by altering surface structure. The devices were selenized and another 250nm Au coating was deposited to provide a uniform electrical contact despite the separation of the initial Au coating. This increased the efficiency to 0.0013% or approximately a factor of 4 from the cells without a blocking layer. The V_{OC} increased slightly to 0.053V, while most of the improved efficiency comes from the approximately 4x increase in J_{SC} to 110μA/cm^2. Conversely the fill factor was reduced to 0.22. It is interesting that for any CIS or CIGS device on TiO_2, it is difficult to break the 120 μA/cm^2 barrier, and that for no device do we get significantly higher than this value, which is the same value as for a spiro OMeTAD cell on TiO_2 without CIGS. This may suggest that the CIGS must be having significant difficulties in transferring the electron charge carriers to the TiO_2, or even that our active junction is actually dominated by the

FTO-TiO_2 barrier. Figure 4.24 shows the J-V characteristics of the CIS on TiO_2 deposited with an gold blocking layer and separate gold contact with and without adjusting for shunt current as shown in Chavali et.al.[142]

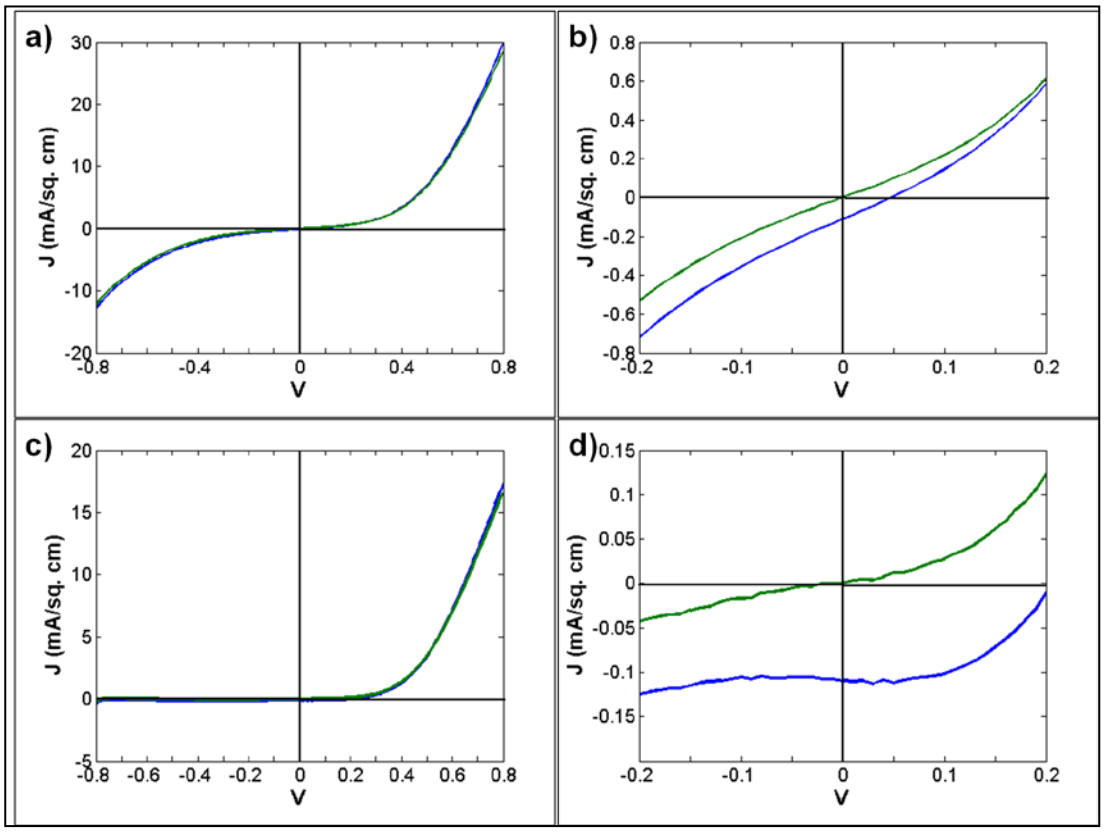

Figure 4.24: J-V performance of a CIS nanoparticle cell deposited on Se coated TiO_2 with an Au blocking layer and additional Au contact (a) without adjusting for shunt current, (b) a detail showing the range of photovoltaic performance, (c) after adjusting for shunt current, and (d) a detail of the shunt-adjusted J-V performance.

The cross-sections of these devices show a variety of different structures, likely due to the uneven nature of the Au coating on top of the film, due to its tendency to form small particles. Some areas were formed only of large micron-sized sintered grains, while others show a micron thick fine-grain pattern. This is of interest, because a full film densely sintered particles has not been observed for nanoparticle devices, and if it is possible to obtain only a dense layer, better devices may be possible. Some areas do

show poor adhesion, but in general these films adhere much better to the TiO_2 surface, indicating the $TiCl_4$ treatment helps, and that it may be possible to find a better surface-terminating agent for the TiO_2 to improve the device performance. Cross sections of the CIS film with both an Au blocking layer and an Au contact are shown in Figure 4.25, Figure 4.26 and Figure 4.27. This variability and the locations of poor adhesion are likely causes of device limitations and shunting; however, if they could be controlled, an efficient CIS-TiO_2 device may be possible.

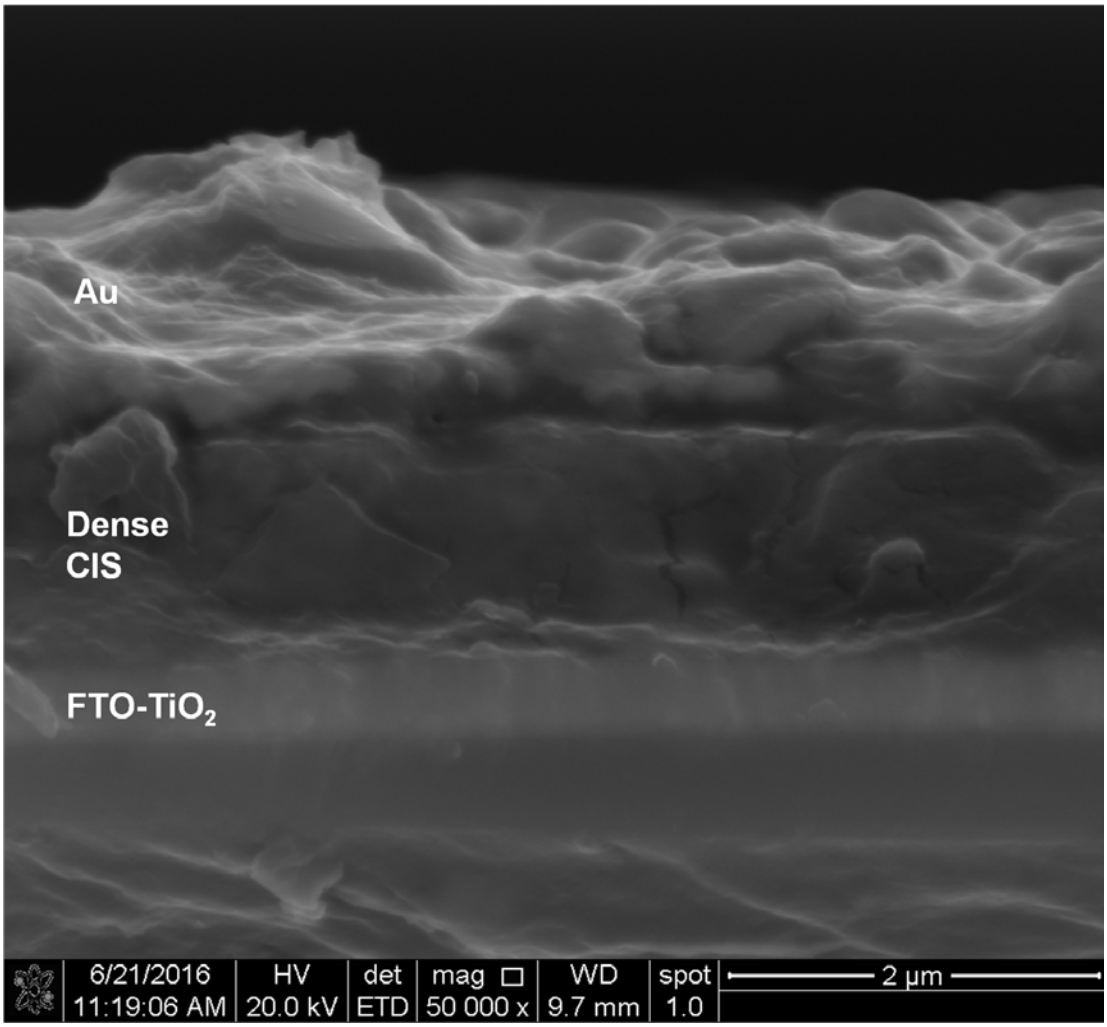

Figure 4.25: SEM cross-section showing a densely-sintered location on the cross section of the CIS film deposited on TiO_2 with an Au blocking layer and contact.

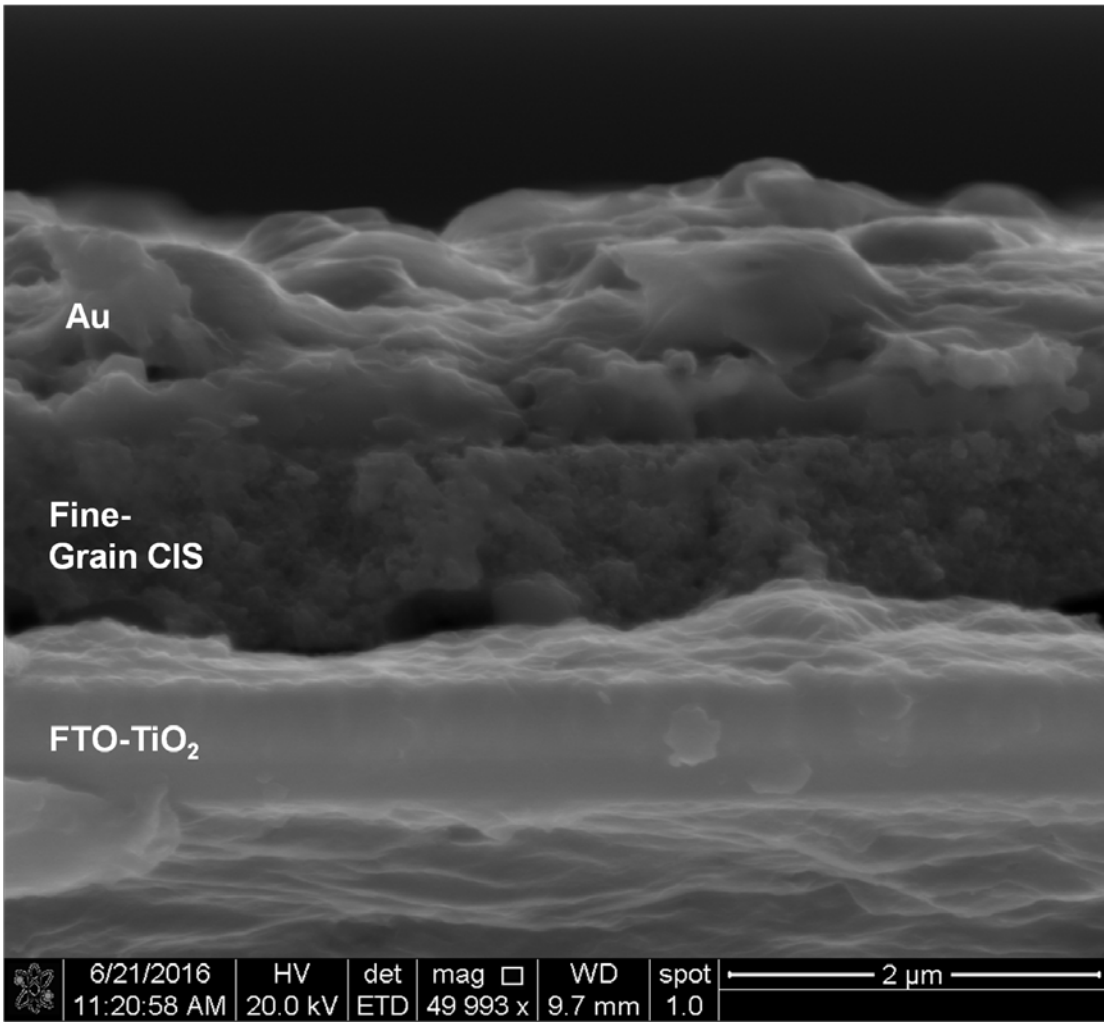

Figure 4.26: SEM cross section of the same film showing a different location with only a fine-grain layer and some voids at the back surface, indicating poor adhesion.

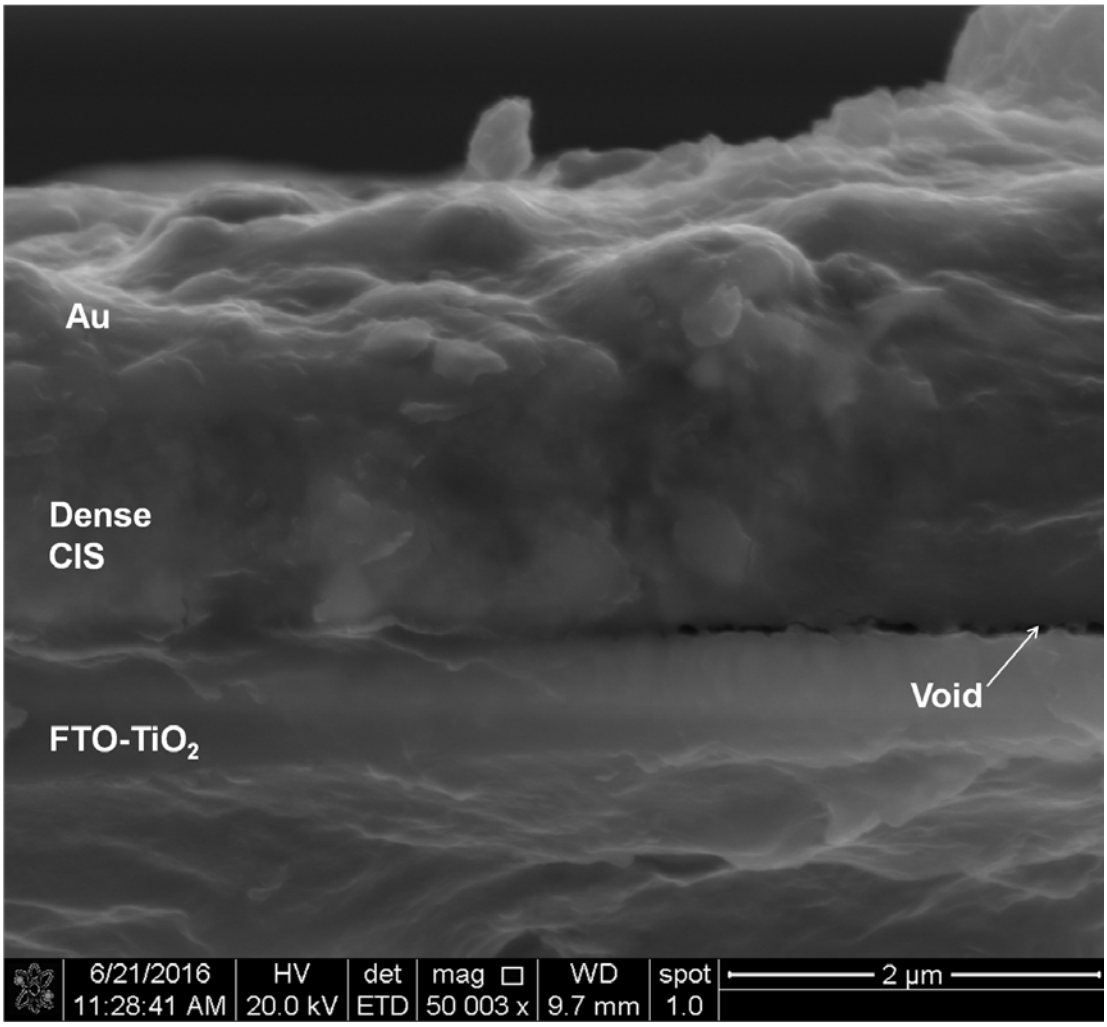

Figure 4.27: SEM cross section of the same showing a location with dense grains, but an extensive void which would not create solid electrical contact at p-n junction.

4.6 Conclusions and Future Work

CIS and CIGS devices can be created on both mesoporous and planar TiO_2 substrates. In both cases device efficiencies remain below 0.001% and are significantly limited by series resistance, shunt current and low short-circuit current. In all these cases, the short-circuit current density remains below 120µA/cm^2. This same current is obtainable with only spiro OMeTAD on mesoporous TiO_2, though due to the wider band

gaps of TiO_2 and spiro OMeTAD a much superior open circuit voltage and efficiency are obtainable. One of the major challenges is achieving a good metallurgical junction between the absorber and the TiO_2 due to poor wetting of the selenium growth agent or the unfavorable interaction with the crystal planes.

If these devices are to obtain efficiencies comparable to those of standard nanoparticle cells or cells with an ALD-deposited TiO_2 buffer layer, work is needed to determine an effective surface treatment to significantly lower the surface energy at that interface. These treatments could be tested by melting a Se pellet on the surface and observing the contact angle. The use of sulfuric or nitric acid should leave hydroxyl-terminated surface sites which may be more favorable, or which could be reacted with another reagent through a dehydration reaction that could show much better improved surface properties.

For nanoparticle-based planar CIS-TiO_2 cells, an effective conductive blocking layer or a methodology using an RTP to avoid surface nucleation would significantly improve the uniformity of these devices. Au could potentially be used as a blocking layer if the thickness were increased or decreased to minimize the coalescence behavior of the Au thin film.

These devices show interesting behavior that may be optimized to create more efficient TiO_2-CIS devices or bifacial solar cells; however, unless drastic increases can be made in their photocurrent, these devices may not be effective. An alternative explanation for the low photocurrent may be a large electrical barrier between the conduction band of the CIS and the TiO_2. This barrier could be reduced by alloying the

CIS absorber material with a significant amount of copper gallium selenide, increasing the conduction band position.

CHAPTER 5. ON THE DISSOLUTION MECHANISM OF SEMICONDUCTOR PRECURSORS IN AMINE-THIOL SOLUTIONS

5.1 Motivations and Background

Amine-thiol solutions have been used to create a wide variety of semiconductor materials, including CZTS,[70] CIGS,[54] and a variety of binary semiconductors including sulfides, selenides and chalcogenides.[71,102,143] Initially, these solvents were used without a clear explanation as to their mechanism. The combination of amines and thiols was initially shown to dissolve compounds that neither component can dissolve individual by Walker et al. in the case of selenium.[100] In these solutions the oxidation of thiols to disulfides allowed for the reduction of selenium with an amine acting as a solvent, after which the thiols could be distilled while the reduced selenium remained in solution.

A better understanding of the mechanism of dissolution would provide a rational method to determine which precursors and processing conditions are likely to yield semiconductor materials with minimal contamination and improved structures and defects. A general mechanism allows for the removal of counter-ion residues before or during annealing. Further, multivalent often exhibit redox chemistry, such as copper (II) being reduced to copper (I), or zinc metal that becomes Zn^{2+} ions. Understanding the source of these redox reactions is essential to control the valency of these ions to form the desired crystal structure, such as the +5 oxidation state required for many I_3-V-VI_4 semiconductors.

Some recent work agrees with and tends to confirm the mechanism proposed here that was first hypothesized in the early fall of 2014. Particularly Buckley et al. seeks to identify the dissolution mechanism for tin compounds and metal, also identifying the compounds as metal thiolates.[102] The best known thiolate compounds involve gold, silver and copper(I) metal cations, which have been extensively studied.[107] The higher electronegativity of these metals creates stronger, more covalent bonds with sulfur atoms.

5.2 Proposed Mechanism

Here we present a general hypothesis of the mechanism of action for the dissolution of various precursors in amine-thiol. The mechanism must be able to provide an explanation for the following phenomena:

1. The ability to dissolve a variety of salt precursors
2. The reduction of chalcogenides in solution
3. The oxidation of a variety of pure metals allowing dissolution
4. The observed reduction of copper (II) ions to copper (I) ions
5. The stability of chalcogenides when the thiol is removed.

The proposed mechanism of dissolution in the amine-thiol mixtures relies on the acid-base behavior of amines and thiols. Alkane thiols are known to have an acid-base dissociation constant (pK_a) in the range around 9-10 depending on substituent groups, which is similar to the pK_a of the alkylammonium conjugate acids of amines.[144] While not exact values, as these pK_a values are measured in water and not in organic solvents, their comparable values indicate that proton transfer between the amines and thiols in a mixture is not only possible but potentially favorable, and that a small percentage of these

molecules are likely to exist in their ionic states in the mixture. The presence of these ions provides the foundation of the proposed dissolution mechanism.

When a salt is dissolved in amine-thiol solution, the metal cation can bind to free thiolate ions in solution, while the counter-anion can be stabilized with the alkylammonium ion. Thus, any salts with metal cations that bind strongly to sulfur should be soluble, as would any that interact strongly with ammonium functional groups through substitution reactions or ionic bonds.

The presence of these ions alone does not explain the redox behavior of this solvent in being able to simultaneously reduce and oxidize metals or reduce chalcogens. However, thiols and thiolates are known to act as reducing agents, combining to form disulfides. The strength and favorability of these reactions is known to depend strongly on the stability of the resulting disulfide, and when small rings are possible, this reaction may be quite favorable. For example, 1,4-butanedithiol can form a 6-membered disulfide ring, and is a particularly effective reducing agent.[144] Rings, dimers and polymers are all possible for a variety of thiols and dithiols. In this case, the one electron per sulfur atom is transferred to an oxidizing agent, and two sulfur atoms for a disulfide bond. Figure 5.1 shows how a chalcogenide, Se, could be reduced by thiolates, in this example, 1,4-butanedithiolate. Copper (II) ions, or other metal ions could be reduced in a like manner.

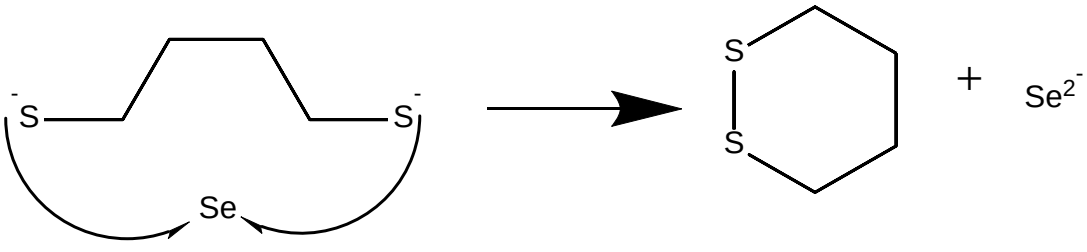

Figure 5.1: Potential reduction mechanism for chalcogenides with thiolates acting as a reducing agent.

Oxidation should be much more difficult in these solutions, as the most probable oxidation agent is the H^+ and R-NH_3^+ ions in solution reacting to create metal cations and hydrogen gas. This would indicate that only metals that have a redox potential higher than the hydrogen electrode in these solvents would react. The trend would loosely follow the redox potential observed in water, with reactive metals such as zinc or aluminum being more soluble, though metals that bind much more strongly to sulfur, such as silver and copper would be more soluble, while metals that bind more strongly to oxygen would be less soluble, and their native oxides may even inactivate the solution to dissolution. The most common oxidation state would depend on the ion that interacts most strongly with thiolate ligands, for example copper (I) which is unstable in water may be far more stable in amine-thiol solutions.

The stability of the chalcogen when the thiol is removed can be understood by the thiol only being necessary as a reducing agent with the amine as solvent. Conversely, the removal of the thiols would break apart metal-thiolate complexes according to Le-Chatlier's principle, resulting in the precipitation of these metals.

In summary, for this dissolution the proposed mechanism is as follows: the thiols protonate a small quantity of amines, forming thiolates and alkylammonium ions. The

thiolates are able to stabilize cations in solution, while the alkylammonium ions stabilize cations. Amines act as a solvent. Thiolates act as reducing agents, forming disulfides, and protons on the thiolates or alkylammonium ions act as oxidizing agents for reactive metals. Figure 5.2 summarizes this basic mechanism.

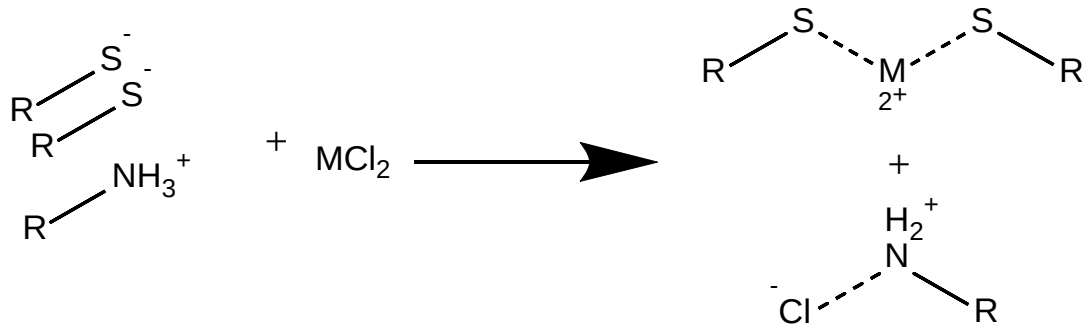

Figure 5.2: A simplified explanation of the dissolution of a metal (M) chloride salt in an amine-thiol mixture.

5.3 Support for the Mechanism

Several observations in literature as well as in various lab experiments confirm these results. Webber et al. observe that the electrical conductivity of a ethylenediamine-ethanedithiol solution increases several orders of magnitude over that of either solvent individually.[104] Lab mates have confirmed this conductivity increase for both thiols and dithiols in ethylene diamine, as well as for solutions of copper chloride in thiol-amine solutions. The increase in conductivity upon mixing indicates the presence of ions in solution. The conductivity of the salt solutions indicates that the salts are dissolved in separate, mobile ionic forms and not as bound molecules.

Our collaborators in Prof. Hilkka Kenttämaa's research group have observed the presence of a variety of thiolates, metal thiolate complexes, ammonium ions and ammonium chloride adducts via high resolution Orbitrap tandem mass spectrometry with

an electrospray ionization source for both CuCl and $CuCl_2$ in amine-thiol solutions. These solutions additionally contain copper bound in complexes containing both thiolates and chlorides. These complexes explain the large amount of residual chloride in the deposited films. The presence of alkylammonium chloride adducts supports the hypothesis that anions are stabilized by the ammonium ions.

To confirm these results, several in-lab experiments were performed. A variety of amine-thiol solutions were prepared and allowed to evaporate naturally at room temperature in a nitrogen glovebox to maintain the dissolved species in as natural of a state as possible. Complete evaporation required approximately 12 hours, and the films were placed in a low vacuum chamber afterwards to remove as much residual thiol as possible. A variety of solutions were prepared in butylamine and propanethiol, and slowly evaporated for examination via UV-Vis spectroscopy and from I-V curves. Solutions included the following: 0.1M germanium iodide and 0.2M selenium, 0.1M lead(II) iodide, 0.1M gallium acetylacetonate and 0.15M selenium and 0.1M copper chloride and 0.05M selenium. Solutions were prepared by weighing an appropriate amount of solids for 2mL of solution at twice the desired concentration. The salts and chalcogenide solutions were measured and dissolved separately. 1mL of amine was added, and then 1mL of thiol was added to each vial. Adding in the reverse order causes significant bubbling and a large amount of gas to be released. After at least 1 hour, a like amount of selenium solution and cation salt were mixed. Additionally, CZTS precursors containing copper (I) chloride, zinc chloride and tin(II) chloride, sulfur and selenium were prepared as explained in Zhang et al.[70] The solutions of greatest interest were those of germanium iodide and selenium, gallium acetylacetonate and those of the CZTS

precursors. The other materials did not show a strong absorption edge below 3eV or any XRD structure, indicating they were amorphous solids.

After deposition on glass, each was measured using an ultra-violet and visible (UV-Vis) light spectrometer to determine an absorption edge. To determine this edge, linear interpolation of the square of the absorptivity was used to fit a line to the absorption redge, and the intercept at the 0 absorption axis was taken as the beginning of the absorption edge, which would be equivalent to the bandgap for an indirect band gap.

The germanium-iodide material showed a spectral edge at ~3eV when evaporated at room temperature, and showed a pale yellow color. Upon annealing 50°C it remained the same. Annealing at 100ºC reduced this to 2.25 eV and left the film a darker yellow. Annealing at 200ºC left an orange residue with an absorption edge at 1.9 eV. The complexes apparently break down starting at around 100ºC, slightly above the 78ºC boiling point of butylamine and 68°C boiling point of propanethiol, indicating that the evaporation of the solvent results in the breakdown of these complexes. The material remains amorphous until annealed at 200°C, at which point it has an XRD pattern as shown in Figure 5.3. All of these samples show a strong XRD peak at 5° which is scaled out of the image as it is 1-2 orders of magnitude larger than the remaining peaks. The structure does not match any known germanium iodide or sulfide compounds, though it bears cosmetic similarities to methylammonium iodide salts, and may be such a material.

The gallium acetylacetonate and selenium solution shows no XRD behavior or absorption edge until annealed at 100°C or higher, after which it becomes an orange glassy solid. Gallium sulfides may form glassy solids with lanthanum doping, but are not known to do so on their own. It is possible that the presence of carbon or the mixed

sulfoselenide form creates this glassy state. It doesn't show any conductivity as the film is full of cracks, as in Figure 5.4. It may prove an interesting material to examine. As it contains no chloride or iodide salts, if the diffraction peaks are caused by alkylammonium halide salts, the lack of these peaks is to be expected.

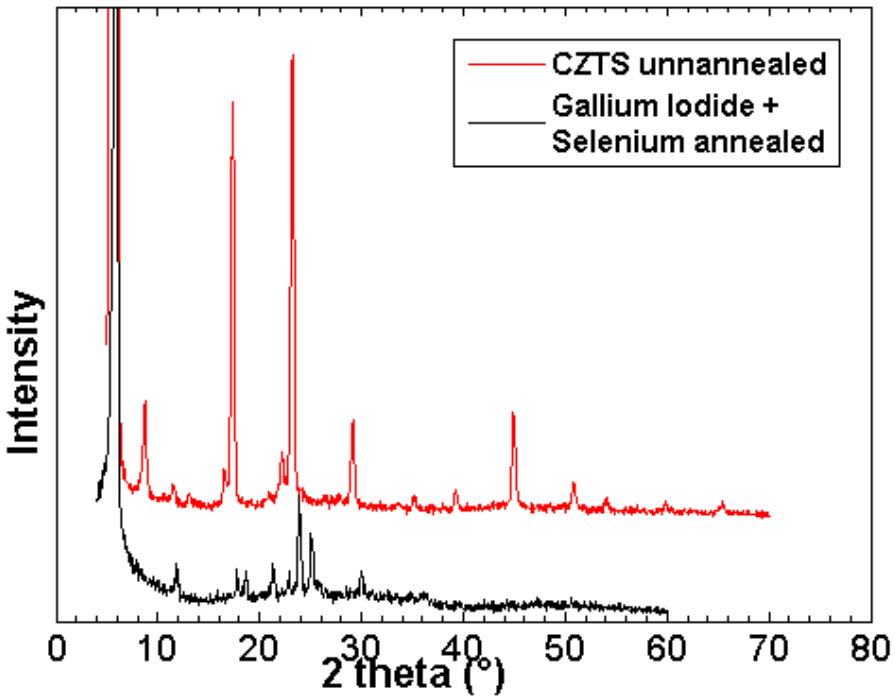

Figure 5.3: GIXRD patterns of germanium iodide and selenium in BA/PT and of CZTS precursors in BA/PT.

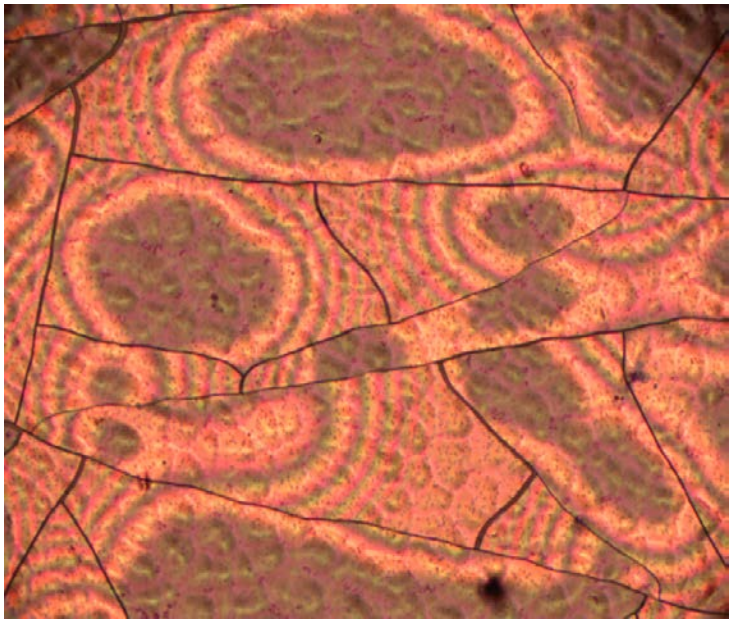

Figure 5.4: Light 1000x microscope image of the annealed $GaAcAc_3$ and Se film showing the extensive cracks in the film.

The films of greatest significance are those of the CZTS precursors. They show a significant XRD pattern when annealed at room temperature, as shown in Figure 5.3. This XRD pattern does not change when another thiol is substituted in the place of propanethiol, nor does it change when the sulfur and selenium ratio is adjusted, and with the exception of one peak at 7°, even in the absence of chalcogen, though when the amine is substituted, the pattern shifts significantly. This indicates that the XRD peaks observed involve primarily the amine in a complex and neither sulfur nor the thiol. As thiolates are the only known metal-containing species in solution, the peaks can likely be attributed primarily to the presence of a butylammonium chloride complex. To test this theory, the films were briefly washed in water as metal thiolates should not be soluble in water but butylammonium chloride salts should be soluble. Upon a simple water rinse, a white supporting matrix is removed, the water becomes slightly acidic (pH=5), and most of the XRD pattern disappears immediately. Only part of the peak at 5.5° remains, likely due to

its high signal and the imperfect washing of the film, and it is reduced in intensity by 75%. Normally the CZTS films corrode in under 12 hours in air to form a teal-coored copper patina, which is usually indicative of chloride presence, however, after washing the corrosion process is slowed to about 2 weeks, indicating significant removal of chloride species. From this it is possible to conclude that an ammonium chloride is indeed formed, and that the residual material is an amorphous metal-thiolate complex of some nature. This is corroborated by the presence of these structures in mass spectrometry. Figure 5.5 shows the XRD patterns for these CZTS precursors under all os these various conditions.

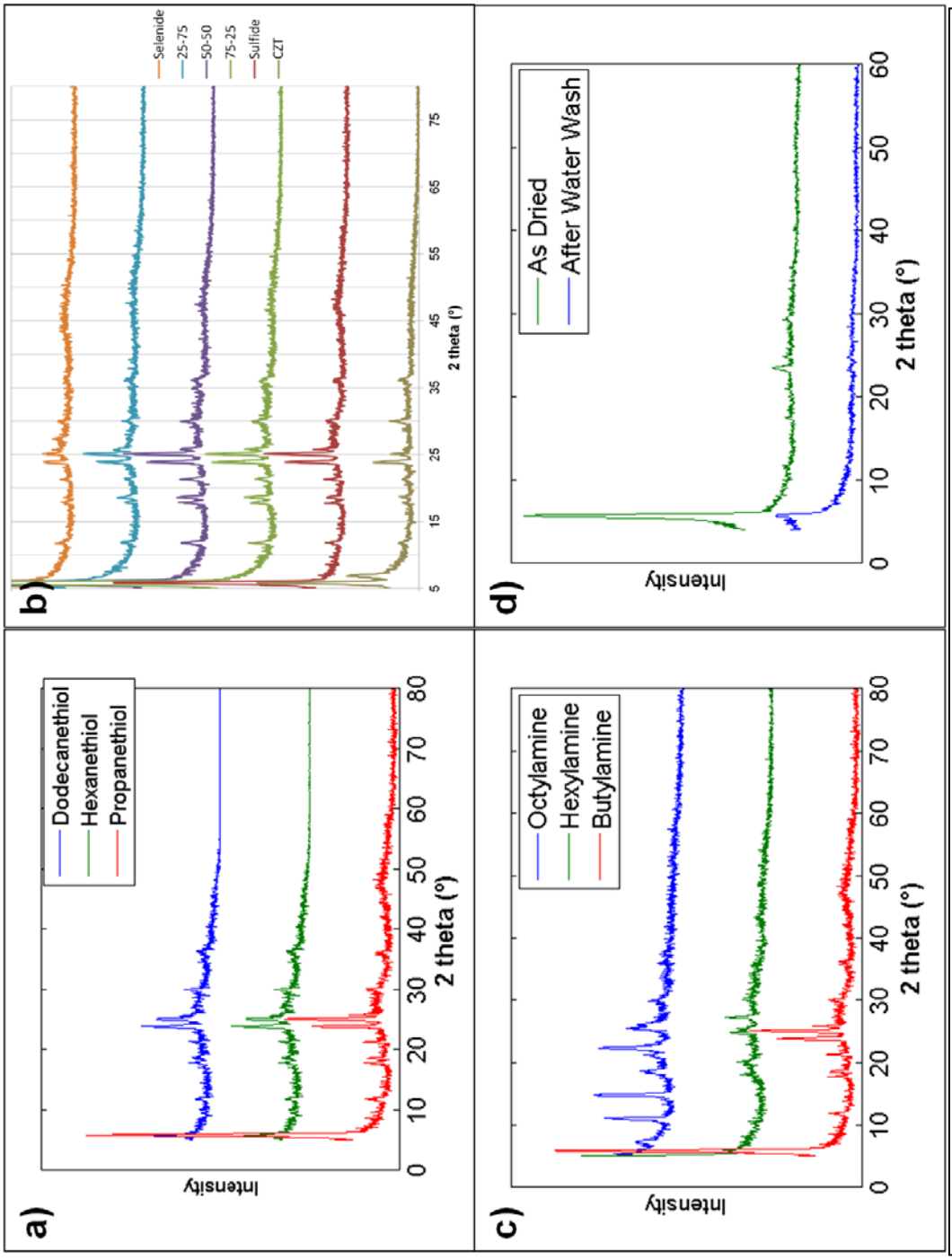

Figure 5.5: XRD patterns of unannealed CZTS amine-thiol precursors showing the uniform behavior with (a) changing thiols, (b) changing selenium: sulfur ratios, (c) and the noticeable changes from changing the amine and(d) washing with water.

5.4 Conclusions

The proposed dissolved species from metals, salts and chalcogenides dissolved in amine-thiol solution do appear to be various metal-thiolates with trace contaminants from anions present in the salt, and counter-ions mostly stabilized by forming a complex with alkylammonium ions. These compounds tend to break down when heated over the boiling point of the amines and thiols, though depending on the anion, the ammonium complexes may remain if they are thermally stable, such as ammonium iodide. These compounds themselves are not conductive and are not phase pure, making it difficult to foresee any use as semiconductors, though when annealed at higher temperatures they will decompose to semiconducting materials that have been made into useful devices.

CHAPTER 6. CONCLUSIONS

In conclusion, CdS is widely used as a buffer layer for thin film inorganic solar cells due to its high effectiveness. While light absorbed in the CdS window layer shows poor quantum efficiencies due to recombination efficiency, the proper optimization of the CdS thickness can improve device performance. Increasing the thickness of the CdS layers from 50nm to 70nm for CZTS nanoparticle cells significantly decreases shunting and can improve the device performance, as the current losses in the thicker CdS are counterbalanced by better overall performance. Further work should see if the same effect is observed for CIGS nanoparticle devices. A quartz microbalance was set up and a process developed to measure the growth of the CdS layer in situ, with a 1nm resolution.

Both mesoporous and planar TiO_2 substrates on FTO glass were developed as a replacement for Mo substrates and the CdS/ZnO buffer layer. These substrates are largely unaffected by annealing in a selenium atmosphere, which allows CIGS and CZTS thin films to be created on top of these structures and selenized. The mesoporous structure can be broken down by the selenization process through capillary forces and is largely destroyed if the absorber material is filled too densely in the pores, as it may expand upon annealing. These devices do not achieve efficiencies greater than 0.004% as presently fabricated, and are limited severely by shunting, high series resistance and short circuit current densities below $120\mu A/cm^2$. Major reasons for this poor

performance include poor contact and wetting between the TiO_2 and the absorber layer, the resistance in a TiO_2 structure and FTO, and the difficulty of reliably nucleating grain growth at the TiO_2-absorber surface. Grids under the TiO_2 may improve resistance issues, if they are stabilized against oxidation and selenization. To achieve better adherence to the TiO_2, surface modifications are necessary through an as yet unknown surface treatment.

Finally, a dissolution mechanism for amine-thiol precursors was hypothesized and supported by x-ray diffraction measurements and solubility tests. This mechanism consists mainly of the partial deprotonation of the thiol by the amine, the creation of metal-thiolates in solution and alkylammonium complexes. These observations are confirmed by our collaborator's work in tandem mass spectrometry. A manuscript containing their results is under preparation but has not been published at the time of writing of this thesis.

REFERENCES

REFERENCES

1. Bequerel, A.-E. Recherches sur les effets de la radiation chimique de la lumiere solaire au moyen des courants electriques. *Comptes Rendus L´Academie des Sci.* **9,** 145–149 (1839).
2. Adams, W. G. & Day, R. E. The Action of Light on Selenium. *Philos. Trans. R. Soc. London* **167,** 313–349 (1877).
3. Chapin, D. M., Fuller, C. S. & Pearson, G. L. A New Silicon p-n Junction Photocell for Converting Solar Radiation into Electrical Power. *J. Appl. Phys.* **25,** 676 (1954).
4. Alan Herries Wilson. The Theory of Electronic Semi-Conductors. *Proc. R. Soc. London. Ser. A,* **133,** 458–491 (1931).
5. Bhandari, K. P., Collier, J. M., Ellingson, R. J. & Apul, D. S. Energy payback time (EPBT) and energy return on energy invested (EROI) of solar photovoltaic systems: A systematic review and meta-analysis. *Renew. Sustain. Energy Rev.* **47,** 133–141 (2015).
6. Wedepohl, K. H. The composition of the continental crust. *Geochim. Cosmochim. Acta* **59,** 1217–1232 (1995).
7. D. C. Reynolds, G. Leies, L. L. Antes, and R. E. M. Photovoltaic Effect in Cadmium Sulfide. *Phys. Rev.* **96,** 533–534 (1954).

8. Martinuzzi, S. Trends and problems in thin film solar cells: A review. *Sol. Cells* **5,** 243–268 (1982).

9. Reynolds, D. C., Greene, L. C. & Antes, L. L. Properties of a Cadmium Sulfide Photorectifier. *J. Chem. Phys.* **25,** 1177 (1956).

10. Grimmeiss, H. G. & Memming, R. P-n Photovoltaic Effect in Cadmium Sulfide. *J. Appl. Phys.* **33,** 2217–2222 (1962).

11. Williams, R. & Bube, R. H. Photoemission in the photovoltaic effect in cadmium sulfide crystals. *J. Appl. Phys.* **31,** 968–978 (1960).

12. Nicoll, F. H. Large Area High-Current Photoconductive Cells using Cadmium Sulfide Powder. *Journal of the Optical Society of America* **45,** (1955).

13. Chamberlin, R. R. & Skarman, J. S. Chemically sprayed thin film photovoltaic converters. *Solid. State. Electron.* **9,** 819–820 (1966).

14. Clarke, R. L. Diffusion of copper in cadmium sulfide crystals. *J. Appl. Phys.* **30,** 957–960 (1959).

15. Kitaev, G. A., A. A. Uritskaya, and S. G. M. Conditions for the chemical deposition of thin films of cadmium sulphide on a solid surface. *Zhurnal Fiz. Khimii* **38,** 2065 (1965).

16. Fraas, L. M. & Ma, Y. CdS Thin Films for Terrestrual Solar Cells. *J. Cryst. Growth* **39,** 92–107 (1977).

17. Bube, R. H. Photoconductivity of the Sulfide, Selenide, and Telluride of Zinc or Cadmium. *Proc. IRE* **43,** 1836–1850 (1955).

18. Cusano, D. A. CdTe solar cells and photovoltaic heterojunctions in II–VI compounds. *Solid. State. Electron.* **6,** 217–218 (1963).

19. Kazmerski, L. L., White, F. R. & Morgan, G. K. Thin-film $CuInSe_2$/CdS heterojunction solar cells. *Appl. Phys. Lett.* **29,** 268–270 (1976).

20. Wagner, S., Shay, J. L., Bachmann, K. J. & Buehler, E. P-InP/n-CdS solar cells and photovoltaic detectors. *Appl. Phys. Lett.* **26,** 229–230 (1975).

21. Malik, I. J., Ryabova, E. & Skumanich, A. Materials Considerations for Pv Markets : Guideposts for Technology Directions. *IEEE Journal of Photovoltaics* 2873–2876 (2010).

22. Ito, K. & Nakazawa, T. Electrical and Optical Properties of Stannite-Type Quarternary Semiconductor Thin Films. *Jpn. J. Appl. Phys.* **27,** 2094–2097 (1988).

23. Wang, W. *et al.* Device characteristics of CZTSSe thin-film solar cells with 12.6% efficiency. *Adv. Energy Mater.* **4,** 1–5 (2014).

24. Gifford, J. Solar Frontier hits 22.3% on CIGS cell. *PV Magazine* (2015). Available at: http://www.pv-magazine.com/news/details/beitrag/solar-frontier-hits-223-on-cigs-cell_100022342/#axzz4BxvCeB00. (Accessed: 18th June 2016)

25. Wesoff, E. First Solar Hits Record 22.1% Conversion Efficiency for CdTe Solar Cell. *Greentech Media* (2016). Available at: http://www.greentechmedia.com/articles/read/First-Solar-Hits-Record-22.1-Conversion-Efficiency-For-CdTe-Solar-Cell. (Accessed: 18th June 2016)

26. Chen, S., Yang, J.-H., Gong, X. G., Walsh, A. & Wei, S.-H. Intrinsic point defects and complexes in the quaternary kesterite semiconductor Cu_2ZnSnS_4. *Phys. Rev. B* **81,** 245204 (2010).

27. Guo, Q. *et al.* Enhancing the performance of CZTSSe solar cells with Ge alloying. *Sol. Energy Mater. Sol. Cells* **105,** 132–136 (2012).

28. Graeser, B. K. *et al.* Synthesis of $(CuInS_2)_{0.5}(ZnS)_{0.5}$ Alloy Nanocrystals and Their Use for the Fabrication of Solar Cells via Selenization. *Chem. Mater.* **26,** 4060–4063 (2014).

29. Shin, D. *et al.* $BaCu_2Sn(S,Se)_4$ – Earth-Abundant Chalcogenides for Thin-Film Photovoltaics. *Chem. Mater.* acs.chemmater.6b01832 (2016). doi:10.1021/acs.chemmater.6b01832

30. Li, W., Liu, X., Cui, H., Huang, S. & Hao, X. The role of Ag in $(Ag,Cu)_2ZnSnS_4$ thin film for solar cell application. *J. Alloys Compd.* **625,** 277–283 (2015).

31. Boyle, J. H., McCandless, B. E., Shafarman, W. N. & Birkmire, R. W. Structural and optical properties of $(Ag,Cu)(In,Ga)Se_2$ polycrystalline thin film alloys. *J. Appl. Phys.* **115,** 0–8 (2014).

32. Xue, H. T., Lu, W. J., Zhu, Z. X. & Tang, F. L. Al-Doped $CuInSe_2$: A Study of Structural and Electronic Properties of a Photovoltaic Material. *Adv. Mater. Res.* **512-515,** 1543–1547 (2012).

33. Wang, C. *et al.* Design of $I_2-II-IV-VI_4$ Semiconductors through Element Substitution : The Thermodynamic Stability Limit and Chemical Trend. (2014).

34. Sheets, Erik J., Wei-Chang Yang, Robert B. Balow, Yunjie Wang, Bryce C. Walker, E. A. S. and R. A. An in situ phosphorous source for the synthesis of Cu3P and the subsequent converions to Cu_3PS_4 nanoparticle clusters. *J. Mater. Res.* **30,** 3710–3716 (2015).

35. Shi, T., Yin, W.-J., Al-Jassim, M. & Yan, Y. Structural, electronic, and optical properties of Cu_3-V-VI_4 compound semiconductors. *Appl. Phys. Lett.* **103,** 152105 (2013).

36. Balow, R. B., Sheets, E. J., Abu-Omar, M. M. & Agrawal, R. Synthesis and characterization of copper arsenic sulfide nanocrystals from earth abundant elements for solar energy conversion. *Chem. Mater.* **27,** 2290–2293 (2015).

37. Yang, B. *et al.* $CuSbS_2$ as a promising earth-abundant photovoltaic absorber material: A combined theoretical and experimental study. *Chem. Mater.* **26,** 3135–3143 (2014).

38. Bhattacharya, R. N. & Ramanathan, K. $Cu(In,Ga)Se_2$ thin film solar cells with buffer layer alternative to CdS. *Sol. Energy* **77,** 679–683 (2004).

39. Bhattacharya, R. N., Contreras, M. a. & Teeter, G. 18.5% Copper Indium Gallium Diselenide (CIGS) Device Using Single-Layer, Chemical-Bath-Deposited ZnS(O,OH). *Jpn. J. Appl. Phys.* **43,** L1475–L1476 (2004).

40. Witte, W., Spiering, S. & Hariskos, D. Substitution of the CdS buffer layer in CIGS thin-film solar cells. *Vak. Forsch. und Prax.* **26,** 23–27 (2014).

41. Hsu, W. *et al.* Electron-Selective TiO2 Contact for $Cu(In,Ga)Se_2$ Solar Cells. *Sci. Rep.* **5,** 16028 (2015).

42. Pant, A. *et al.* Fundamentals of lateral and vertical heterojunctions of atomically thin materials. *Nanoscale* **8,** 3870–3887 (2016).

43. Mottet, S., J. E. V. Thermionic Emission in Heterojunctions. in *Proceedings of the 3rd International Conference on Simulation of Semiconductor Devices and Processes* 97–108 (1988).

44. Wada, T., Kohara, N., Nishiwaki, S. & Negami, T. Characterization of the Cu (In, Ga) Se_2Mo interface in CIGS solar cells. *Thin Solid Films* **387,** 118–122 (2001).

45. Dhere, N. G. Scale-up issues of CIGS thin film PV modules. *Sol. Energy Mater. Sol. Cells* **95,** 277–280 (2011).

46. Friedlmeier, T. M. *et al.* Improved Photocurrent in Cu (In , Ga) Se_2 Solar Cells : 7–9 (2015).

47. Nakada, T., Hirabayashi, Y., Tokado, T., Ohmori, D. & Mise, T. Novel device structure for Cu(In,Ga)Se_2 thin film solar cells using transparent conducting oxide back and front contacts. *Sol. Energy* **77,** 739–747 (2004).

48. Hagendorfer, H. *et al.* Highly Transparent and Conductive ZnO: Al Thin Films from a Low Temperature Aqueous Solution Approach. *Adv. Mater.* 10.1002/adma.201303186 (2013). doi:10.1002/adma.201303186

49. Jung, S. *et al.* Effects of Ga contents on properties of CIGS thin films and solar cells fabricated by co-evaporation technique. *Curr. Appl. Phys.* **10,** 990–996 (2010).

50. Marudachalam, M. *et al.* Preparation of homogeneous Cu(InGa)Se_2 films by selenization of metal precursors in H2Se atmosphere. *Appl. Phys. Lett.* **67,** 3978 (1995).

51. McLeod, Steven M. , Charles J. Hages, N. J. C. and R. A. Synthesis and characterization of 15% efficient CIGSSe solar cells from nanoparticle inks. *Prog. Photovoltaics. Res. Appl.* **23,** 1550–1556 (2015).

52. Miskin, C. K. *et al.* 9.0% efficient $Cu_2ZnSn(S,Se)_4$ solar cells from selenized nanoparticle inks. *Prog. Photovoltaics Res. Appl.* n/a–n/a (2014). doi:10.1002/pip.2472

53. Lincot, D. *et al.* Chalcopyrite thin film solar cells by electrodeposition. *Sol. Energy* **77,** 725–737 (2004).

54. Zhao, X., Lu, M., Koeper, M. J. & Agrawal, R. Solution-processed sulfur depleted Cu(In, Ga)Se $_2$ solar cells synthesized from a monoamine–dithiol solvent mixture. *J. Mater. Chem. A* **4,** 7390–7397 (2016).

55. Jackson, P. *et al.* Properties of $Cu(In,Ga)Se_2$ solar cells with new record efficiencies up to 21.7%. *Phys. status solidi – Rapid Res. Lett.* **9,** 28–31 (2015).

56. Ng, P. *et al.* High Efficieny $Cu(In,Ga)Se_2$-Based Solar Cells of Novel Absorber Structures. *Sol. Energy* 68–75 (1994).

57. Schleussner, S., Zimmermann, U., Wutjen, T., Leifer, K. & Edoff, M. Effect of gallium grading in Cu(In,Ga)Se2 solar-cell absorbers produced by multi-stage coevaporation. *Sol. Energy Mater. Sol. Cells* **95,** 721–726 (2011).

58. Friedfeld, R., Ra, R. P. & Mantovani, J. G. Electrodeposition of CuInGaSe thin Films. *Sol. Energy Mater.* **58,** 375–385 (1999).

59. Dale, P. *et al.* Deposition and Characterization of Copper Chalcopyrite Based Solar Cells using Electrochemical Techniques. *ECS Trans.* **6,** 535–546 (2007).

60. Saji, V. S., Choi, I. H. & Lee, C. W. Progress in electrodeposited absorber layer for $CuIn_{(1-x)}Ga_xSe_2$ (CIGS) solar cells. *Sol. Energy* **85,** 2666–2678 (2011).

61. Guo, Q., Hillhouse, H. W. & Agrawal, R. Synthesis of Cu_2ZnSnS_4 Nanocrystal Ink and Its Use for Solar Cells. 11672–11673 (2009).

62. Guo, Q. *et al.* Development of $CuInSe_2$ nanocrystal and nanoring inks for low-cost solar cells. *Nano Lett.* **8,** 2982–7 (2008).

63. Guo, Q. *et al.* Fabrication of 7.2% efficient CZTSSe solar cells using CZTS nanocrystals. *J. Am. Chem. Soc.* **132,** 17384–6 (2010).

64. Guo, Q., Ford, G. M., Hillhouse, H. W. & Agrawal, R. Sulfide nanocrystal inks for dense $Cu(In_{1-x}Ga_x)(S_{1-y}Se_y)2$ absorber films and their photovoltaic performance. *Nano Lett.* **9,** 3060–5 (2009).

65. Barkhouse, D. Aaron R. , Oki Gunawan, Tayfun Gokmen, T. K. T. and D. B. M. Device characteristics of a 10.1% hydrazine-processed $Cu_2ZnSn(Se,S)_4$ solar cell. *Prog. Photovolt Res. Appl.* **20,** 6–11 (2012).

66. Mitzi, D. B. *et al.* Hydrazine-based deposition route for device-quality CIGS films. *Thin Solid Films* **517,** 2158–2162 (2009).

67. Todorov, Teodor K. , Oki Gunawan, T. G. and D. B. M. Solution-processed $Cu(In,Ga)(S,Se)_2$ absorber yielding a 15.2% efficient solar cell. *Prog. Photovolt Res. Appl.* **21,** 82–87 (2013).

68. Xin, H. & Hillhouse, H. W. 8.3% Efficient copper zinc tin sulfoselenide solar cells processed from environmentally benign solvent. *Conf. Rec. IEEE Photovolt. Spec. Conf.* 441–443 (2013). doi:10.1109/PVSC.2013.6744186

69. Uhl, A. R., Katahara, J. K. & Hillhouse, H. W. Molecular-ink route to 13.0% efficient low-bandgap $CuIn(S,Se)_2$ and 14.7% efficient $Cu(In,Ga)(S,Se)_2$solar cells. *Energy Environ. Sci.* **9,** 130–134 (2016).

70. Zhang, R., Szczepaniak, S. M., Carter, N. J., Handwerker, C. A. & Agrawal, R. A versatile solution route to efficient $Cu_2ZnSn(S,Se)_4$ thin-film solar cells. *Chem. Mater.* **27,** 2114–2120 (2015).

71. Zhang, R. *et al.* Metal–metal chalcogenide molecular precursors to binary, ternary, and quaternary metal chalcogenide thin films for electronic devices. *Chem. Commun.* **846,** 31–39 (2016).

72. Zhao, D. *et al.* Solution-deposited pure selenide CIGSe solar cells from elemental Cu, In, Ga, and Se. *J. Mater. Chem. A Mater. energy Sustain.* **00,** 1–5 (2015).

73. Kay, A. & Grätzel, M. Artificial Photosynthesis. 1. Photosensitization of TiO_2 Solar Cells with Chlorophyll Derivativesand Related Natural Porphyrins. *J. Phys. Chem.* **97,** 6272–6277 (1993).

74. Markham, S. C. Photocatalytic properties of oxides. *J. Chem. Educ.* **32,** 540 (1955).

75. Wrighton Mark S., Arthur B. Ellis, Peter T. Wolczanski, D. L. M. & Harmon B. Abrahamson, and D. S. G. Strontium Titanate Photoelectrodes. Efficient Photoassisted Electrolysis of Water at Zero Applied Potential. *J. Am. Chem. Soc.* **98,** 2774–2779 (1976).

76. Jamieson, J. C. and B. O. Pressure-Temperature Studies of Anatase, Brookite Rutile and TiO2(II): A Discussion. *Am. Minerol.* **54,** 1477–1481 (1969).

77. Hanaor, D. A. H. & Sorrell, C. C. Review of the anatase to rutile phase transformation. *J. Mater. Sci.* **46,** 855–874 (2011).

78. Scanlon, D. O. *et al.* Band alignment of rutile and anatase TiO_2. *Nat. Mater.* **12,** 798–801 (2013).

79. Kroemer, H., Chien, W. Y., Harris, J. S. & Edwall, D. D. Measurement of isotype heterojunction barriers by C-V profiling. *Appl. Phys. Lett.* **36,** 295–297 (1980).

80. Forro, L. *et al.* High mobility n-type charge carriers in large single crystals of anatase (TiO_2). *J. Appl. Phys.* **75,** 633–635 (1994).

81. Di Valentin, C., Pacchioni, G. & Selloni, A. Reduced and n-Type Doped TiO_2 : Nature of Ti^{3+} Species. *J. Phys. Chem. C* **113,** 20543–20552 (2009).

82. Nazeeruddin, M. K. *et al.* Conversion of Light to Electricity by cis-X2Bis(2,2'-bipyridyl-4,4'-dicarboxylate)ruthenium(II) Charge-Transfer Sensitizers (X = Cl-, Br-, I-, CN-, and SCN-) on Nanocrystalline TiO_2 Electrodes. *J. Am. Chem. Soc.* **115,** 6382–6390 (1993).

83. Mathew, S. *et al.* Dye-sensitized solar cells with 13% efficiency achieved through the molecular engineering of porphyrin sensitizers. *Nat. Chem.* **6,** 242–247 (2014).

84. Xia, J., Masaki, N., Jiang, K. & Yanagida, S. Sputtered Nb_2O_5 as a Novel Blocking Layer at Conducting Glass / TiO_2 Interfaces in Dye-Sensitized Ionic Liquid Solar Cells. *J. Phys. Chem. B* **110,** 25222 – 25228 (2007).

85. Fitzgibbons, E. T., Sladek, K. J. & Hartwig, W. H. TiO_2 Film Properties as a Function of Processing Temperature. *J. Electrochem. Soc.* **119,** 735 (1972).

86. Harizanov, O. & Harizanova, A. Development and investigation of sol-gel solutions for the formation of TiO<sub 2> coatings. **63,** 185–195 (2000).

87. Kavan, L. & Grätzel, M. Highly Efficient Semiconducting TiO_2 Photoelectrodes Prepared By Aerosol Pyrolysis. *Electrochim. Acta* **40,** 643–652 (1995).

88. Arend, H., Huber, W., Mischgofsky, F. H. & Richter-Van Leeuwen, G. K. Layer perovskites of the $(C_nH_{2n}+1NH_3)_2MX_4$ and $NH_3(CH_2)mNH_3MX_4$ families with M = Cd, Cu, Fe, Mn or Pd and X = Cl or Br: Importance, solubilities and simple growth techniques. *J. Cryst. Growth* **43,** 213–223 (1978).

89. Liang, K., Mitzi, D. B. & Prikas, M. T. Synthesis and Characterization of Organic−Inorganic Perovskite Thin Films Prepared Using a Versatile Two-Step Dipping Technique. *Chem. Mater.* **10,** 403–411 (1998).

90. Akihiro Kojima,† Kenjiro Teshima,‡ Yasuo Shirai, and T. M. Organometal Halide Perovskites as Visible- Light Sensitizers for Photovoltaic Cells. *J Am Chem Soc* **131,** 6050–6051 (2009).

91. Seo, J., Noh, J. H. & Seok, S. Il. Rational Strategies for Efficient Perovskite Solar Cells. *Acc. Chem. Res.* **49,** 562–572 (2016).

92. Saliba, M. *et al.* Cesium-containing Triple Cation Perovskite Solar Cells: Improved Stability, Reproducibility and High Efficiency. *Energy Environ. Sci.* **9,** - (2016).

93. Di Giacomo, F. *et al.* High efficiency $CH_3NH_3PbI_{(3-x)}Cl_x$ perovskite solar cells with poly(3-hexylthiophene) hole transport layer. *J. Power Sources* **251,** 152–156 (2014).

94. Heo, J. H. *et al.* Efficient inorganic-organic hybrid heterojunction solar cells containing perovskite compound and polymeric hole conductors. *Nat Phot.* **7,** 486–491 (2013).

95. Seok, S. Il. Methoxy Substituents in Spiro-OMeTAD for Efficient Inorganic − Organic Hybrid Perovskite Solar Cells. (2014). doi:10.1021/ja502824c

96. Hernández-Rodríguez, E., Rejón, V., Mis-Fernández, R. & Peña, J. L. Application of sputtered TiO_2 thin films as HRT buffer layer for high efficiency CdS/CdTe solar cells. *Sol. Energy* **132,** 64–72 (2016).

97. Wang, Z. & Demopoulos, G. P. Nanoscale Photo-Absorbing Kesterite Grown on Anatase Mesoscopic Films by Sequential Binary Chalcogenide Solution Deposition-Exchange, Annealing, and Etching. *Cryst. Growth Des.* acs.cgd.6b00033 (2016). doi:10.1021/acs.cgd.6b00033

98. Liu, Y. *et al.* Alkylthiol-enabled Se powder dissolution in oleylamine at room temperature for the phosphine-free synthesis of copper-based quaternary selenide nanocrystals. *J. Am. Chem. Soc.* **134,** 7207–10 (2012).

99. Walker, Bryce C., and R. A. in *38th IEEE Photovoltaic Specialists Conference* 2654–2657 (2012).

100. Walker, B. C. & Agrawal, R. Contamination-free solutions of selenium in amines for nanoparticle synthesis. *Chem. Commun.* **50,** 8331 (2014).

101. Webber, D. H., Buckley, J. J., Antunez, P. D. & Brutchey, R. L. Facile dissolution of selenium and tellurium in a thiol–amine solvent mixture under ambient conditions. *Chem. Sci.* **5,** 2498 (2014).

102. Buckley, J. J., McCarthy, C. L., Del Pilar-Albaladejo, J., Rasul, G. & Brutchey, R. L. Dissolution of Sn, SnO, and SnS in a Thiol-Amine Solvent Mixture: Insights into the Identity of the Molecular Solutes for Solution-Processed SnS. *Inorg. Chem.* **55,** 3175–3180 (2016).

103. Arnou, P., Cooper, C. S., Malkov, A. V., Bowers, J. W. & Walls, J. M. Solution-processed $CuIn(S,Se)_2$ absorber layers for application in thin film solar cells. *Thin Solid Films* **582,** 31–34 (2015).

104. Webber, D. H. & Brutchey, R. L. Alkahest for V_2VI_3 chalcogenides: dissolution of nine bulk semiconductors in a diamine-dithiol solvent mixture. *J. Am. Chem. Soc.* **135,** 15722–5 (2013).

105. McCarthy, C. L. *et al.* Earth Abundant $CuSbS_2$ Thin Films Solution Processed from Thiol-Amine Mixtures. *J. Mater. Chem. C* (2016). doi:10.1039/C6TC02117D

106. Yang, Y. *et al.* Solution-Processed Highly Efficient $Cu_2ZnSnSe=$ Thin Film Solar Cells by Dissolution of Elemental Cu , Zn , Sn , and Se Powders Solution-Processed Highly Efficient $Cu_2ZnSnSe_4$ Thin Film Solar Cells by Dissolution of Elemental Cu , Zn , Sn , and Se Powder. (2014). doi:10.1021/am5064926

107. Janssen, M. D., Grove, D. M. & Van Koten, G. Copper(I), lithium, and magnesium thiolate complexes: an overview with due mention of selenolate and tellurolate analogs and related silver(I) and gold(I) species. *Prog. Inorg. Chem.* **46,** (1997).

108. Miller, M. L., Ibrahim, S. A., Golden, M. L. & Darensbourg, M. Y. Adamantane-like Cluster Complexes of Mixed-Valent Copper − Copper and Nickel − Copper Thiolates. *Inorg. Chem.* **42,** 2176–2183 (2003).

109. Konôpka, M., Rousseau, R., Štich, I. & Marx, D. Detaching thiolates from copper and gold clusters: Which bonds to break? *J. Am. Chem. Soc.* **126,** 12103–12111 (2004).

110. Chang, J. & Waclawik, E. R. Colloidal semiconductor nanocrystals: controlled synthesis and surface chemistry in organic media. *RSC Adv.* **4,** 23505–23527 (2014).

111. Hsieh, Y. T. *et al.* Efficiency Enhancement of $Cu_2ZnSn(S,Se)_4$ Solar Cells via Alkali Metals Doping. *Adv. Energy Mater.* **6,** 1–6 (2016).

112. Winkler, M. T. *et al.* Optical designs that improve the efficiency of $Cu_2ZnSn(S,Se)_4$ solar cells. *Energy Environ. Sci.* **7,** 1029 (2014).

113. Contreras, M. A. *et al.* Optimization of CBD CdS process in high-efficiency $Cu(In,Ga)Se_2$-based solar cells. *Thin Solid Films* **403-404,** 204–211 (2002).

114. Kittel, C. *Introduction to Solid State Physics*. (John Wiley & Sons, INC, 2005).

115. Ramanathan, K., Wiesner, H., Asher, S., Niles, D. & Bhattacharya, R. N. High-Efficiency Cu (In , Ga) Se_2 Thin Film Solar Cells Without Intermediate Buffer Layers. *2nd World Conf. Exhib. Photovolt. Sol. Energy Convers.* 6 (1998).

116. Froment, M. & Lincot, D. Phase formation processes in solution at the atomic level: Metal chalcogenide semiconductors. *Electrochim. Acta* **40,** 1293–1303 (1995).

117. Lincot, D., Barges, R. O., Lincot, D. & Borges, R. O. Chemical bath deposition of cadmium sulfide thin films. In situ growth and structural studies by combined quartz crystal microbalance and electrochemical impedance. *J. Electrochem. Soc.* **139,** 1880–1889 (1992).

118. Ortega-Borges, R. Mechanism of Chemical Bath Deposition of Cadmium Sulfide Thin Films in the Ammonia-Thiourea System. *J. Electrochem. Soc.* **140,** 3464 (1993).

119. Ulrich, F.; Zachariasen, W. H. Ueber die Kristallstruktur des alpha- und beta Cd S, sowie des Wurtzits. *Zeitschrift fuer Krist. Krist. Krist. Krist.* **62,** 260–273 (1925).

120. Choi, H. *et al.* The effect of $TiCl_4$-treated TiO_2 compact layer on the performance of dye-sensitized solar cell. *Curr. Appl. Phys.* **12,** 737–741 (2012).

121. Ramasamy, K., Tien, B., Archana, P. S. & Gupta, A. Copper antimony sulfide ($CuSbS_2$) mesocrystals: A potential counter electrode material for dye-sensitized solar cells. *Mater. Lett.* **124,** 227–230 (2014).

122. Yamamoto, A. & Kambara, S. Structures of the Reaction Products of Tetraalkoxytitanium with Acetylacetone and Ethyl Acetoacetate. *J. Am. Chem. Soc.* **79,** 4344–4348 (1957).

123. Jiang, C. *et al.* Influences of alcoholic solvents on spray pyrolysis deposition of TiO_2 blocking layer films for solid-state dye-sensitized solar cells. *J. Solid State Chem.* **198,** 197–202 (2013).

124. Zhao, Y. & Zhu, K. CH_3NH_3Cl-Assisted One-Step Solution Growth of $CH_3NH_3PbI_3$: Structure , Charge-Carrier Dynamics , and Photovoltaic Properties of Perovskite Solar Cells. *Renew. Energy* (2014).

125. Choy, K. L. & Su, B. Titanium dioxide anatase thin films produced by electrostatic spray assisted vapor deposition (ESAVD) technique. *J. Mater. Sci. Lett.* **18,** 943–945 (1999).

126. Seigo Ito, Peter Chen, Pascal Comte, Mohammad Khaja Nazeeruddin, Paul Liska, P. P. and M. G. Fabrication of Screen-Printing Pastes From TiO_2 Powders for Dye-Sensitised Solar Cells. *Prog. Photovolt Res. Appl.* **15,** 603–612 (2007).

127. Saliba, M. *et al.* A molecularly engineered hole-transporting material for efficient perovskite solar cells. *Nat. Energy* **1,** 15017 (2016).

128. Sommeling, P. M. *et al.* Influence of a $TiCl_4$ Post-Treatment on Nanocrystalline TiO_2 Films in Dye-Sensitized Solar Cells. *J. Phys. Chem. B* **110,** 19191–19197 (2006).

129. Assoud, A., Soheilnia, N. & Kleinke, H. New quaternary barium copper/silver selenostannates: Different coordination spheres, metal-metal interactions, and physical properties. *Chem. Mater.* **17,** 2255–2261 (2005).

130. Cuevas, A., A. Luque, J. D. A. 50 Per Cent More Output From an Albedo Collecting Flat panel Using Bifacial Solar Cells. *Sol. Energy* **29,** 419–420 (1982).

131. Ito, S. *et al.* Bifacial dye-sensitized solar cells based on an ionic liquid electrolyte. *Nat. Photonics* **2,** 693–698 (2008).

132. Dhere, R. G. *et al.* Development of substrate structure CdTe photovoltaic devices with performance exceeding 10%. *Conf. Rec. IEEE Photovolt. Spec. Conf.* 3208–3211 (2012). doi:10.1109/PVSC.2012.6318260

133. Lee, J.-Y., Connor, S. T., Cui, Y. & Peumans, P. Solution-Processed Metal Nanowire Mesh Transparent Electrodes. *Nano Lett* **8,** 689–692 (2008).

134. Klein, A. Energy band alignment in chalcogenide thin film solar cells from photoelectron spectroscopy. *J. Phys. Condens. Matter* **27,** 134201 (2015).

135. Chen, C., Kiriya, D. & Javey, A. 19.2% Efficient InP Heterojunction Solar Cell with Electron-Selective TiO_2 Contact. *ACS Photonics* **1,** 1245–1250 (2014).

136. Wang, Y., Li, C., Yin, X., Wang, H. & Gong, H. Cu_2ZnSnS_4 (CZTS) Application in TiO_2 Solar Cell as Dye. *ECS J. Solid State Sci. Technol.* **2,** Q95–Q98 (2013).

137. Xu, A. *et al.* A novel approach to utilize thiol reduced graphene oxide as linker molecule for Cu_2ZnSnS_4 sensitized solar cell. *Int. J. Hydrogen Energy* **40,** 15933–15939 (2015).

138. Hages, C. J. Development and Characterization of Nanoparticle-Based Kesterite Solar Cells. (2015).

139. German, R. M., Suri, P. & Park, S. J. Review: Liquid phase sintering. *J. Mater. Sci.* **44,** 1–39 (2009).

140. Olson, D. C., Piris, J., Collins, R. T., Shaheen, S. E. & Ginley, D. S. Hybrid photovoltaic devices of polymer and ZnO nanofiber composites. *Thin Solid Films* **496,** 26–29 (2006).

141. Park, S. H. *et al.* Bulk heterojunction solar cells with internal quantum efficiency approaching 100%. *Nat. Photonics* **3,** 297–303 (2009).

142. Chavali, R. V. K., Wilcox, J. R., Ray, B., Gray, J. L. & Alam, M. A. Correlated nonideal effects of dark and light I-V characteristics in a-Si/c-Si heterojunction solar cells. *IEEE J. Photovoltaics* **4,** 763–771 (2014).

143. Webber, D. H. & Brutchey, R. L. Alkahest for V2VI3 Chalcogenides: Dissolution of Nine Bulk Semiconductors in a Diamine-Dithiol Solvent Mixture. *J. Am. Chem. Soc.* **135,** 15722–5 (2013).

144. Houk, J. & Whitesides, G. M. Structure-Reactivity Relations for Thiol-Disulfide Interchange. *J. Am. Chem. Soc.* **11,** 6825–6836 (1987).

145. Zhang, J., Zhou, P., Liu, J. & Yu, J. New understanding of the difference of photocatalytic activity among anatase, rutile and brookite TiO_2. *Phys. Chem. Chem. Phys.* **16,** 20382–20386 (2014).

146. Winkler, M. T. *et al.* Optical designs that improve the efficiency of $Cu_2ZnSn(S,Se)_4$ solar cells. *Energy Environ. Sci.* (2014). doi:10.1039/c3ee42541j

147. Sharbati, S. & Sites, J. R. Impact of the Band Offset for n-Zn(O,S)/p-Cu(In,Ga)Se Solar Cells. *IEEE J. Photovoltaics* **4,** 697–702 (2014).